UC San Diego
UC San Diego Electronic Theses and Dissertations

Title
Study of nonlinear energy transfer between drift wave turbulence and spontaneously generated sheared flows in a laboratory plasma

Permalink
https://escholarship.org/uc/item/566830cd

Author
Xu, Min

Publication Date
2010

Peer reviewed|Thesis/dissertation

eScholarship.org
Powered by the California Digital Library
University of California

UNIVERSITY OF CALIFORNIA, SAN DIEGO

Study of nonlinear energy transfer between drift wave turbulence and spontaneously generated sheared flows in a laboratory plasma

A dissertation submitted in partial satisfaction of the requirements for the degree

Doctor of Philosophy

in

Engineering Sciences (Engineering Physics)

by

Min Xu

Committee in charge:

Professor George R. Tynan, Chair
Professor Patrick H. Diamond
Professor Paul F. Linden
Professor Keiko K. Nomura
Professor Thomas M. O'Neil

2010

Copyright

Min Xu, 2010

All rights reserved.

The Dissertation of Min Xu is approved, and it is acceptable in quality and form for publication on microfilm and electronically:

Chair

University of California, San Diego

2010

To my parents *Zhihua* and *Chunxiu,*

and to my brother *Ping* and sister *Bing*.

TABLE OF CONTENTS

Signature Page iii

Table of Contents v

List of Figures viii

Acknowledgements xiv

Vita xvii

Abstract of the dissertation xix

Chapter 1 Introduction 1

- 1.1 Why fusion? 1
- 1.2 Fusion and the relevant confinement 2
  - 1.2.1 Fusion reactions and Lawson criterion 2
  - 1.2.2 Particle motion in magnetic field 3
  - 1.2.2 Neoclassical and turbulent transport 6
- 1.3 Basic drift turbulence theory 10
  - 1.3.1 Linear electrostatic drift waves and the corresponding instability 10
  - 1.3.2 Hasegawa-Wakatani model and Hasegawa-Mima model 15
- 1.4 Theoretical understanding of zonal flows generation and their back-reaction on turbulence 20
- References: 29

Chapter 2 Previous experimental research on the plasma drift wave-zonal flow system 31

- 2.1 The link between turbulence and confinement 31

2.2 Existence of zonal flows in plasmas 34

2.3 Effects of zonal flows on turbulence 37

2.4 Mean shear effects on turbulence and transport 40

2.5 Previous experiments on CSDX 43

2.6 Motivation behind the dissertation 51

References: 55

Chapter 3 Experimental setup and data analysis methods 58

3.1 CSDX linear plasma device 58

3.2 Diagnostics 60

3.2.1 The dual 3x3 Langmiur probe array 60

3.2.2 The 4-tip turbulent flux Langmiur probe array 66

3.2.3 Fast imaging diagnostic 67

3.3 Methods for data analysis 70

3.3.1 General statistical analysis techniques 70

3.3.2 Bispectral analysis and its interpretation 72

3.3.3 Other techniques used 76

References: 80

Chapter 4 Study of nonlinear spectral energy transfer in frequency domain 81

4.1 Introduction 81

4.2 Theoretical derivation and interpretation of nonlinear energy transfer terms 85

4.3 Experimental measurement of multi-field nonlinear energy transfer 94

4.4 Experimental results 98

4.5 Summary and discussions 105

References: 108

Chapter 5 Fourier-domain study of drift turbulence driven sheared flow in a laboratory plasma. 110

5.1 Introduction 110

5.2 Experimental setup 111

5.3 Experimental results 113

5.4 Linear stability analysis with comparison to experiment 124

5.5 Summary and discussion 130

References: 132

Chapter 6 Generation of a sheared plasma rotation by emission, propagation and absorption of drift wave packets 134

References: 148

Chapter 7 Summary, discussions and future plans 150

7.1 Summary and conclusions 150

7.2 Discussions and future plans 154

7.2.1 Perturbative and bias experiments on CSDX 154

7.2.2 A systematic study of the transition to turbulent stage 155

7.2.3 Analysis of nonlinear energy transfer using conditional average 155

7.2.4 Increasing the separation of spatial scales 156

7.2.5 A testing of ideas from linear machines on tokamak plasmas 156

References: 158

LIST OF FIGURES

Figure 1.1: Gyro-motion of ions and electrons in a uniform magnetic field [5] 3

Figure 1.2: The banana orbit of a particle in a toroidal confinement device [6] 8

Figure 1.3: The thermal (χ_e and χ_i) and particle (D_e , D_{He} , and D_T) diffusivity in a tokamak discharge. The inferred values from experiment are substantially larger than the predicted neoclassical values [4] 10

Figure 1.4: Physical mechanism of a drift wave [13] 13

Figure 1.5: The temporal evolution of the energy spectrum $E_k = \frac{1}{2}\left(\left|n_k\right|^2 + k^2\left|\phi_k\right|^2\right)$ 19

Figure 1.6: The density contour (a) and potential contour (b) from the numerical simulation of the electrostatic plasma turbulence. The closed iso-potential contours indicate that an azimuthally directed, radially sheared flow has been generated [18] 20

Figure 1.7: Zonal electric field and zonal flow. The poloidal cross-section is shown here, where the hatched region and dotted region denote the positive and negative charges respectively [11] 21

Figure 1.8: (a) The magnetic field and $\vec{E}\times\vec{B}$ drift. The fact that the magnetic field line deviates from the geodesic line causes the compression of plasma. (b) The helical zonal flows in a torus [20] 22

Figure 1.9: The generation of zonal flows by drift wave turbulence via three wave (triad) coupling. The wavenumbers of drift waves are much bigger than that of the zonal flow $\vec{k}_1,\ \vec{k}_2 \gg \vec{k}_{ZF}$, indicating a non-local energy transfer in wavenumber space[11] 24

Figure 1.10: (a) (Left) spatially complex structures of zonal flows. (b) (Right) zonal flow shearing is a random, diffusive process consists of a series of kicks [21] 26

Figure 1.11: The paradigm of drift wave-zonal flow system for plasma turbulence [10] 27

Figure 2.1: The ratio of normalized plasma potential to normalized density fluctuations is plotted out as a function of radius. The ratio is significantly bigger than the expected value ~1 for the case of adiabatic electrons. (a) is for ohmic discharge and (b) is L-mode discharge [8] 32

Figure 2.2: Radial profiles of turbulent particle flux in the ISX-B tokamak. The empty squares correspond to the case with neutral beam heating, and the filled squares are for the case without beam heating [8]. 33

Figure 2.3: Radial profiles of total ion and electron heat flux from power balance q (shaded area), the total convective heat flux q_{conv} predicted by a neutral-penetration code and H_α measurements, and the turbulence-introduced heat flux $q_{conv}^{\tilde{E}}$ [9]. 34

Figure 2.4: Zonal flow structure measurement in CHS [10, 11]. 36

Figure 2.5: Turbulence modulation due to stationary zonal flows in CHS [17, 18]. (a) Evolution of the wavelet spectrum of electric field. (b) Evolution of zonal flows $Z_A(t)$. (c) FFT spectrum of wavelet power evolution of frequencies 30 to 100 kHz. (d) Conditional averages of wavelet power spectra around the maxima and minima of the zonal flow. 38

Figure 2.6: Turbulence modulation due to GAM in JFT-2M [19]. (a) GAM fluctuation. (b) The ambient density fluctuation. (c) Power spectrum of the envelope of density fluctuation. (d) Coherence between GAM and density fluctuation. 39

Figure 2.7: (a) RMS fluctuation amplitude shows a reduction of fluctuation intensity in the H-mode regime. (b) Turbulent radial correlation length. (c) D_α light emission from the separatrix region [26]. 41

Figure 2.8: (a) The frequency resolved turbulent particle flux and (b) density potential cross-phase in the ohmic and ohmic H-mode [27]. 42

Figure 2.9: The spatially resolved spectrum for floating potential at different magnetic field. It is clear that when the magnetic field increases from 500 Gauss to 1000 Gauss, potential fluctuations evolves from a combination of discrete modes into a broadband turbulent stage [28] 45

Figure 2.10: Azimuthal wavenumber spectral evolution suggests an inverse energy transfer [28] 46

Figure 2.11: Both the Mach probe data (blue curve) and the TDE inferred azimuthal velocity (black diamonds) show that there is a shear flow in the plasma. The black solid line is the inferred velocity from turbulent momentum conservation analysis. The red curve is from a two-field turbulence simulation [34]. 48

Figure 2.12: Plasma equilibrium profiles. (a) Density (solid black) and RMS of density fluctuation (solid red). (b) Turbulent particle flux. (c) Reynolds Stress. (d) Estimated ion viscosity. (e) Plasma azimuthal velocity [31]. 49

Figure 2.13: Inferring the residual stress term and relevant profiles. (a) Equilibrium density. (b) Reynolds stress. (c) Mean square of turbulent radial velocity. (d) Constructed diffusive turbulent transport term, $\pi_{diff} = -\chi_\theta \frac{\partial \langle u_\theta \rangle}{\partial r}$. (e) Inferred residual stress. (f) Equilibrium azimuthal velocity [32]. 51

Figure 3.1: Skematic of the Controlled Shear Decorrlation Experiment linear plasma device [1]

....59

Figure 3.2: Picture of the Controlled Shear Decorrlation Experiment. 60

Figure 3.3: Dual 3x3 Langmiur probe array, of which one 3x3 array (9 channels) is for floating potential and anther 3x3 array is for ion saturation current (or density). These two arrays shift in the axial direction by 1.5 mm [2]. 61

Figure 3.4: Thevinen equivalence for floating potential channels with resistor placed after the cable...63

Figure 3.5: Thevinen equivalence for floating potential channels with resistor placed before the cable...64

Figure 3.6: The 4-tip turbulent flux probe array. (a) and (b) shows the position relative to the magnetic field line. (c) is a 3D sketch and (d) is a picture of the Langmiur probe array. One of the 3 short tips is for ion saturation current, and the rest (two short tips and one long tip) are for floating potential, as indicated in (b). 66

Figure 3.7: The optical setup of the fast imaging system [2] 68

Figure 3.8: Raw ion saturation current signal from Langmiur probe and light intensity fluctuation from fast imaging as a function of time. (b) Cross-correlation between Isat and light intensity fluctuations [7]...69

Figure 3.9: (a) auto-spectrum of the test signal x(t). (b) 3D view of the auto-bicoherence. (c) auto-bispectrum, and (d) auto-bicoherence. 75

Figure 3.10: The azimuthal velocity measured by two-point correlation TDE from probe and imaging data compared against ion fluid velocity measured by Mach probe [14]. 77

Figure 4.1: Calculation region for 3-field (X,Y, Z) cross-bispectrum and cross-bicoherence.

The x-axis is for field X and y-axis is for field Y. 93

Figure 4.2: Spatial layout of the measurement grid points..95

Figure 4.3: (a) Time-averaged plasma density. (b) Time resolved plasma azimuthal velocity profile calculated from 2D visible light imaging using Time Delay Estimation [31]. (c) Time-averaged electron temperature profile [28]. (d) Correlation between density and potential fluctuations at shear layer. 99

Figure 4.4: Convergence test for the bispectral calculation for the internal and kinetic energy transfer terms $T_n(f, f_1)$ and $T_u(f, f_1)$ at the frequencies $f = 0.25KHz$ and $f_1 = 10.25KHz$. (a) is for $T_n(f = 0.25KHz, f_1 = 10.25KHz)$ and (b) is for $T_u(f = 0.25KHz, f_1 = 10.25KHz)$ 100

Figure 4.5: Enveloped signals from Langmiur probe data 102

Figure 4.6: Measurement is taken at $r = 3.6cm$, magnetic field 1000Gauss, RF power 1.5KW and pressure 3.0mtorr. (a) Bispectral internal energy transfer $T_n(\omega, \omega_1)$. (b) Bispectral kinetic energy transfer $T_u(\omega, \omega_1)$ 103

Figure 5.1: Equilibrium radial profiles for CSDX. (a) Time-averaged density (solid black) and RMS of density fluctuation (solid red). (b) Time-averaged turbulent particle flux. (c) Time-averaged Reynolds Stress. (d) Estimated ion viscosity. (e) Plasma azimuthal velocity [17]. 114

Figure 5.2: Typical autospectra (a) density, (b) potential, and (c) perpendicular velocity for the weakly turbulent plasmas in CSDX. Measurement was taken at argon pressure 3.2 mTorr, magnetic field 1000 Gauss, and RF power 1.5 kW by the dual 3x3 Langmuir probe array centered at the radial position r=3.6 cm. 116

Figure 5.3: The experimentally measured nonlinear energy transfer rates............................117

Figure 5.4: Net energy transfer rates (a) internal (b) kinetic. Here a positive value at one specific frequency means that density (or perpendicular velocity) fluctuation at this frequency gains energy, while a negative value means losing energy. 119

Figure 5.5: Contributions to the net internal and kinetic energy transfer rates from each different term 123

Figure 5.6: Two-point spectrum $S(f, k_\theta)$ from potential (with the intensity in log scale)124

Figure 5.7: (a) Nonlinear energy transfer rates mapped from frequency domain to wavenumber domain (b) Effective growth rates inferred from the nonlinear net energy transfer rates. (c) Linear growth rates from Hasegawa-wakatani model. 128

Figure 6.1: Time averaged radial profiles of the CSDX plasma 137

Figure 6.2: Sequential visible light emissions images showing the birth, evolution, and death of vortex-like structures. Radii of r = 3.0 cm and r = 4.0 cm are denoted by the two dashed circles...139

Figure 6.3: (a) Nonlinear kinetic energy transfer vs. effective azimuthal mode number. (b) Time resolved density (blue) and vorticity (red) fluctuations. (c) Correlation between density and vorticity fluctuations. (d-g) Cross-correlation between vorticity flux at different radial positions...144

ACKNOWLEDGEMENTS

As I complete one milestone in my life, I am feeling truly thankful to all the people who have helped me walk this far along the route. I'd like to give my deepest gratitude to my great advisor, Professor George Tynan, who is knowledgeable, creative, patient and understanding, with outstanding intuition in physics and really thinks for students. To me, he is a very good friend as well as a great advisor, who taught me so much not only about plasma physics but also elements to succeed in academic careers and life in general. Thank you so much for helping me to become who I am today, and well prepared to become who I want to be in the future.

I owe deep gratitude to professors who offered me excellent lectures during the past five years in UCSD, particularly to Professors Patrick H. Diamond, Thomas M. O'Neil, Sergei I. Krasheninnikov, and Sutanu Sarkar who are well-known for their very broad knowledge, outstanding ability to explain complicated physics concepts in simple language, and devotion and patience inside and outside classes for students. I also want to thank Professors Thomas Bewley, Stefan G. Llewellyn Smith, and Constantine Pozrikidis who helped me a lot to develop my scope in numerical methods. Thank you all so much for all the classes in both physics and math, from which I definitely have benefited a lot and for sure I will continue to get benefits in the future.

I should give my sincere gratitude to my Ph.D. committee members, Professor Patrick H. Diamond, Professor Thomas M. O'Neil, Professor Paul. F. Linden, and Professor Keiko K. Nomura. Thank you all very much for the invaluable comments and suggestions within the scope of research

and outside research.

I really want to give my special thanks to all the scientists and engineers in the CSDX and PISCES group, including Russ Doerner, Christopher Holland, Jonathan Yu, Daisuke Nishijima, Stefan Muller, Karl R. Umstadter, Eric Hollmann, Alex James, Matthew Baldwin, Leo Chousal, Rolando Hernandez, Ray Seraydarian, Tyler Lynch, Zheng Yan, Laizhong Cai, Nazli Taheri and all others, who have helped me a lot in innumerable ways. Particularly Dr. Christopher Holland and Dr. Jonathan Yu have offered very detailed assistances in physics models and numerical codes, as well as very useful comments and suggestions along the way of my research. To me, Leo Chousal and Rolando Hernandez are like my two big brothers, they really not only helped me greatly in experiments but also brought me lots of invaluable suggestions for life. It is a fortune to meet you two. Laizhong Cai and Zheng Yan have worked very closely with me throughout all these years. I really want to thank you two for all your support as my colleagues and best friends.

The MAE and CER staff are really helpful and did excellent jobs. In particular I would like to thank Linda McKamey, Justin Williams, Brandi Pate, Sandy Rosas, and Cynthia Escobedo for treating me so nicely and kindly all the time.

Of course I will never forget those many years that I spent in USTC, where learned and experienced a lot, and especially I met lots of great people. I owe a great deal to my former advisor, Professor YiZhi Wen, who guided me into the world of plasma physics and trained me very well with necessary skills in experiments, and helped me to grow as a young scientist. His brilliant ideas and suggestions are still benefiting me a lot today. I also want to give my great thanks to Professors ChangXuan Yu, JinXiu Ma, Ding Li, WanDong Liu, JinXiang Cao, and RuJuan Zhan for offering excellent courses in plasma physics. I really learned a lot and had great times with my fantastic lab mates in USTC, including ZhiJiang Wang, RongHua Lu, Jun Wang, Yi Yu, Xiang Sun, DeLong Xiao, Tao Lan, YangFang Li, Liang Lin, Gang Chen, and all others. Thank you all very much.

It is a great treasure to me to have so many fantastic friends along the way, both in US and in China. I want to let you know that you all are very important to me, and I am feeling truly thankful to have you as friends.

Most of all, I want to thank my family, my father ZhiHua Xu, mother ChunXiu Shen, brother Ping Xu, sister Bing Xu, sister in law Jue Li, brother in law GuoDong Liu,and my cute nephew Lang Xu, for their love, support and patience.

The text and data in chapter 4, in full, is a reprint of the material as it appears in "Study of nonlinear spectral energy transfer in frequency domain", M. Xu, G. R. Tynan, C. Holland, Z. Yan, S. H. Muller, J. H. Yu, Phys. Plasmas **16** 042312 (2009). The dissertation author is the primary investigator and author of this article.

The text and data in chapter 5, in full, is a reprint of the material as it appears in "Fourier-domain study of drift turbulence driven sheared flow in a laboratory plasma", M. Xu, G. R. Tynan, C. Holland, Z. Yan, S. H. Mueller, J. H. Yu, Phys. Plasmas 17, 032311 (2010). The dissertation author is the primary investigator and author of this article.

The text and data in chapter 6, in full, is a reprint of the material submitted to Phys. Rev. Lett. as it appears in "Generation of a Sheared Plasma Rotation by Emission, Propagation and Absorption of Drift Wave Packets", M. Xu, G. R. Tynan, P. H. Diamond, S. H. Muller, C. Holland, J. Yu , Z. Yan, Phys. Rev. Lett. (2010). The dissertation author is the primary investigator and author of this article.

VITA

2010	Ph.D., Engineering Physics, University of California, San Diego, California, USA
2005-2010	Graduate Student Researcher, Center for Energy Research, University of California, San Diego, California, USA
2009	Teaching Assistant, Department of Mechanical and Aerospace Engineering, University of California, San Diego, California, USA
2005	M.S., Applied Physics, University of Science and Technology of China, Hefei, China
2001	B.S., Physics, University of Science and Technology of China, Hefei, China
2001	B.A., Business Administration, University of Science and Technology of China, Hefei, China

PUBLICATIONS

Generation of a Sheared Plasma Rotation by Emission, Propagation and Absorption of Drift Wave Packets, M. Xu, G. R. Tynan, P. H. Diamond, S. H. Muller, C. Holland, J. Yu , Z. Yan, submitted to *Phys. Rev. Lett.* (2010)

Fourier-domain study of drift turbulence driven sheared flow in a laboratory plasma, M. Xu, G. R. Tynan, C. Holland, Z. Yan, S. H. Mueller, J. H. Yu, *Phys. Plasmas* 17, 032311 (2010)

Study of nonlinear spectral energy transfer in frequency domain, M. Xu, G. Tynan, C. Holland, Z. Yan, S. Muller, J. Yu, *Phys. Plasmas* 16, 042312 (2009)

Intrinsic Rotation from a Residual Stress at the Boundary of a Cylindrical Laboratory Plasma, Z. Yan, M. Xu, P. H. Diamond, C. Holland, S. H. Muller, G. R. Tynan, J. H. Yu, *Phys. Rev. Lett.* 104, 065002 (2010)

Shear flow and drift wave turbulence dynamics in a cylindrical plasma device, Z. Yan, G. R. Tynan, C. Holland, M. Xu, S. H. Muller, J. H. Yu, *Phys. Plasmas* 17, 032302 (2010)

Scaling properties of turbulence driven shear flow, Z. Yan, G. R. Tynan, C. Holland, M. Xu, S. H. Muller, and J. H. Yu, *Phys. Plasmas* 17, 012302 (2010)

Statistical analysis of the turbulent Reynolds stress and its link to the shear flow generation in a cylindrical laboratory plasma device, Z. Yan, J. H. Yu, C. Holland, M. Xu, S. H. Muller, and G. R. Tynan, *Phys. Plasmas* 15, 092309 (2008)

FIELDS OF STUDY

Major field: Engineering Sciences (Engineering Physics)

Studies in Plasma Physics
Professor George R. Tynan

ABSTRACT OF THE DISSERATION

Study of nonlinear energy transfer between drift wave turbulence and spontaneously generated sheared flows in a laboratory plasma

by

Min Xu

Doctor of Philosophy in Engineering Sciences (Engineering Physics)

University of California, San Diego, 2010

Professor George R. Tynan, Chair

Experiments in a laboratory plasma are used to identify how small-scale turbulent structures give rise to large-scale sheared zonal flows. A new technique based on cross-bispectral analysis has been developed and applied to directly measure the nonlinear energy transfer rates between drift wave turbulence and sheared flows. In addition fast imaging is used to directly observe the turbulent

structure dynamics. A combined study using both Langmiur probe arrays and fast visible light imaging shows that the sheared zonal flow is sustained by the emission of drift vortices in the central plasma which then propagate in a spiral trajectory, approach the shear layer, and then merge into the sheared flow, thereby transferring their momentum and kinetic energy to it. The shear flow is then amplified. The results are consistent with previous probe measurements of the turbulent Reynolds stress, and provide a detailed confirmation of the basic theoretical expectations for the turbulent drive of zonal flows in magnetized plasmas.

Chapter 1

Introduction

1.1 Why fusion?

When discussing energy, most people think of oil, coal, natural gas, solar, wind power, hydropower, etc., but few will realize that all the above energy resources actually originate from the sun, which is powered by nuclear fusion. Fusion is the mechanism that powers our sun and all the stars in the universe, and it is the origin of nearly all forms of energies in nature. Although currently fossil fuels provide most of the world's energy, these fuels supply are limited and we are running out of them rather quickly. At current consumption rates, the proven oil reserve will be used up in about 30-50 years, the proven natural gas reserve can only sustain roughly 60 more years, and the coal reserve will be depleted within 150 years [1]. Although it seems that renewable energies such as solar and wind, which are large and inexhaustible, will play important roles in future energy supply, they are highly intermittent, seasonal and subject to geographic limitations, therefore have limited potential. In order to fill up the gap left by the depletion of fossil fuels in the future, we need a reliable, sustainable, environmentally benign, and economical source of energy. Fusion is a candidate solution that may offer all of the above qualities.

1.2 Fusion and the relevant confinement

1.2.1 Fusion reactions and Lawson criterion

Nuclear fusion is the process in which multiple light nuclei fuse together to form a single heavier nucleus. Generally a fusion of two nuclei with lower mass than iron, which has the largest binding energy per nucleon, releases energy; while a fusion of two nuclei heavier than iron absorbs energy. The typical nuclear fusion reactions in current fusion energy research are:

$$D^2 + T^3 \rightarrow He^4(3.5MeV) + n^1(14.1MeV) \tag{1.1}$$

$$D^3 + D^2 \rightarrow He^2(0.82MeV) + n^1(2.45MeV) \tag{1.2}$$

$$D^2 + D^2 \rightarrow T^3(1.01MeV) + H^1(3.02MeV) \tag{1.3}$$

$$D^2 + He^3 \rightarrow He^4(3.6MeV) + H^1(14.7MeV) \tag{1.4}$$

By far the most promising method to supply fusion energy is through reaction Eqn. (1.1) by heating deuterium-tritium fuel to a sufficiently high temperature (10 keV or roughly 100 million degree centigrade) such that the thermal velocities of nuclei are high enough to overcome the Coulomb repulsion force to produce the fusion reaction. As a result we need to confine the very hot ions and electrons to maintain a sufficient ion density n, at a very high temperature T, for a sufficient long time τ_E, as described by the famous Lawson criterion [2]:

$$nT\tau_E > 5\times10^{21} m^{-3} s\ keV \tag{1.5}$$

In the above equation τ_E is called the energy confinement time, and is a measure of the rate at which the system loses energy to the environment. Although the required density, temperature and confinement time have all been obtained, they have not been achieved in the same plasma. The energy confinement time is defined as the total stored thermal energy in the plasma W, divided by the energy loss rate P_{loss} :

$$\tau_E \equiv \frac{W}{P_{loss}} \tag{1.6}$$

1.2.2 Particle motion in magnetic field

The idea of using magnetic field to confine the hot fusion fuel particles in the form of plasma is called magnetic confinement fusion [3], which is one of the two major branches of nuclear fusion research, with the other being inertial confinement fusion [4] that seeks to fuse nuclei so fast that the fuel assembly do not have time to expand. The magnetic fusion has been highly developed and is generally considered more promising for energy production.

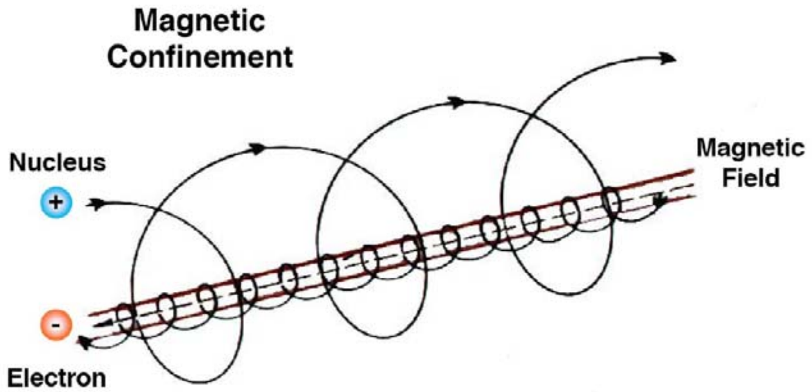

Figure 1.1 Gyro-motion of ions and electrons in a uniform magnetic field [5].

When an externally imposed magnetic field is present in a plasma, charged particles (ions and electrons) will gyrate around the magnetic field lines, as shown in figure 1.1. They can not move across the magnetic field lines and therefore are confined in the directions perpendicular to the magnetic field. Along the magnetic field charged particles can move freely thus are not confined.

Ions and electrons in magnetic field experience guiding center drifts, which can be easily seen from the fluid momentum equation:

$$mn\frac{d\vec{v}}{dt} = qn\left(\vec{E} + \vec{v} \times \vec{B}\right) - \nabla p \tag{1.7}$$

where the plasma density is denoted by n, the charge carried by the particle by q, electric field by $\vec{E}$, magnetic field by $\vec{B}$, and the pressure gradient by ∇p. By crossing the above equation by $\vec{B}$ and solving the corresponding equation we can get the velocity perpendicular to the magnetic field

$$\vec{v}_\perp = \frac{\vec{E} \times \vec{B}}{B^2} - \frac{\nabla p \times \vec{B}}{qnB^2} - \frac{m}{qB^2}\frac{d\vec{v}_\perp}{dt} \times \vec{B} \tag{1.8}$$

For the conditions of our experiments the first term on the RHS of equation (1.8) is dominant [3], and thus we can replacing $\frac{d\vec{v}_\perp}{dt}$ in the RHS by $\frac{d\vec{v}_\perp}{dt} = \frac{d}{dt}\left(\frac{\vec{E} \times \vec{B}}{B^2}\right)$ and the equation becomes

$$\vec{v}_\perp = \frac{\vec{E} \times \vec{B}}{B^2} - \frac{\nabla p \times \vec{B}}{qnB^2} + \frac{m}{qB^2}\frac{d\vec{E}_\perp}{dt} \tag{1.9}$$

Equation (1.9) can be rewritten as

$$\vec{v}_\perp = \frac{\vec{E} \times \vec{B}}{B^2} - \frac{\nabla p \times \vec{B}}{qnB^2} \pm \frac{1}{\omega_c B}\frac{d\vec{E}_\perp}{dt} \tag{1.10}$$

where $\omega_c = \frac{qB}{m}$ is the cyclotron frequency and the “+” and “-” signs correspond to positive and negative charged particles respectively. The first term in the RHS of equation (1.10) is called the ExB drift velocity $v_E = \frac{\vec{E} \times \vec{B}}{B^2}$. It is independent with charge and mass, which means that for both ions and electrons their ExB drift velocities are in the same direction and with the same magnitude.

Therefore ExB drift does not lead to charge separation in the plasma. The second term in the RHS of equation (1.10) is called diamagnetic drift velocity $v_d = -\frac{\nabla p \times \vec{B}}{qnB^2}$. The diamagnetic drift velocity is actually not a guiding center drift of particles, but is instead a fluid velocity related to the fact that there are more particles passing through a reference surface in one direction than the other when there is a pressure gradient. The last term of equation (1.10) is normally referred as the polarization drift $v_p = \pm \frac{1}{\omega_c B} \frac{d\vec{E}_\perp}{dt}$. Its physical origin is easy to understand: suppose there is an ion at rest in magnetic field $\vec{B}$, and suddenly an electric field $\vec{E}_\perp(t)$ perpendicular to $\vec{B}$ is applied. The first thing that the ion does is to move along $\vec{E}_\perp$. It is only after picking up a velocity does the ion feel the $\vec{v} \times \vec{B}$ Lorentz force. Therefore polarization drift can be thought of as a startup drift due to inertia. Note that the polarization drift velocities of ions and electrons are in the opposite directions, therefore they will result in a charge separation, which we will see lately in the following sections that it will lead to drift wave instability.

When the magnetic field is not uniform, there will be other mechanisms that lead to drift motions in plasmas, such as curvature drift and ∇B drift, etc. When a particle's guiding center drift follows a curved magnetic field line, it feels a centrifugal force $\vec{F}_c = \frac{mv_\parallel^2}{R} \hat{r}_c$, where $\hat{r}_c$ is the unit vector outward along the radius of curvature. The corresponding momentum equation is:

$$m\frac{d\vec{v}}{dt} = \vec{F}_c + q\vec{v} \times \vec{B} \qquad (1.11)$$

Following similar derivation for the ExB drift, the curvature drift velocity can be obtained:

$$v_c = \frac{1}{q}\frac{\vec{F}_c \times \vec{B}}{B^2} = \frac{mv_{\parallel}^2}{qB^2}\frac{\hat{r}_c \times \vec{B}}{R} \tag{1.12}$$

In a magnetic field with a transverse gradient the part of particle's orbit on the stronger magnetic field side has a smaller gyro-radius, while the part on the weaker magnetic field side has larger gyro-radius. This leads to a guiding center drift due to ∇B. Its drift velocity can be written as:

$$v_{\nabla B} = \pm\frac{1}{2}v_{\perp}r_L\frac{\vec{B}\times\nabla B}{B^2} \tag{1.13}$$

More detailed derivation of the drift velocities can be found at any plasma physics text books such as [3].

1.2.2 Neoclassical and turbulent transport

If the energy (or particle) loss in a magnetically confined plasma is fully diffusive, we can model the corresponding transport using random walk processes, for which the diffusion coefficient D can be expressed as:

$$D = \frac{\delta^2}{\Delta t} = \nu\delta^2 \tag{1.14}$$

where δ here is the average random walk step size and Δt is the average time elapsed between two successive walks, and ν is defined as $\frac{1}{\Delta t}$ and is the average random walk frequency. From the diffusion equation with constant diffusion coefficient:

$$\frac{\partial\phi(r,t)}{\partial t} = D\nabla^2\phi(r,t) \tag{1.15}$$

we can estimate the energy confinement time as

$$\tau_E = \frac{L^2}{D} \tag{1.16}$$

where L is the plasma pressure gradient scale length and is associated with machine size, and we have taken $\frac{\partial}{\partial t} \sim \frac{1}{\tau_E}$ and $\nabla^2 \sim \frac{1}{L^2}$. Combining Eqns. (1.15) and (1.16) we can rewrite the energy confinement time as

$$\tau_E = \frac{L^2}{\delta^2}\Delta t = \frac{L^2}{\nu\delta^2} \tag{1.17}$$

The above equation implies that we can get a better confinement by either increasing the machine size L or decreasing the random walk size δ. In a cylindrical plasma the collisional transport of particles and energy can be understood using this simple random walk model, by simply replacing Δt with the characteristic collision time τ_c and the random walk step size by the Larmor gyro-radius ρ_L, such that the diffusion coefficient becomes $D = \frac{\rho_L^2}{\tau_c}$ and the corresponding energy confinement time becomes $\tau_E = \left(\frac{L}{\rho_L}\right)^2 \tau_c$. This collisional diffusion in a cylindrical plasma is called *classical diffusion*.

The classical transport model described above is not appropriate in a torus [3], especially for high temperature plasmas in which the lower collisional frequency allows particles to have trajectories determined by the toroidal geometry, such as banana orbits as shown in figure 1.2.

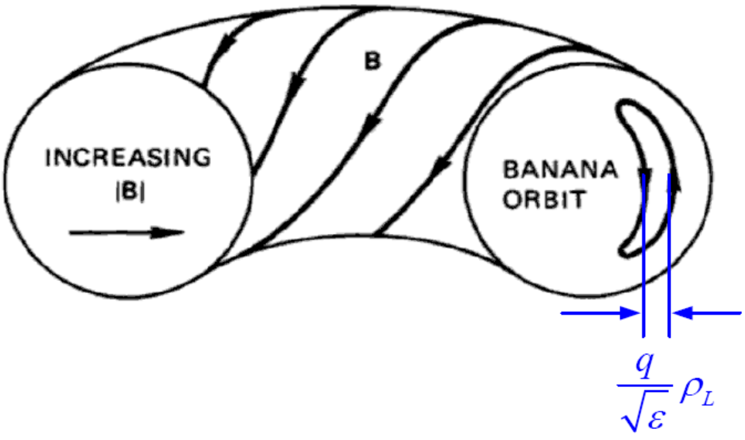

Figure 1.2 The banana orbit of a particle in a toroidal confinement device [6].

Because the collisions which scatter the ions or electrons out of their trapped banana orbits will displace the particles across the flux surface by a distance of the banana orbits width, $\frac{q}{\varepsilon^{1/2}}\rho_L$, therefore they will lead to a bigger random walk step size and thus a higher diffusive transport. Here q is the safety factor defined as $q = \frac{rB_\phi}{RB_\theta}$, where r is the minor radius and R is major radius; B_ϕ and B_θ are the magnetic field in the toroidal and poloidal direction respectively, and ε is the inverse aspect-ratio which is defined as $\varepsilon = a/R$. By taking into account that only a fraction, $\sim \varepsilon^{1/2}$, of particles are trapped, the effective banana regime diffusion coefficient is $D \sim \frac{q^2}{\varepsilon^{3/2}}\frac{\rho_L^2}{\tau_c}$, and the corresponding energy confinement time is $\tau_E \sim \frac{\varepsilon^{3/2}}{q^2}\left(\frac{L}{\rho_L}\right)^2 \tau_c$ [3]. This collisional transport in a torus is known as *neoclassical transport*, in which case τ_E is different from the classical diffusion by a factor of $\frac{\varepsilon^{3/2}}{q^2}$. Note that in a toroidal machine typically $q > 1$

in the center of plasma and $q \sim 2-8$ at the edge, and the inverse aspect-ratio $\varepsilon < 0.5$, which renders $\frac{\varepsilon^{3/2}}{q^2} \sim 0.1$, and thus this transport exceeds the classical values.

Nuclear fusion probably would have been realized today if the cross field particle and thermal transport follow their neoclassical levels. However with few exceptions their values measured in experiments are much higher than the levels predicted by the neoclassical calculation. Figure 1.3 shows such a case for the L-mode (low confinement mode) discharges [7], where it is very clear that all the thermal (χ_e and χ_i) and particle (D_e, D_{He}, and D_T) diffusivity are much higher than the predicted neoclassical values, especially the electron heat conduction is about two orders of magnitude higher than its predicted neoclassical values. This enhanced transport is now believed to be largely due to the presence of turbulence in plasmas, or more specifically the low-frequency drift wave turbulent fluctuations [7, 8]. Such turbulence-induced high level of thermal and particle transport is normally referred to as "anomalous" transport or *turbulent transport*. Therefore in order to achieve a better confinement and ultimately realize fusion, we really need to understand how drift turbulence is generated in plasmas, how it induces the large transport, and how we can predict and control the turbulence and the resulting turbulent transport. Key aspects of this turbulent transport physics are summarized in several recent review papers [8-11].

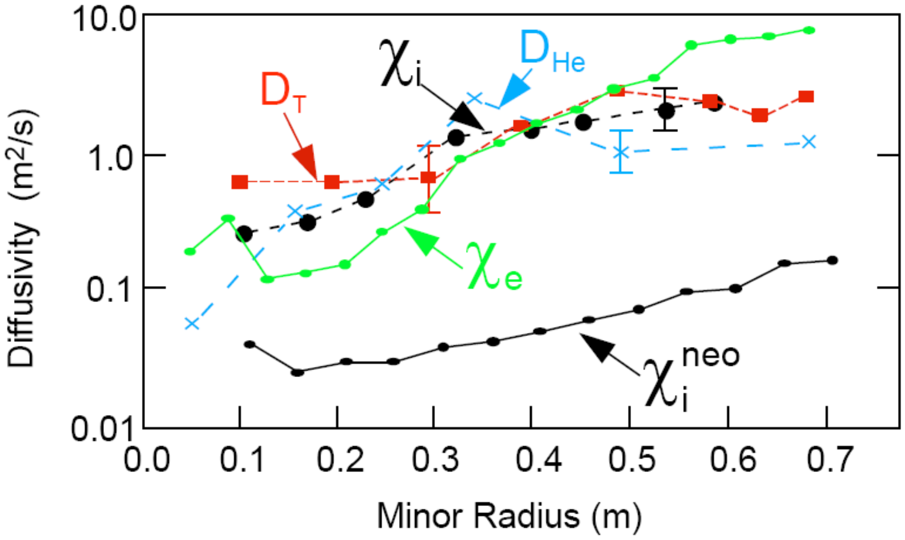

Figure 1.3. The thermal (χ_e and χ_i) and particle (D_e, D_{He}, and D_T) diffusivity in a tokamak discharge. The inferred values from experiment are substantially larger than the predicted neoclassical values [4].

1.3 Basic drift turbulence theory

1.3.1 Linear electrostatic drift waves and the corresponding instability

Drift waves and drift turbulence result from the interaction between the dynamics perpendicular and parallel to the magnetic field due to the combined effects of density gradient, ion inertia, and electron parallel motion. The name ‘drift wave’ is related to the fact that the wave phase velocity (perpendicular to both density gradient and magnetic field) propagates in the diamagnetic drift direction of the species with dominant pressure gradient at a speed of approximately the same as the diamagnetic drift velocity.

A brief derivation of drift wave dispersion relation is shown in the following, which is quite simple and is available elsewhere in many text books and papers such as [6, 12, 13]. For the cool collisional plasma used in our work it is normal to assume $u_{thi} << \omega / k_{||} << u_{the}$, where ω is the drift wave frequency, u_{thi} and u_{the} are the ion and electron thermal speed respectively, such that for the interested time scale electrons can move rapidly along the magnetic field line to establish a thermodynamic equilibrium among themselves, but ion motions along B could be neglected. Therefore for electron momentum equation along magnetic field, we have

$$m_e n_e \left(\frac{\partial \vec{u}_{e||}}{\partial t} + \vec{u}_{e||} \cdot \nabla \vec{u}_{e||} \right) = neE_{||} + \nabla_{||} P_e \tag{1.18}$$

where P_e is the electron pressure, E is the electric field and $||$ denotes the direction along the magnetic field. Here electron dissipation has been neglected. Because electrons have low inertia, the LHS of Eqn. (1.18) is small and thus negligible, and we can then obtain a Boltzmann relation:

$$\frac{\tilde{n}}{n_0} = \frac{e\tilde{\phi}}{k_B T_e} \tag{1.19}$$

where n_0 and T_e are the equilibrium density and temperature, and it is assumed that $\frac{e\tilde{\phi}}{k_B T_e} \ll 1$. When considering waves satisfying $\omega / k_{||} \gg u_{thi}$, we can neglect the parallel ion motion. For the conditions of our experiments the ion motion perpendicular to the magnetic field is dominated by the ExB velocity $\tilde{u}_{\perp} \approx \tilde{u}_E = -\frac{\nabla \tilde{\phi} \times \hat{z}}{B}$ ($\hat{z}$ stands for the direction along magnetic field line), thus the ion continuity equation

$$\frac{\partial n_i}{\partial t} + \nabla \cdot (n_i \tilde{u}_i) = 0 \tag{1.20}$$

can be rewritten as:

$$\frac{\partial n_i}{\partial t}+\tilde{u}_E\cdot\nabla n_i=0 \tag{1.21}$$

For a plane wave solution $\sim\exp\left(i\vec{k}\cdot\vec{r}-i\omega t\right)$, we then have

$$i\omega\tilde{n}_i=-\frac{1}{B_0}\frac{\partial\tilde{\phi}}{\partial y}\nabla n_0 \tag{1.22}$$

where y refers to the azimuthal direction, and the density gradient is only in the radial direction. Combining (1.19) and (1.22) and using the quasi-neutrality condition $\tilde{n}_e\approx\tilde{n}_i=n$, the drift wave dispersion relation could be found:

$$\frac{\omega}{k_y}=-\frac{k_BT_e}{eB_0}\frac{\nabla n_0}{n_0} \tag{1.23}$$

Note that in Eqn. (1.23) the drift wave phase velocity is exactly the electron diamagnetic drift velocity. The physical picture of the electron drift wave is shown in figure 1.4, where the equilibrium density gradient is towards the left, and the equal density contour is initially a vertical line. If a small density perturbation is introduced then it will perturb the equal density contour, as indicated by the isobar . In the case when Eqn. (1.19) is valid, i.e., electrons can move freely along magnetic field line such that density and potential fluctuations are in phase, higher density regions have a higher potential, which means that region ① in figure 1.4 has a higher potential and region ③ has a lower potential, leading to an electric field along the y direction at position ②. Therefore an ExB drift pointing to the “+x” direction exist at position ②, which will bring in particles from the denser plasma region and increase the density at position ②. The fluctuating electric fields at other locations are indicated by the arrows under E_y, and the corresponding drift velocities for electrons and ions are indicated by v_e and v_i respectively (in figure 1.4 v_i is the total drift velocity that includes the ExB and polarization drift velocities). By looking at the arrows indicating velocities we can tell that the drift motions move the perturbation upward, thus generating an oscillatory drift wave.

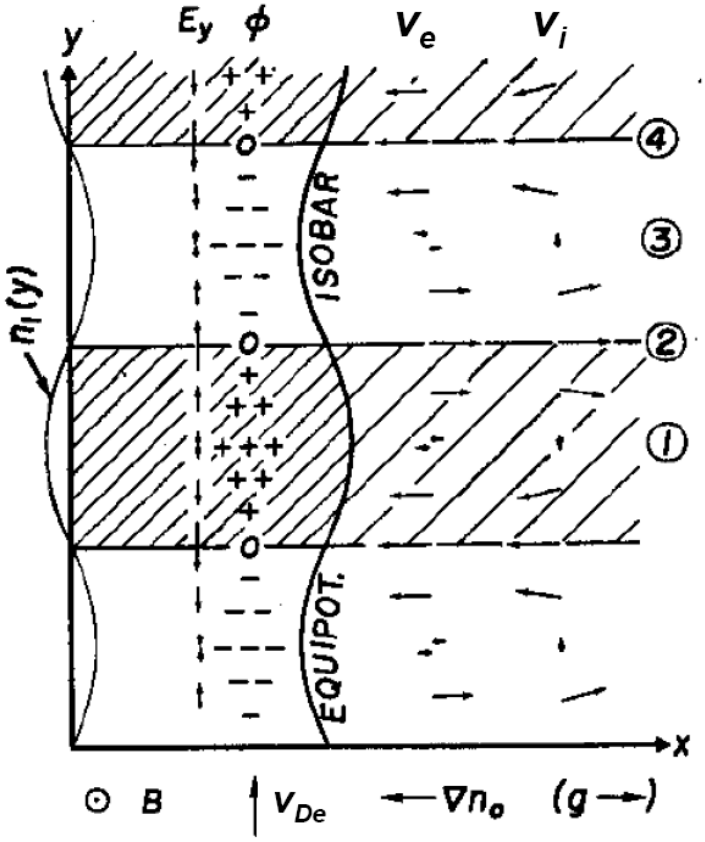

Figure 1.4 Physical mechanism of a drift wave [13].

Note that the drift wave described above is purely oscillatory, hence no damping or growth is predicted. The drift instabilities are a particular important class of instabilities which have often been invoked as the source of plasma turbulence responsible for anomalous transport in tokamaks. The origin of resistive drift wave instability could be seen through the following derivation [6]. Since the electron polarization drift is negligible due to its low inertia $m_e \ll M_i$, the ion polarization drift $\tilde{v}_{pi} = \frac{1}{\omega_{ci} B} \frac{d\tilde{E}_{\perp}}{dt}$ carries the perpendicular current:

$$\tilde{J}_\perp = en_{i0}\tilde{v}_{pi} = \frac{en_{i0}}{\omega_{ci}B}\frac{d\tilde{E}_\perp}{dt} = -\frac{en_{i0}}{\omega_{ci}B}\omega k_\perp \tilde{\phi} \tag{1.24}$$

where n_{i0} refers to the equilibrium ion density and a plane wave assumption $\tilde{\phi} \sim \exp\left[i\left(\vec{k}\cdot\vec{r}-\omega t\right)\right]$ was made, which makes $\frac{d\tilde{E}_\perp}{dt} = -\frac{d\nabla_\perp\tilde{\phi}}{dt} = -\omega k_\perp\tilde{\phi}$. Due to the conservation of charge, perpendicular current should be compensated by parallel current, which gives

$$\nabla_\perp \tilde{J}_\perp = -\nabla_{\|}\tilde{J}_{\|} \tag{1.25}$$

From Ohm's law we have

$$\tilde{J}_{\|} = \frac{1}{\eta_{\|}}\left(\tilde{E}_{\|} + \frac{1}{en_0}\nabla_{\|}\tilde{p}\right) = \frac{1}{\eta_{\|}}\left(-ik_{\|}\tilde{\phi} + \frac{k_BT_e}{en_0}ik_{\|}\tilde{n}\right) \tag{1.26}$$

Substitute (1.26) and (1.24) into (1.25) we have a Boltzmann relation

$$\frac{\tilde{n}}{n_0} = \frac{e\tilde{\phi}}{k_BT_e}\frac{\omega_* + ib\sigma_{\|}}{\omega + ib\sigma_{\|}} \tag{1.27}$$

where $b = \frac{k_BT_ek_y^2}{M_i\omega_{ci}^2}$, $\omega_* = -\frac{k_yk_BT_e}{eB_0}\frac{\nabla n_0}{n_0}$, and $\sigma_{\|} = \frac{k_{\|}^2\omega_{ce}\omega_{ci}}{k_y^2\nu_{ei}}$. Combining Eqn. (1.27) with Eqn. (1.22) gives the dispersion relation of resistive drift waves in the limit of $b \ll 1$:

$$\omega^2 + i\sigma_{\|}\left(\omega - \omega_*\right) = 0 \tag{1.28}$$

Solving the above equation when $\sigma_{\|} \gg \omega$ we have

$$\omega \approx \omega_* + i\frac{\omega_*^2}{\sigma_{\|}} \tag{1.29}$$

This shows that with any finite parallel electron dissipation $\mathrm{Im}(\omega)$ is always positive and therefore drift waves are always unstable. They have $\omega_R \approx \omega_*$ and $\frac{\omega_*^2}{\sigma_{\|}}$ is maximum for $b \le 1$.

Comparing the derivation of Eqn. (1.23) and (1.30) we know that the instability depends on the existence of a phase shift between the wave electric field (or plasma potential) and plasma density oscillations. The phase shift could be introduced in the collision-dominated regime by electron-ion collisions and in the collisionless regime by Landau damping through the interaction between electrons and waves [12]. As a result, in the direction parallel to the magnetic field electrons lose their momentum to the background and can not be considered moving freely along the field line. Thus the Boltzmann relation (1.19) is no longer valid, and instead $\tilde{n}/n_0 = \left(e\tilde{\phi}/k_B T_e\right)\left(1-i\delta\right)$ as shown in Eqn. (1.27), where $\delta \neq 0$ [9]. In this case, the charge separation introduced by polarization drift (resulted from the different velocities of ions and electrons in figure 1.4) can not be cancelled therefore instabilities will develop. A more detailed description about the physical pictures of linear drift waves and the linear drift wave instability can be found at [3, 6, 13].

1.3.2 Hasegawa-Wakatani model and Hasegawa-Mima model

The Hasegawa-Wakatani (HW) model [14, 15] is a basic but very useful model which includes necessary components to describe a drift turbulence system: linear drift waves, a mechanism for driving instability, and linear or nonlinear damping mechanism for turbulence saturation. A brief derivation of this model is given in the following. Starting from the electron momentum equation

$$n_e m_e\left(\frac{\partial \vec{u}_e}{\partial t}+\vec{u}_e\cdot\nabla\vec{u}_e\right)=-en_e(-\nabla\phi+\vec{u}_e\times\vec{B})-\nabla p_e-n_e{}^2e^2\xi(\vec{u}_e-\vec{u}_i) \qquad (1.30)$$

where $\xi=\frac{m_e\nu_{ei}}{n_e e^2}$ is electron resistivity and the electron pressure gradient is indicated by ∇p_e, we can obtain the drift velocity perpendicular and parallel to the magnetic field:

$$\vec{u}_e=\vec{u}_{e\perp}+\vec{u}_{e\|}\approx-\frac{\nabla\phi\times\vec{B}}{B^2}+\frac{\nabla p_e\times\vec{B}}{en_eB^2}+\hat{z}\frac{1}{\xi en_e}\left(\frac{\partial}{\partial z}\phi-\frac{1}{en_e}\frac{\partial}{\partial z}p_e\right) \qquad (1.31)$$

where $\hat{z}$ denotes the direction along the magnetic field. Substitute this velocity into the electron continuity equation:

$$\frac{\partial n_e}{\partial t}+\nabla\cdot(n_e\underline{u}_e)=0 \tag{1.32}$$

we have:

$$(\frac{\partial}{\partial t}-\frac{\nabla_\perp\phi\times\vec{B}}{B^2}\cdot\nabla_\perp)\ln n_e=\frac{k_BT_e}{\xi e^2 n_e}\frac{\partial^2}{\partial z^2}\ln n_e-\frac{1}{\xi e n_e}\frac{\partial^2}{\partial z^2}\phi \tag{1.33}$$

Note that $n_e = n_{e0}+\tilde{n}_e$ in Eqn. (1.33). Normalizing the above equation by $\hat{n}_e \equiv \frac{\tilde{n}_e}{n_{e0}}$, $\hat{\phi}\equiv\frac{e\phi}{k_BT_e}$, $\hat{t}\equiv\frac{t}{1/\Omega_{ci}}$, $\hat{\nabla}_\perp \equiv \rho_s\nabla_\perp$, and $\hat{L}_{nr}\equiv L_{nr}/\rho_s$, where $\rho_s\equiv\frac{c_s}{\Omega_{ci}}=\sqrt{\frac{k_BT_e}{M\Omega_{ci}{}^2}}$ is the effective ion Larmor radius, and dropping all “^”, we get:

$$\left(\frac{\partial}{\partial t}-\nabla_\perp\tilde{\phi}\times\hat{z}\cdot\nabla_\perp\right)\left(\tilde{n}+\ln n_0\right)=c_1\left(\tilde{\phi}-\tilde{n}\right) \tag{1.34}$$

where $c_1 = k_\|^2 u_{the}^2/\nu_e\omega_{ci}$ is the “adiabatic parameter”. This is the first equation of the HW model.

Similarly from the ion momentum equation

$$Mn_i(\frac{\partial}{\partial t}+\vec{u}_i\cdot\nabla)\vec{u}_i=en_i(-\nabla\phi+\vec{u}_i\times\underline{B})-\nabla p_i+\mu_\perp\nabla_\perp^2\vec{u}_i \tag{1.35}$$

we can obtain the ion velocity perpendicular to the magnetic field:

$$\vec{u}_{i\perp}=-\frac{\nabla\phi\times\vec{B}}{B^2}-\frac{\nabla p_i\times\vec{B}}{en_iB^2}+\frac{\mu_\perp\nabla_\perp^2\vec{u}_i\times\vec{B}}{en_iB^2}-\frac{M\left(\frac{\partial\vec{u}_i}{\partial t}+\vec{u}_i\cdot\nabla\vec{u}_i\right)\times\vec{B}}{eB^2} \tag{1.36}$$

By combining (1.36) and the ion continuity equation

$$\frac{\partial n_i}{\partial t}+\nabla\cdot(n_i\vec{u}_i)=0 \tag{1.37}$$

and neglecting the ion parallel motion we then have

$$\frac{n_iM}{eB^2}(\frac{\partial}{\partial t}-\frac{\nabla_\perp\phi\times\hat{b}}{B}\cdot\nabla_\perp)\nabla_\perp^2\phi=\frac{k_BT_e}{\xi e^2}\frac{\partial^2}{\partial z^2}(\ln n_i-\frac{e\phi}{k_BT_e})+\frac{\mu_\perp}{eB^2}\nabla_\perp^4\phi \tag{1.38}$$

Following the same normalizations as applied to (1.33), the second equation of the HW model can be obtained

$$\left(\frac{\partial}{\partial t}-\nabla_\perp\tilde{\phi}\times\hat{z}\cdot\nabla_\perp\right)\nabla_\perp^2\tilde{\phi}=c_1\left(\tilde{\phi}-\tilde{n}\right)+c_2\nabla_\perp^4\tilde{\phi} \qquad (1.39)$$

where $c_1 = k_{\|}^2 u_{the}^2 / \nu_e \omega_{ci}$ is the "adiabatic parameter" and $c_2 = \mu_{ii} / \rho_s^2 \omega_{ci}$ is the normalized ion viscosity. Here $k_{\|}$ is the wavenumber along magnetic field line, u_{the} is the electron thermal speed, and ν_e is the electron collision frequency. The adiabatic parameter is related to the electron parallel dynamics and quantifies the degree that a Boltzmann relation between density and potential fluctuations is maintained. The coupled equations (1.34) and (1.39) together comprise the HW weak turbulence model.

When $c_1 \sim 1$ electron parallel momentum will be damped hence there exist a phase shift between density and potential fluctuations, and the Boltzmann relation is no longer valid. The new relation is $\tilde{n}/n_0 = \left(e\tilde{\phi}/k_B T_e\right)\left(1-i\delta\right)$, where the phase shift δ is the key for instability. For $c_1 \ll 1$, which means electrons can hardly move along the magnetic field line, (1.34) reduces to the two-dimensional Euler equation. Drift waves become turbulent typically when $\rho_s / L_n \ll 1$ and $c_2 \ll 1$, which makes the convective derivative term in the ion momentum equation important [16]. In our experiments this condition is satisfied by $c_1 \approx 1$, $\rho_s / L_n \approx 0.3-0.5$, and $c_2 \approx 0.2-0.3$ inside the plasma [16].

For $c_1 \gg 1$ electrons can move very rapidly along magnetic field line to cancel out any excessive charges. This will lead to a Boltzmann relation between density and potential hence the drift waves are linearly stable. In this case by adding equations (1.34) and (1.39) together we will recover the Hasegawa-Mima (HM) model [16, 17]:

$$\frac{\partial}{\partial t}\left(\tilde{\phi}-\nabla_{\perp}^{2}\tilde{\phi}\right)-\left[\left(\nabla_{\perp}\tilde{\phi}\times\hat{z}\right)\cdot\nabla_{\perp}\right]\nabla_{\perp}^{2}\tilde{\phi}-\frac{1}{L_n}\frac{\partial}{\partial y}\tilde{\phi}=0 \tag{1.40}$$

By looking at the two coupled equations of HW model, we can see that HW model has retained the polarization drift term $\frac{\partial}{\partial t}\nabla_{\perp}^{2}\tilde{\phi}$. It makes the ion motion perpendicular to the B field no longer incompressible ($\nabla_{\perp}\cdot\tilde{u}_{\perp}\neq 0$) and leads to a charge separation, which combined with any mechanism associated with electron parallel momentum dissipation will lead to drift wave instability thus generate drift wave turbulence in plasmas. The HW model has also included the nonlinear terms $\nabla_{\perp}\tilde{\phi}\times\hat{z}\cdot\nabla_{\perp}\left(\nabla_{\perp}^{2}\tilde{\phi}\right)$ and $\nabla_{\perp}\tilde{\phi}\times\hat{z}\cdot\nabla_{\perp}\left(\tilde{n}+\ln n_0\right)$. These two terms originally come from the convective nonlinear terms $\vec{u}\cdot\nabla_{\perp}\vec{u}$ and $\vec{u}\cdot\nabla_{\perp}n$, which effectively introduce the mechanism of turbulent energy exchange among different turbulent frequencies or spatial scales. Figure 1.5 shows the temporal evolution of the energy spectrum $E_k=\frac{1}{2}\left(\left|n_k\right|^2+k^2\left|\phi_k\right|^2\right)$ from numerical simulation, which suggests that there is an inverse energy transfer to the small wavenumber region [15].

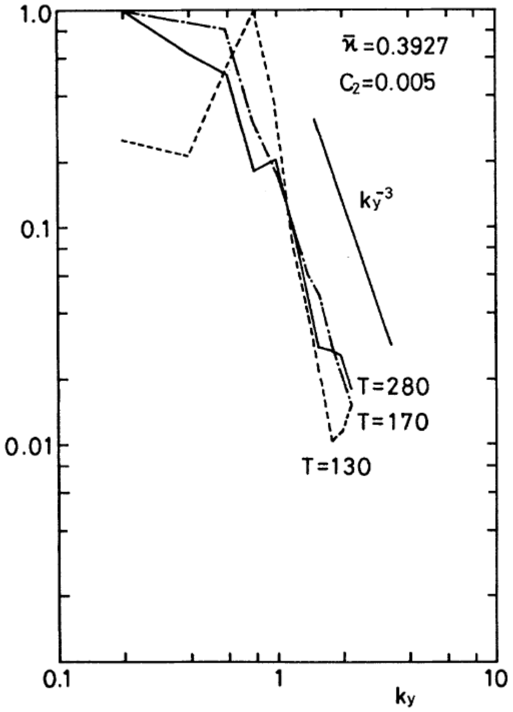

Figure 1.5 The temporal evolution of the energy spectrum $E_k = \frac{1}{2}\left(|n_k|^2 + k^2|\phi_k|^2\right)$ [15].

In 1979, Hasegawa et al. studied the nonlinear dynamics of drift waves using numerical simulations, and found that the potential fluctuation forms a closed potential surface, which is the consequence of the generation of toroidally and poloidally symmetric m=n=0 potential structures through inverse energy transfer from the drift wave kinetic energy with perpendicular wavenumber in the range $0.1 < k_\perp \rho_s < 1$, as shown in figure 1.6 [18]. Therefore the HW model naturally included the physics of generating turbulence and nonlinearly redistributing the turbulent energy to other scales, which we will see in the next section naturally lead to the formation of zonal flows.

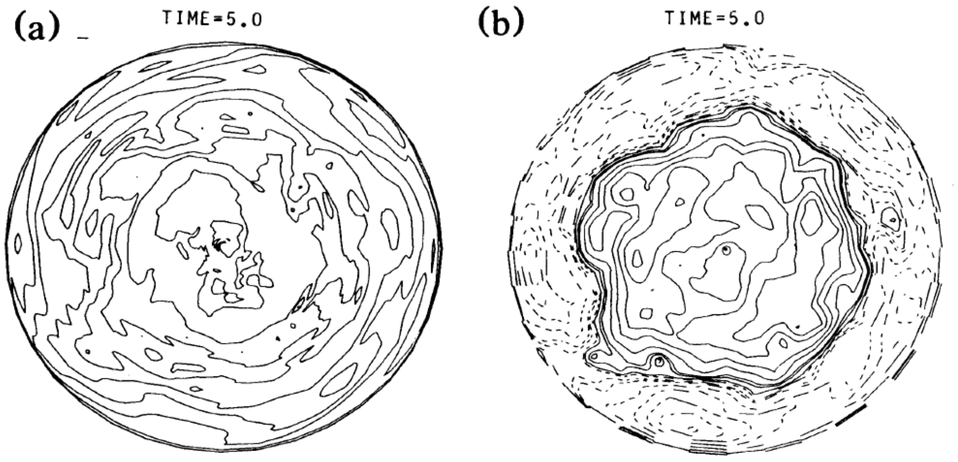

Figure 1.6 The density contour (a) and potential contour (b) from the numerical simulation of the electrostatic plasma turbulence. The closed iso-potential contours indicate that an azimuthally directed, radially sheared flow has been generated [18].

1.4 Theoretical understanding of zonal flows generation and their back-reaction on turbulence

In the context of tokamak plasmas, zonal flow refers to the toroidally (also predominantly azimuthally) symmetric but radially localized band-like flow structures, i.e., it is an n=m=0 electrostatic fluctuation with finite radial wavenumber. It got its name because of its similarities to the large scale quasi-two-dimensional atmospheric and oceanic flows along the latitude line in geophysics, where “zonal” here means latitudinal. Another feature of zonal flow is that it has a zero frequency. Figure 1.7 shows a schematic of the typical structures of zonal flows [11]. It is clear in the figure that the associated $\vec{E}\times\vec{B}$ flow is in the poloidal direction, and its sign changes with radius.

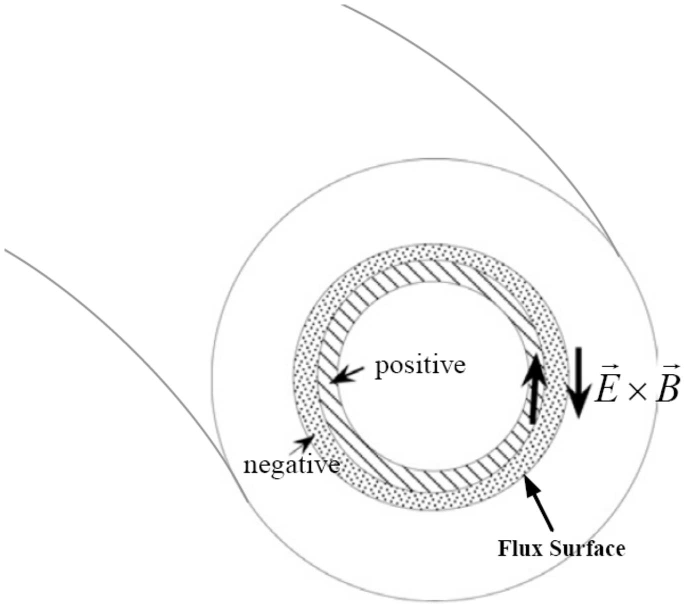

Figure 1.7 Zonal electric field and zonal flow. The poloidal cross-section is shown here, where the hatched region and dotted region denote the positive and negative charges respectively [11].

In a cylindrical plasma, the zonal flows are in the direction of diamagnetic drift velocity. However in a torus the magnetic field deviates from the geodesic lines (defined as curves whose tangent vectors remain parallel if they are transported along the curves), the $\vec{E}\times\vec{B}$ drift velocities at neighboring points are no longer parallel to each other. This will lead to a nonzero divergence of the $\vec{E}\times\vec{B}$ drift, and thus a compression of plasma density. If the flows are constrained to the magnetic surface, i.e. $V_r = 0$, then the divergence of the poloidal flow $\nabla_{\perp}\cdot V_{\theta}$ either can be compensated by a parallel flow $\nabla_{\|}\cdot V_{\|}$ ($V_{\|} = -2qV_{\theta}\cos\theta$, where q is the safety factor), which leads to the zero frequency zonal flows (m=n=0), or can be relaxed by launching a sound wave

($\omega_{GAM} = \sqrt{2}c_s / R$, where R is the major) along the magnetic field line, which is called the geodesic acoustic mode (GAM, m=1, n=0) [9, 19-21]. In the following part of this thesis, “zonal flows” refers to the zero frequency zonal flows and the other branch of zonal flow with finite frequency is referred to as “GAM” unless otherwise specified. Figure 1.8 from [20] shows the physical mechanism for the density compression caused by geodesic curvature and the helical structure of zonal flows.

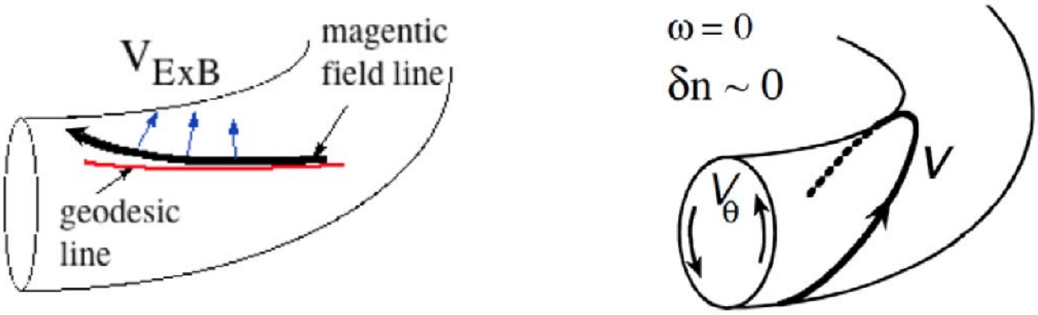

Figure 1.8 (a) The magnetic field and $\vec{E} \times \vec{B}$ drift. The fact that the magnetic field line deviates from the geodesic line causes the compression of plasma. (b) The helical zonal flows in a torus [20].

Because zonal flows occur within a magnetic flux surface where plasma pressure $p = const.$, they cannot tap expansion free energy stored in the temperature, density gradient, etc. that are normal to the surface, and as a result they can only be driven by nonlinear interactions that transfer energy from drift waves into this n=m=0 mode. Thus the generation of zonal flows naturally reduces the intensity and the level of transport caused by drift wave turbulence. This is the main reason why the research on zonal flows has been carried out so extensively in magnetic confinement fusion. Also because of their symmetry, zonal flows do not generate additional energy or particle transport, and are not subject to Landau damping and primarily damped by collisional processes. All the above features are thought to make zonal flows a benign reservoir of free energy in the system [11].

The generation of zonal flows by turbulence is closely related to the inverse energy cascade in two-dimensional fluid turbulence, where the dynamics are fundamentally different from those of three-dimensional turbulent flows. In 3D turbulence the vortex tube has the freedom to stretch along the vortex axis, i.e., $\frac{\partial V_z}{\partial z} \neq 0$ (here z is along the vortex axis). This stretching process is associated with an increase of vorticity in the stretching direction due to the conservation of angular momentum, and for incompressible flows the lengthening along the vortex axis will lead to a thinning in the direction perpendicular to the axis due to volume conservation of fluid element. As a result, this stretching allows a production of enstrophy (mean squared vorticity defined as $\varepsilon \equiv \frac{1}{2}\int_S \left|\nabla \times \vec{u}\right|^2 \, ds$) and a cascade of kinetic energy from large to small vortices, i.e. from lower to higher wavenumbers, where both the energy and enstrophy is strongly dissipated via viscosity. This is the well-known direct energy cascade [22]. However in 2D turbulence by definition the stretching along vortex axis does not occur, i.e., $\frac{\partial V_z}{\partial z} = 0$, and both the enstrophy and kinetic energy are conserved [23]. In this case the kinetic energy will be transferred from small to large vortices, while the enstrophy will be transferred from large to small vortices [23].

In strongly magnetized plasmas the turbulence is approximately 2D since the turbulent correlation length along B field is much larger than the correlation length perpendicular to B, thus making the zonal flow formation in plasma very similar to the inverse energy cascade in 2D fluid turbulence. Note that there is at least one major difference between these two nonlinear energy transfer processes: zonal flow formation involves a direct interaction between small scales and large scales, and is a non-local interaction in wavenumber space, while the inverse energy cascade proceeds via a series of local couplings [11]. Zonal flows can be thought of as being generated by turbulence via three wave coupling that satisfies the wavenumber constraint $\vec{k}_1 + \vec{k}_2 = \vec{k}_{ZF}$, where $\vec{k}_1$ and $\vec{k}_2$ are the wavenumbers of turbulence, and $\vec{k}_{ZF}$ denotes the zonal flow wavenumber. Figure 1.9 shows the thin triangle for generating zonal flows by drift wave turbulence, where we can see that the wavenumbers of drift waves are much bigger than that of the zonal flow $\vec{k}_1,\ \vec{k}_2 \gg \vec{k}_{ZF}$.

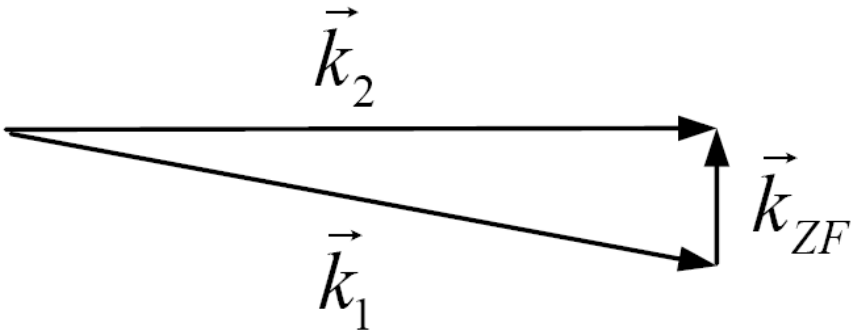

Figure 1.9 The generation of zonal flows by drift wave turbulence via three wave (triad) coupling. The wavenumbers of drift waves are much bigger than that of the zonal flow $\vec{k}_1,\ \vec{k}_2 \gg \vec{k}_{ZF}$, indicating a non-local energy transfer in wavenumber space[11].

The turbulence drive mechanism of zonal flows has been described by a simple model [9, 24]:

$$\frac{\partial}{\partial t}\overline{V}_{ZF} = -\frac{\partial}{\partial x}\left\langle \tilde{v}_x \tilde{v}_y \right\rangle - \nu_d \overline{V}_{ZF} \tag{1.41}$$

where $\overline{V}_{ZF}$ denotes the zonal flow velocity, and ν_d is the elective zonal flow damping rate. Here x and y denote the radial and azimuthal (or poloidal) direction respectively. The time-averaged quantity $\left\langle \tilde{v}_x \tilde{v}_y \right\rangle$ is the turbulent momentum flux, and also known as the *Reynolds stress*. It plays the role of redistributing momentum among different spatial locations but does not inject or dissipate momentum into or out of the plasma system. The divergence of such a momentum flux then corresponds to the concentration or diffusion of momentum, thus should be closely related to the velocity profiles in plasmas.

Another feature of zonal flows that makes them a focus of fusion plasma research is that they can shear turbulent eddies into smaller ones. At smaller scales, eddies will have a stronger coupling to dissipation, thus zonal flow shearing can effectively reduce the turbulence intensity and the resulting turbulent transport. Zonal flows present a spatio-temporally complex shearing pattern, as shown in figure 1.10 (a) [21]. In position space the zonal flows shearing is random because zonal flows have complex spatial structures, i.e., the signs and amplitudes of zonal flow rotations in the poloidal direction are random variables of radial position; while in the time domain although zonal flows have a zero-mean frequency the zonal flow shearing is also random because zonal flows are with random life times. Thus the shearing could be considered as a random diffusive process consists of many short kicks, as shown in figure 1.10 (b). The change of turbulence wavenumber, $\vec{k}_r$, due to the zonal flow shearing is considered diffusive in wavenumber space and could be modeled as [11]:

$$\left\langle \delta k_r^2 \right\rangle = D_k t \tag{1.42}$$

where the turbulent diffusion rate is $D_k = k_\theta^2 \left\langle \tilde{V}_{ZF}^{'2} \right\rangle \tau_c$, and $\left\langle \cdots \right\rangle$ denotes the average.

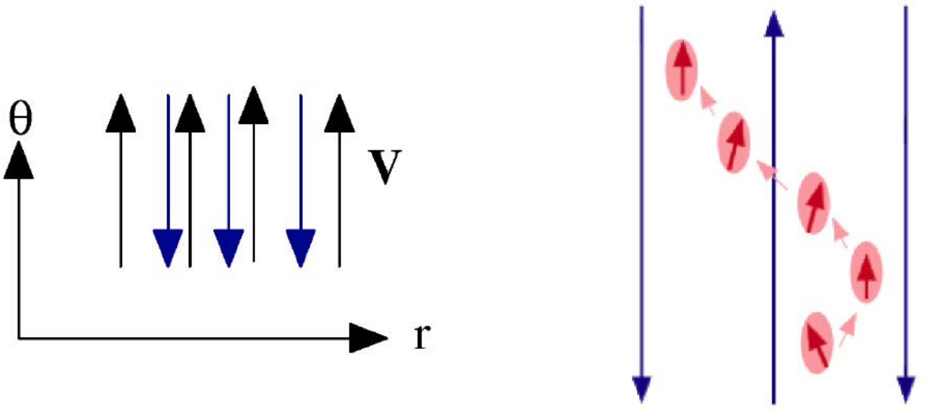

Figure 1.10 (a) (Left) spatially complex structures of zonal flows. (b) (Right) zonal flow shearing is a random, diffusive process consists of a series of kicks [21].

Based on the above discussion, we can clearly see that drift wave turbulence and zonal flows are closely coupled: on the one hand drift turbulence can generate large scale zonal flows through the typical three-wave interaction, in which small-scale turbulent eddies nonlinearly transfer their kinetic energy and momentum into a large-scale zonal structure to maintain it against damping; on the other hand zonal flows can actively shear turbulent eddies into smaller ones, at which scale the dissipation of kinetic energy and enstrophy of those smaller eddies are stronger. Both of the generation and shearing processes of zonal flows can effectively reduce the turbulence intensity and the resulting turbulent energy and particle transport, thus will lead to a better plasma confinement.. Also note that both the mean shear flow and the zonal flow can reduce the transport by altering the wave-particle interaction time, which determines the “cross-phase”, even for fixed turbulence intensity. Due to this feedback loop between zonal flows and turbulence, plasma turbulence now can be regarded as a combination of drift waves and zonal flows, which interact with each other and self-regulate to reach an equilibrium state, are often referred to as drift wave-zonal flow turbulence. This process is schematically shown in figure 1.11 [10, 11].

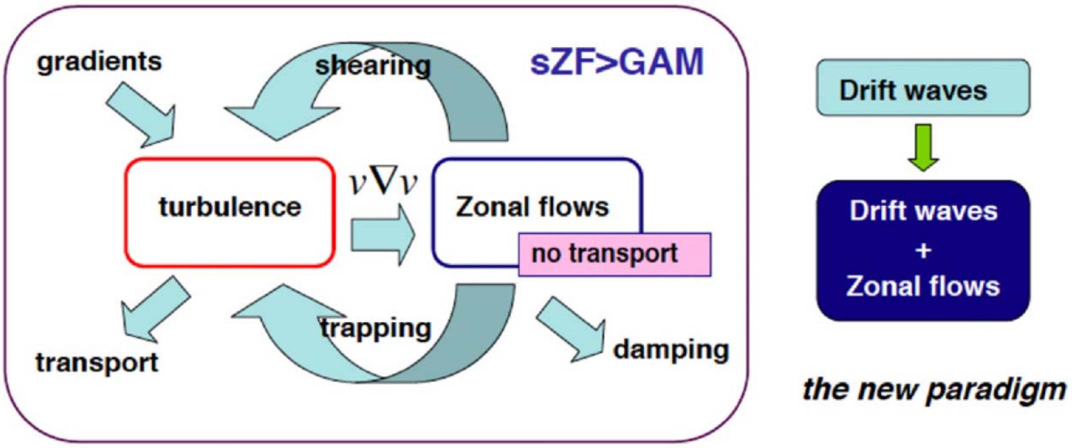
gradients
shearing
sZF>GAM
turbulence
$v\nabla v$
Zonal flows
no transport
transport
trapping
damping
Drift waves
Drift waves
+
Zonal flows
the new paradigm

Figure 1.11 The paradigm of drift wave-zonal flow system for plasma turbulence. Density or temperature gradients generate turbulence, which causes an enhanced turbulent transport. And the generated turbulence also nonlinearly transfer their energy and momentum to zonal flows, in which process reduces the turbulence intensity. Zonal flows will also give a back-reaction on turbulence to further reduce its intensity by either shearing or trapping. Due to their symmetry, zonal flows do not contribute to transport, and therefore serve as benign reservoir of free energy in the system [10].

Finally it is also important to note the difference between zonal flows and the mean shear flow, which can also exist in the plasma. First, zonal flows are exclusively driven by turbulence through nonlinear coupling. Therefore if there is no turbulence, there will be no zonal flow; while the mean shear flow can either be driven by turbulence [24] or neoclassical ion orbit loss [20], or can be externally excited by techniques such as electrode biasing [25, 26] or momentum input. Second, zonal flow shearing is spatially and temporally random, which increases the turbulence radial wavenumber $\vec{k}_r$ through a diffusive process. As we can see from Eqn. (1.42), $\vec{k}_r$ increases as $\sim t^{1/2}$; while the coherent shearing generated by the mean shear flow increases $\vec{k}_r$ as $\sim t$ [11]. Therefore both type of shear flows act to reduce the turbulent transport. For a detailed discussion of the difference please refer to the review paper [11].

References:

[1] International Energy Outlook 2009, DOE/EIA-0484 (2009), Washington DC, May 2009. Available online: http://www.eia.doe.gov/oiaf/ieo/index.html

[2] J. D. Lawson, Proceedings of the Physical Society B, Vol. 70, p. 6 (1957)

[3] J. Wesson, Tokamaks, 2nd edition, Clarendon Press-London 1997

[4] J. Nuckolls, A. Thiessen, L. Wood, and Zimmerma.G, Nature **239**, 139 (1972)

[5] http://www.plasmas.org/rot-energy.htm

[6] F. F. Chen, Introduction to Plasma Physics and Controlled Fusion, Volume 1, Second Edition, Plenum Press, New York, 1984

[7] R. J. Hawryluk, S. Batha, W. Blanchard, Phys. Plasmas **5**, 1577-1589 (1998).

[8] W. Horton, Rev Mod Phys **71** (3), 735-778 (1999).

[9] G. R. Tynan, A. Fujisawa and G. McKee, Plasma Phys. Control. Fusion **51**, 13001 (2009).

[10] A. Fujisawa, Nucl. Fusion **49**, 013001 (2009)

[11] P. H. Diamond, S. I. Itoh, K. Itoh and T. S. Hahm, Plasma Phys. Control. Fusion **47**, R35-R161 (2005).

[12] Hans R. Griem and Ralph H. Lovberg, Methods of Experimental Physics, Part A, Academic Press, New York and London, 1970

[13] F. F. Chen, Phys. Fluids 8, 912 (1965)

[14] A. Hasegawa and M. Wakatani, Phys. Rev. Lett. 50, 682 (1983)

[15] M. Wakatani and A. Hasegawa, Phys. Fluids 27, 611 (1984)

[16] Z. Yan, Ph.D. thesis, Turbulence-driven shear flow and self-regulating drift wave in a cylindrical plasma device (2008)

[17] A. Hasegawa and K. Mima, Phys. Fluids 21, 87 (1978)

[18] A. Hasegawa and M. Wakatani, Phys. Rev. Lett. 59, 1581 (1987)

[19] N. Winsor, J. L. Johnson, and J. M. Dawson, Phys. Fluids 11, 2448 (1968)

[20] K. Itoh and S. I. Itoh, Plasma Phys. Control. Fusion 38, 1 (1996)

[21] K. Itoh, S. I. Itoh, P. H. Diamond, A. Fujisawa, Y. Nagashima, M. Yagi, A. Fukuyama, T. S. Hahm, K. Hallatschek, and G. R. Tynan, First ITER International Summer School, p. 106 (2007)

[22] E. Pope, Turbulent Flow, Cambridge University Press (2002)

[23] R. H. Chraichnan, Phys. Fluids 10, 1417 (1967)

[24] P. H. Diamond and Y. B. Kim, Phys. Fluids B 3, 1626 (1991)

[25] R. J. Taylor and M. L. Brown et al, Phys. Rev. Lett. 63,2365 (1989)

[26] R. J. Taylor and L. Oren, Phys. Rev. Lett. 43,446 (1979)

Chapter 2

Previous experimental research on the plasma drift wave-zonal flow system

2.1 The link between turbulence and confinement

Drift turbulence can come from a variety of free energy sources. When there is significant ion heating, it can be generated via a type of instability driven by ion temperature gradient (ITG) [1, 2]; similarly when there is strong electron heating, the electron temperature gradient (ETG) could be large enough to trigger the ETG turbulence [3]; the presence of trapped particles can also lead to instabilities, such as the trapped electrons mode (TEM), which can be driven by a combined effect of trapped electron collisions and electron temperature gradient [4-6]. For laboratory plasma or the edge tokamak plasmas, the collisional or resistive drift turbulence can occur. Figure 2.1 presents the heavy ion beam probe (HIBP, which measures the plasma density and potential by injecting singly charged ions [7]) measurements in ISX-B tokamak, which shows that density and potential fluctuations drastically depart from the Boltzmann relation at the edge $\rho > 0.95$, indicating that parallel electron dissipation is strong in this region [8].

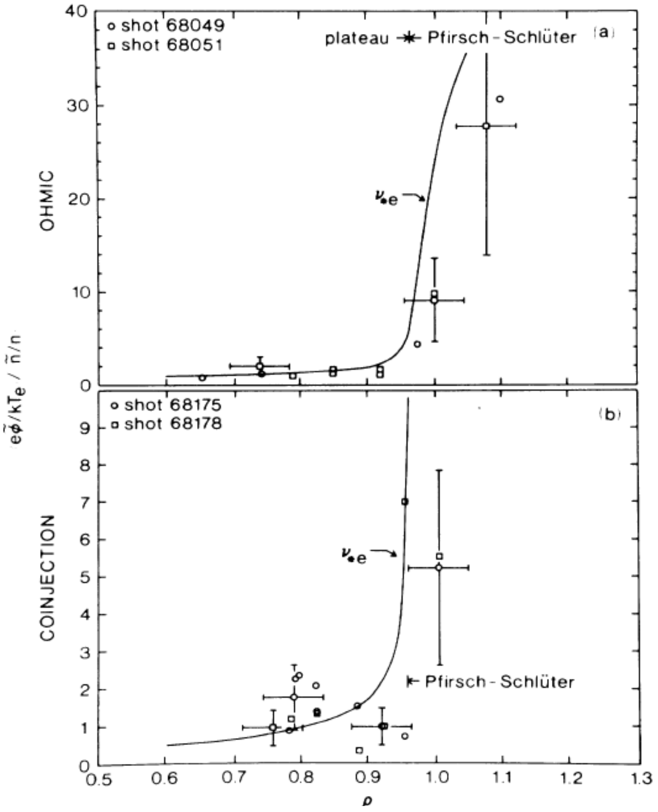

Figure 2.1 The ratio of normalized plasma potential to normalized density fluctuations is plotted out as a function of radius. The ratio is significantly bigger than the expected value ~1 for the case of adiabatic electrons. (a) is for ohmic discharge and (b) is L-mode discharge [8].

In a variety of toroidal confinement experiments, the turbulent particle/heat flux appears to be within about a factor of 2 of the value needed to explain the observed global confinement. The parametric variations of particle or heat confinement and turbulence have been studied in many experiments. In these cases, the flux is integrated over the flux surface and the resulting total particle or heat loss is compared against expectations from global confinement measurement. For example, measurements in ISX-B, figure 2.2 [8], showed that the total particle flux of beam-heated discharges is an order of magnitude larger compared to ohmic discharges, which is consistent with changes in global confinement. In the beam heated discharges, the convective thermal electron heat flux was roughly consistent (within a factor of 2) with global energy confinement time.

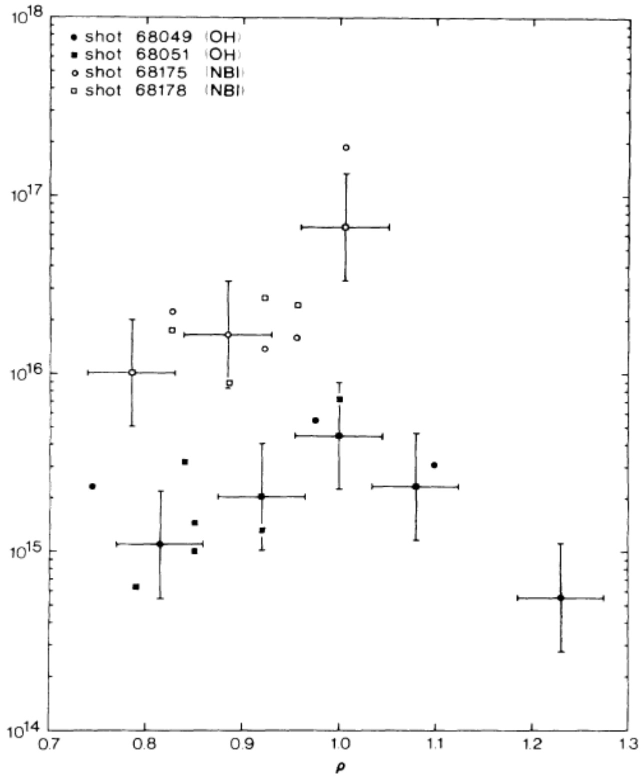

Figure 2.2 Radial profiles of turbulent particle flux in the ISX-B tokamak. The empty squares correspond to the case with neutral beam heating, and the filled squares are for the case without beam heating [8].

The first measurement of the convective and conducted turbulent heat flux was carried out in the TEXT tokamak [9], as is shown in figure 2.3. The results showed that turbulent fluctuations were dominantly responsible for the energy loss at the edge region, and sufficient to explain the loss of heat from the core plasma; but deeper in the plasma the convective turbulent heat flux was much lower than the flux estimated to be exhausted from the plasma core, suggesting that some other mechanism such as turbulent conduction by temperature fluctuations could be responsible for the loss of heat in the core plasma region.

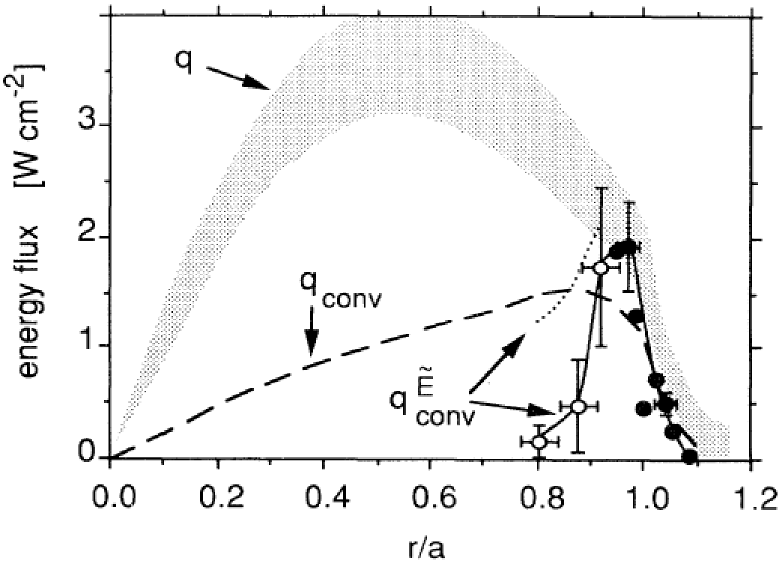

Figure 2.3 Radial profiles of total ion and electron heat flux from power balance q (shaded area), the total convective heat flux q_{conv} predicted by a neutral-penetration code and H_{α} measurements, and the turbulence-introduced heat flux $q^{\tilde{E}}_{conv}$ [9].

2.2 Existence of zonal flows in plasmas

The first identification of zero-frequency zonal flows [10, 11] where ions are magnetized was carried out on the CHS heliotron (R=1.0 m, a=0.2 m, B=0.9 T) using two heavy ion beam probes (HIBP) [7]. These two HIBPs were toroidally separated by 90°, as shown in figure 2.4 (a). The waveforms of fluctuations at two toroidal locations are quite identical with each other if the two observation points are on the same magnetic flux surface (figure 2.4 (b)). If the two observation points are located on slightly different flux surface the fluctuations are with a constant phase difference determined by the separation distance in the radial direction. These above observations apparently confirmed the symmetry of zonal flows in the toroidal direction and the finite $\vec{k}_r$ in the radial direction. Recently the zonal flow symmetry in the poloidal direction was confirmed by a L-mode discharge in DIII-D (R=1.73 m, a=0.6 m, B=2.0 T) using a beam emissions spectroscopy (BES) [12], where for the two observation points separated by 1.2 cm in the poloidal direction no poloidal phase shift was found for the lower frequency region $f < 10\ kHz$ (but with a finite coherence 0.15-0.3 between these two channels).

The 3D structures of the GAM was also investigated in HL-2A (R=1.65 m, a=0.4 m, B=2.3-2.4 T) for an ohmic discharge, which confirmed the symmetry of GAMs in the toroidal and poliodal directions, and the finite correlation length in the radial direction was also observed [13].

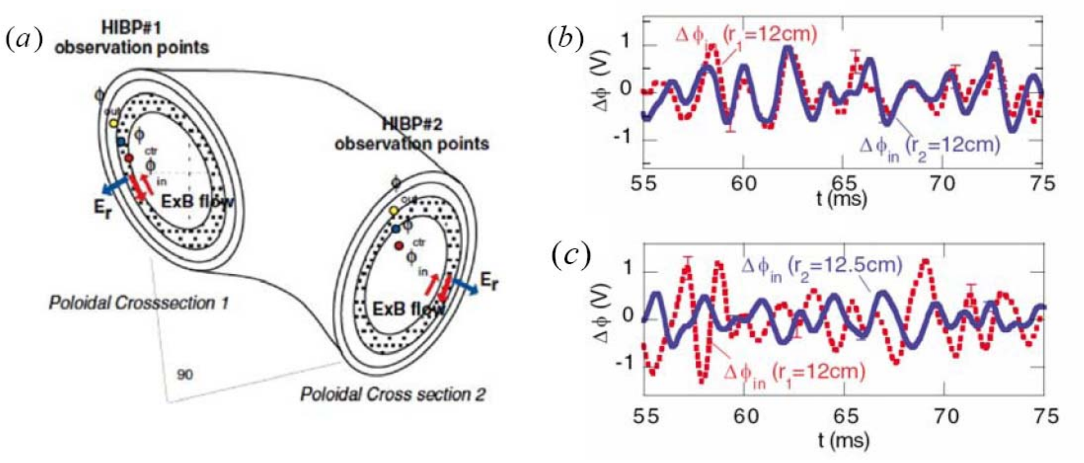

Figure 2.4 Zonal flow structure measurement in CHS. (a) The position of the two toroidally separated twin HIBPs. (b) Waveforms of the electric field (or potential difference) on the same magnetic flux surface at difference toroidal positions. (c) Waveforms of the electric field (or potential difference) on slightly different magnetic flux surface at different toroidal positions [10, 11].

The research on the generation of shear/zonal flows by turbulence is strikingly important simply because they can serve as a tool to suppress turbulence and the resulting turbulent transport. The process in which turbulence drives zonal flows is essentially the process in which small-scale turbulent fluctuations nonlinearly transfer their energy and momentum to large-scale zonal flows. The first experiment to attempt to study how the energy is nonlinearly transferred from high k to low k region was performed on the TEXT tokamak [14]. The one fluid model suitable for weak parallel dissipation used there was formed in the wavenumber domain. Therefore a sufficient high spatial resolution was needed for actually computing the nonlinear energy transfer function. Due to experimental limitations, two poloidally separated Langmiur probes were used to measure the density fluctuations and the relevant spectral analysis was done on frequency domain since Ritz argued that a frozen flux approximation could be safely used. It was found that the energy in the linearly unstable frequency range (30 to 110 kHz) was transferred predominantly to the linearly stable frequency range (10 to 40 kHz). Recent work on the TJ-K stellarator measured the two-field nonlinear energy transfer in the wave number domain [15]. The results are qualitatively consistent with the turbulence drive mechanism of zonal flows, with kinetic energy transferred to larger scale and energy associated with density transferred to smaller scales. The nonlinear energy transfer measurement was also carried out on the H1-heliac toroidal machine (R=1.0 m, a=0.2 m) by using both the above one fluid model developed by Ritz et al. and the amplitude correlation technique [16], which showed that the energy associated with floating potential nonlinearly coupled from unstable frequency region (20-50 kHz) into the lower frequency region (0-15 kHz) associated with large coherent structures, and into the broad band turbulence region.

2.3 Effects of zonal flows on turbulence

Only a few experimental observations have been made on the interaction between zonal flow and turbulence. Figure 2.5 shows the turbulence modulation due to the stationary zonal flows in CHS [17, 18], where the comparison between the waveforms of turbulence and the zonal flow power shows that the turbulence power increases (decreases) when the power of zonal flow decreases (increases). This anti-correlation clearly demonstrates that stationary zonal flows can modulate turbulence.

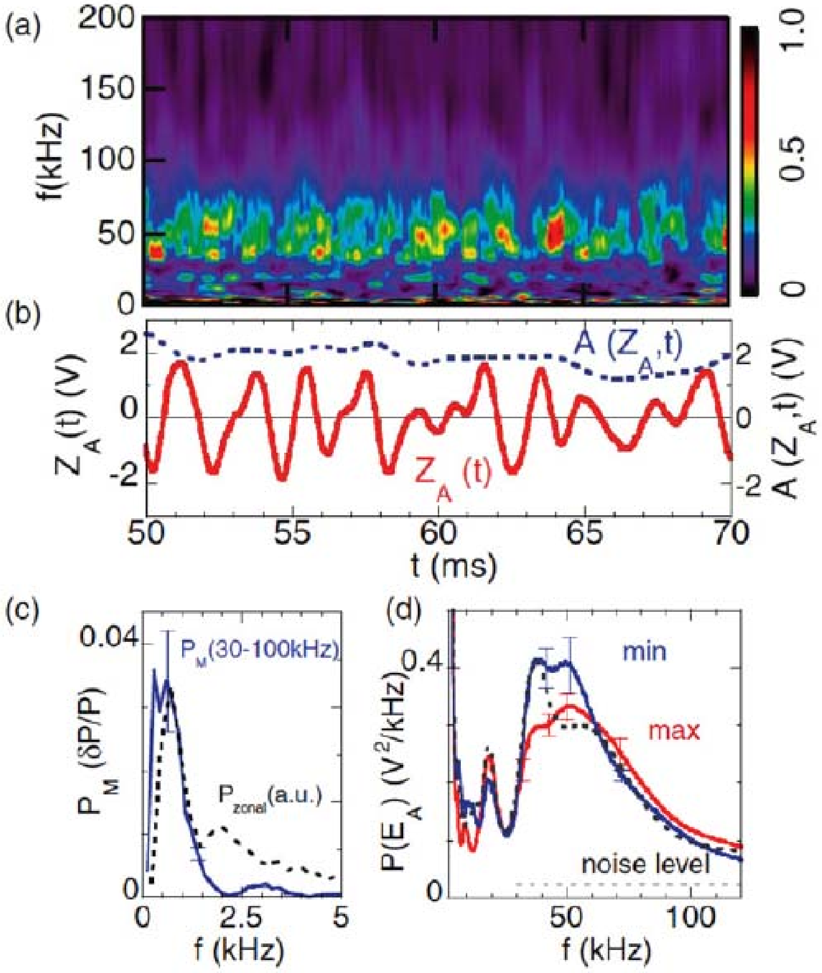

Figure 2.5 Turbulence modulation due to stationary zonal flows in CHS [17, 18]. (a) Evolution of the wavelet spectrum of electric field. (b) Evolution of zonal flows $Z_A(t)$. (c) FFT spectrum of wavelet power evolution of frequencies 30 to 100 kHz. (d) Conditional averages of wavelet power spectra around the maxima and minima of the zonal flow.

Similar observations have shown that GAMs modulate turbulence amplitude. Figure 2.6 shows such a modulation, and there exists an anti-correlation between the envelope of density fluctuation and GAMs [19].

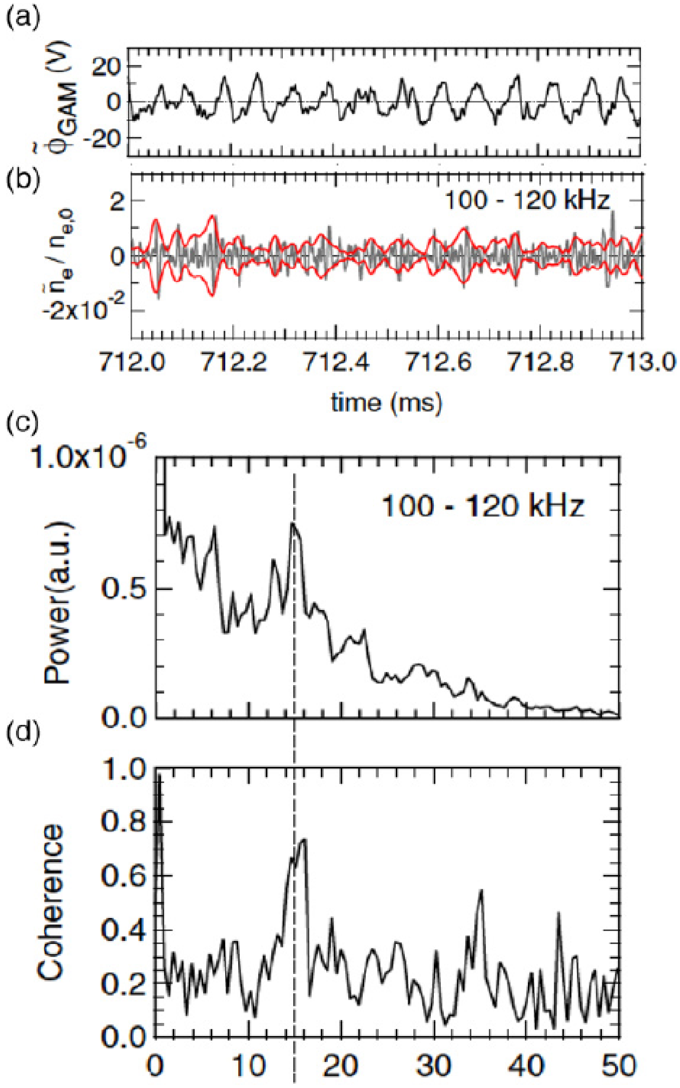

Figure 2.6 Turbulence modulation due to GAM in JFT-2M [19]. (a) GAM fluctuation. (b) The ambient density fluctuation. (c) Power spectrum of the envelope of density fluctuation. (d) Coherence between GAM and density fluctuation.

2.4 Mean shear effects on turbulence and transport

When it comes to the question of how shear/zonal flows can suppress turbulence and make a better confinement, we must mention the high confinement mode (H-mode). The discovery of H-mode is probably one of the most important things that have happened in nuclear fusion research. In 1982 H-mode was found in the “old” ASDEX tokamak (which is now in China as HL-2A) [20, 21]. When enough neutral beam heating (NBI) power was injected into the plasma, the energy confinement time was observed to spontaneously double from the previous low confinement regime, and the energy, particle, impurity and momentum transport were improved simultaneously. This type of behavior has been subsequently observed in many different tokamaks, such as PDX [22], DIII-D [23], and JET [24], etc., and finally in the W7-AS stellarator [25]. The change of the confinement is first apparent at the edge of plasma where there is a rapid increase in the pressure gradient mainly due to the increase in edge density. Thus the edge can be thought of as having a transport barrier, inside which the density gradient is very high. When this edge transport barrier (ETB) appears, the density of the whole plasma volume increases on the confinement time scale. It is generally accepted that the improved confinement is due to the turbulence reduction by a $\vec{E}\times\vec{B}$ shear flow developed at the edge of plasmas. The PCI (Phase Contrast Imaging) measurement in DIII-D showed that in the region where there is a strong electric field the turbulent radial correlation length is significantly decreased [26]. Figure 2.7 was taken from [26] to show this turbulent correlation length reduction during the L-mode to H-mode transition. Note that in figure 2.7 (b) the turbulent correlation length was reduced roughly by a factor of two, and figure 2.7 (c) shows the L-H transition through the D_α emission intensity (a measure of the recycling between the plasma and the surrounding surfaces). The Langmuir probe measurement in DIII-D also suggested that the plasma poloidal rotation plays a critical role in the L-H transition, which implied that the physics introduces this rotation determines the transition.

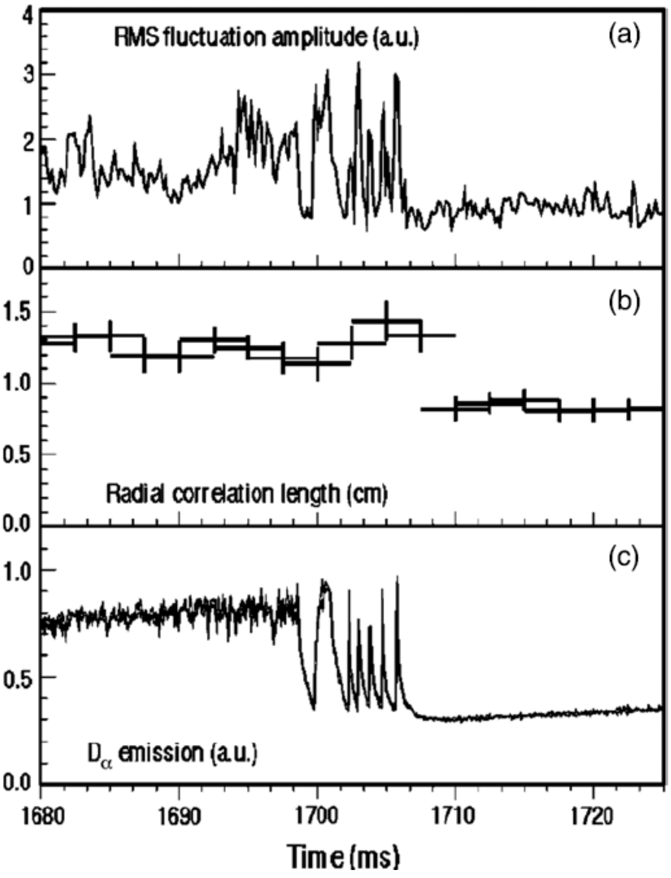

Figure 2.7 (a) RMS fluctuation amplitude shows a reduction of fluctuation intensity in the H-mode regime. (b) Turbulent radial correlation length. (c) D_α light emission from the separatrix region [26].

The turbulent particle flux inferred from the correlation of density and potential fluctuations was found to be greatly reduced across the whole edge and SOL (scrape-off layer) region, as shown in figure 2.8 [27], when plasma develops from L-mode to H-mode phase. The particle flux reduction is due to both changes in turbulence amplitude and cross-phase between density and potential fluctuations.

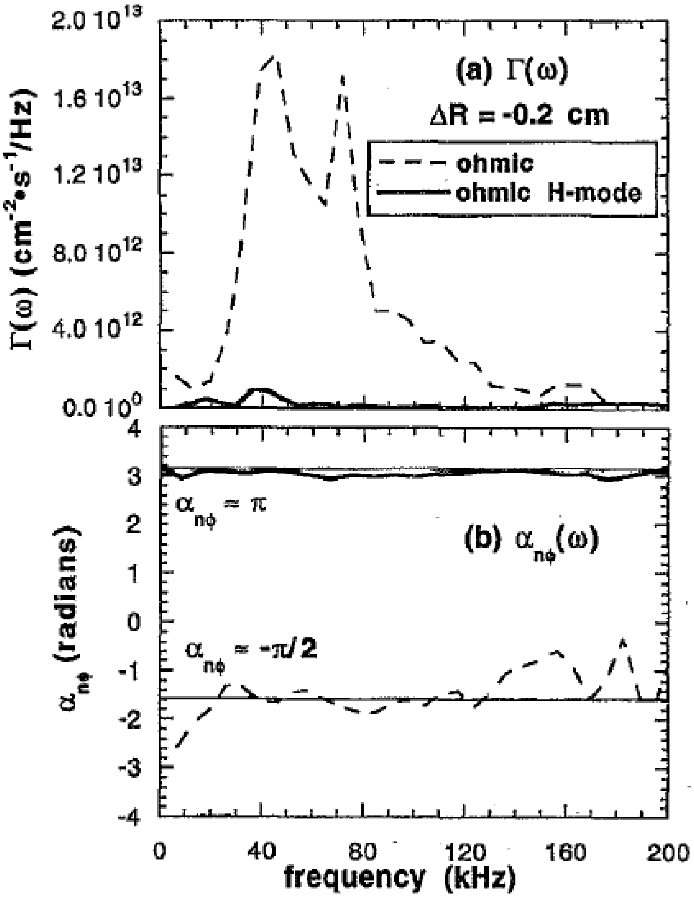

Figure 2.8 (a) The frequency resolved turbulent particle flux and (b) density potential cross-phase in the ohmic and ohmic H-mode [27].

Although H-mode has been discovered for almost 30 years, and there have been substantial experimental and theoretical efforts put into it, the physics origin or trigger behind H-mode has not been quite understood, most notably the sudden suppression (or disappearance) of edge turbulence with its driving source (the gradients) increase. To verify if the mean shear flow is really triggered by turbulence via a nonlinear process akin to zonal flow generation a simultaneous measurement of the turbulence and shear flow intensity is necessary but not enough. A direct measurement of the energy flow into the shear flow would be sufficient and conclusive. Equivalently if there is a transfer of momentum from the turbulence to the shear flows to maintain them against damping, a measurement of the turbulent momentum flux (i.e., Reynolds stress) profile and the shear/zonal flow intensity profile evolution would be very useful. Unfortunately for both case, no such experiment has ever been done on strong magnetized plasmas. This is mostly because both of the above verifications require a multi-channel plasma potential measurement, which is difficult in high performance tokamaks. One possible way is through HIBP, which is very expensive; another way is by Langmiur probe array, which is much cheaper but can only be placed at edge under very limited occasions. For lower temperature laboratory plasmas detailed measurements are made possible through Langmiur probe arrays to test these theoretical pictures. Motivated by these considerations we give a brief summary of experiments done on the linear laboratory plasma device (CSDX).

2.5 Previous experiments on CSDX

The Controlled Shear Decorrelation Experiment (CSDX) is a linear plasma device in University of California, San Diego. CSDX is a 2.8 m long linear helicon plasma device equipped with a 13.56 MHz half wave-length azimuthally symmetric (RF wavefields have azimuthal mode number m=0) helicon source with a radius r_{src}=4.5cm, which typically produces a plasma with an on-axis density ~ 10^{13} cm^{-3} and on-axis electron temperature ~3 eV. The typical operation magnetic field is 0.1 T, and the injected RF power is 1.5kW (reflected power less than 30 W), and the gas fill pressure is 3.2 mTorr. A number of experiments have been done on CSDX, including a controlled transition from coherent drift wave oscillations to drift turbulence [28]; evidence for the turbulence-drive mechanism of the spontaneous rotation in the device [29, 30]; a study of the statistical properties of Reynolds stress [31]; and evidence for a edge-drive mechanism through the influence of residual stress at the plasma boundary [32].

The plasma in CSDX is very stable and very repeatable, and it will make a gradual transition from coherent drift wave fluctuations into a turbulent regime as the magnetic field is increased. Figure 2.9 shows the transition process [28]. It is clear that when the magnetic field increases from 500 Gauss to 1000 Gauss, potential fluctuations evolve from a combination of discrete modes into a broadband turbulent stage. Also notice that at 700 Gauss there develops one single dominating coherent mode at 10 kHz.

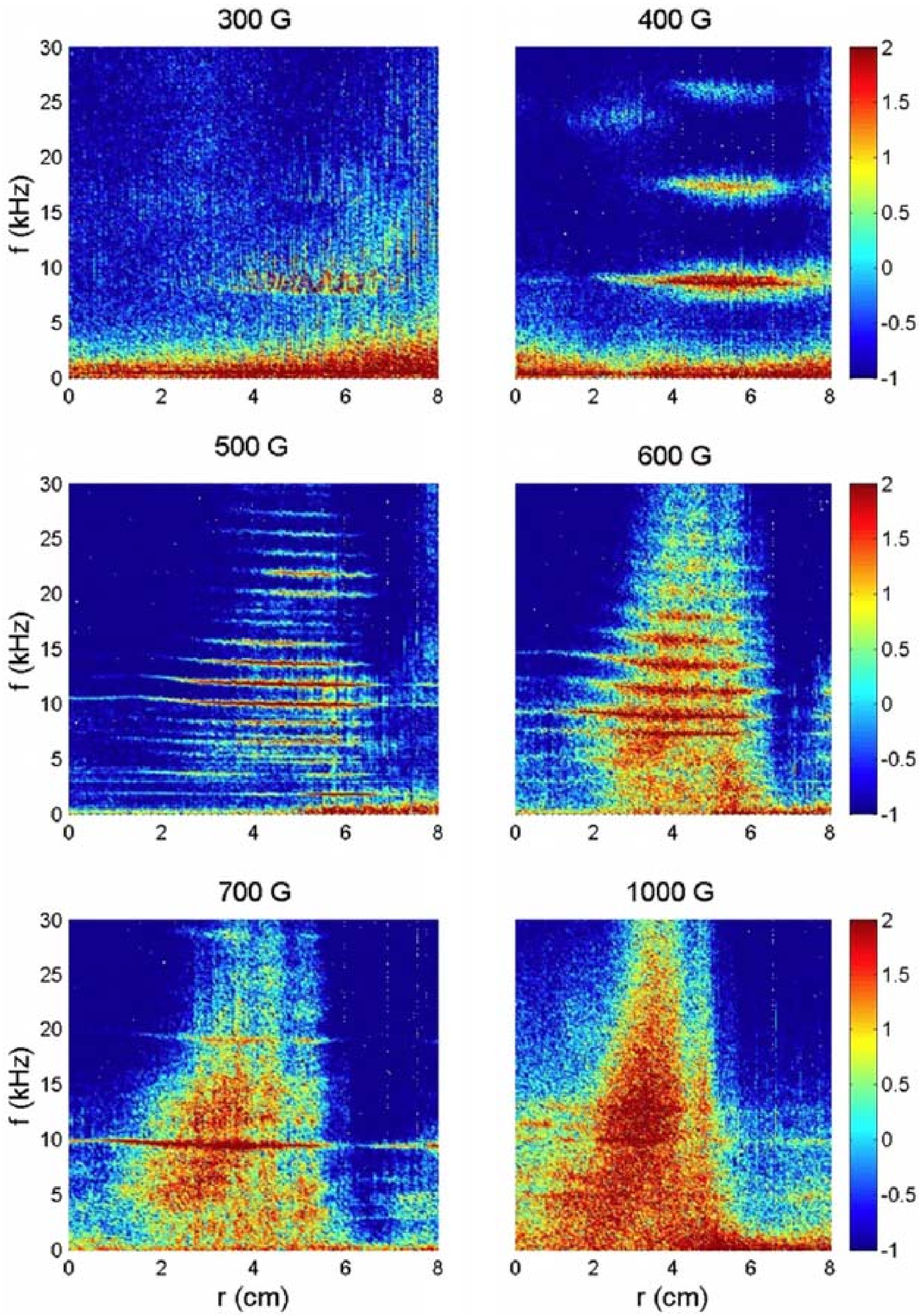

Figure 2.9 The spatially resolved spectrum for floating potential at different magnetic field. It is clear that when the magnetic field increases from 500 Gauss to 1000 Gauss, potential fluctuations evolves from a combination of discrete modes into a broadband turbulent stage [28].

As the magnetic field increases, the energy contained in the linearly stable fluctuations with low wavenumbers ($k_\perp \rho_s \leq 0.5$) increases over a factor of 100, while the energy contained in those linearly unstable fluctuations with intermediate wavenumbers ($k_\perp \rho_s \sim 1-2$) increases by only a factor of 2-3 (shown in figure 2.10). The energy in these linearly stable modes must come from a nonlinear process, implying that there exists a nonlinear transfer of energy from the linearly unstable region into the linearly stable region, which seems to be consistent with the theory of fluctuations driven shear flow.

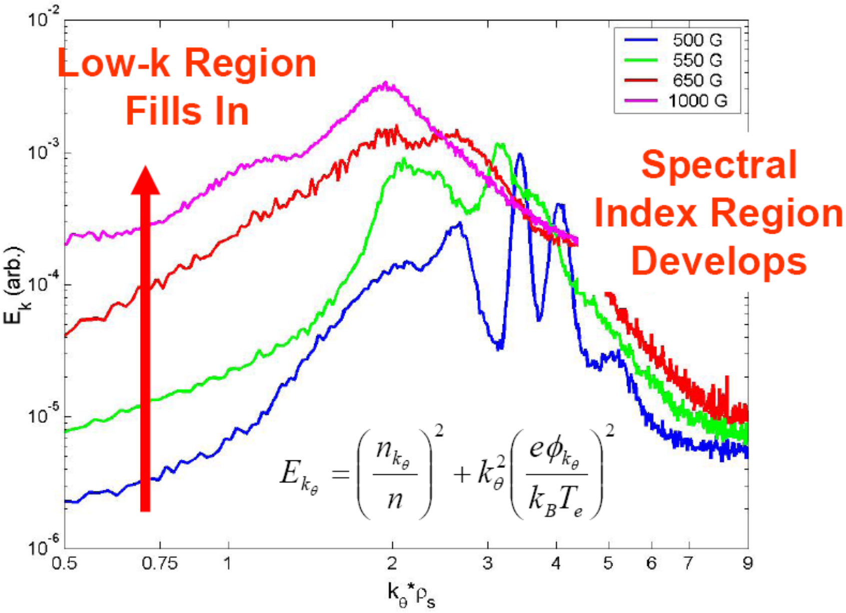

Figure 2.10 Azimuthal wavenumber spectral evolution suggests an inverse energy transfer [28].

As will be shown in chapter 3, the nonlinear terms $n(\vec{u}\cdot\nabla n)$ or $\vec{u}\cdot(\vec{u}\cdot\nabla\vec{u})$ in the modified plasma continuity or momentum equation are the only terms responsible for redistributing turbulent energy among different turbulent frequencies or spatial scales through nonlinear wave-wave interactions. In the Fourier domain, these two terms correspond to the 3-wave interaction, i.e., two waves beating with each other to generate the 3rd wave, of which the amount of energy transferred can be quantified by bispectra. Therefore we can infer that 3-wave interaction is the only process that nonlinearly transfers the turbulent energy in the Fourier domain from the linearly unstable wavenumber regions to the linearly stable regions.

By using a Langmiur probe array, the plasma ion velocity in the azimuthal direction could be obtained by using Mach probe and the time-delay estimation techniques [33]. It was found that the plasma spontaneously rotates in the azimuthal direction even without any external momentum input, and the time average rotation speed has a velocity shear, as is shown in figure 2.11 [34]. An azimuthal momentum conservation analysis was done by substituting the experimentally measured Reynolds stress profile into an azimuthal momentum balance equation given below

$$\frac{1}{r^2}\frac{\partial}{\partial r}\left(r^2\left\langle \tilde{u}_r\tilde{u}_\theta\right\rangle\right)=-\nu_{i-n}\left\langle u_\theta\right\rangle+\mu_{ii}\left[\frac{1}{r}\frac{\partial}{\partial r}\left(r\frac{\partial\left\langle u_\theta\right\rangle}{\partial r}\right)-\frac{\left\langle u_\theta\right\rangle}{r^2}\right] \tag{2.1}$$

where $\left\langle \tilde{u}_r\tilde{u}_\theta\right\rangle$ is the Reynolds stress computed from floating potential channels, ν_{i-n} is the ion-neutral collision rate, and μ_{ii} is the ion viscosity, and then estimating the ion-neutral drag and ion viscosity, and then finally solving the equation to infer the time average azimuthal velocity profile [29]. The result is shown in figure 2.11 by the black solid line, which agrees well with the Mach probe data (blue curve) and the TDE measurement (black diamonds).

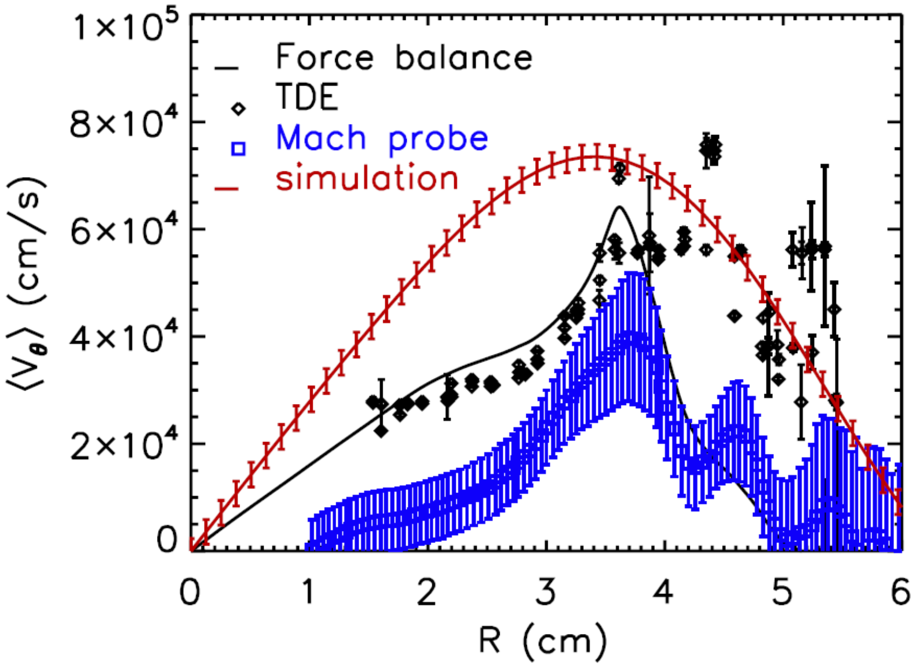

Figure 2.11 Both the Mach probe data (blue curve) and the TDE inferred azimuthal velocity (black diamonds) show that there is a shear flow in the plasma. The black solid line is the inferred velocity from turbulent momentum conservation analysis, which agrees well with the Mach probe and TDE measurement. The red curve is from a two-field turbulence simulation and is consistent with the experimental measurements [34].

Based on the above analysis, it was concluded that the turbulent Reynolds stress determines the spatial distribution of azimuthal momentum throughout the plasma. But one natural question to ask when staring at the described azimuthal profiles is: why does the velocity shear exist at the plasma edge? A comparison of the Reynolds stress profile against the velocity profile can partly answer this question. Figure 2.12 (c) shows the Reynolds stress profile and 2.12 (e) is the velocity profile. Note that the maximum negative Reynolds stress gradient lies in the same region (shaded) as the maximum azimuthal velocity, which is consistent since a negative divergence means a concentration of turbulent momentum. This result apparently implies that turbulence carries momentum from other radial positions and concentrates it at the edge region.

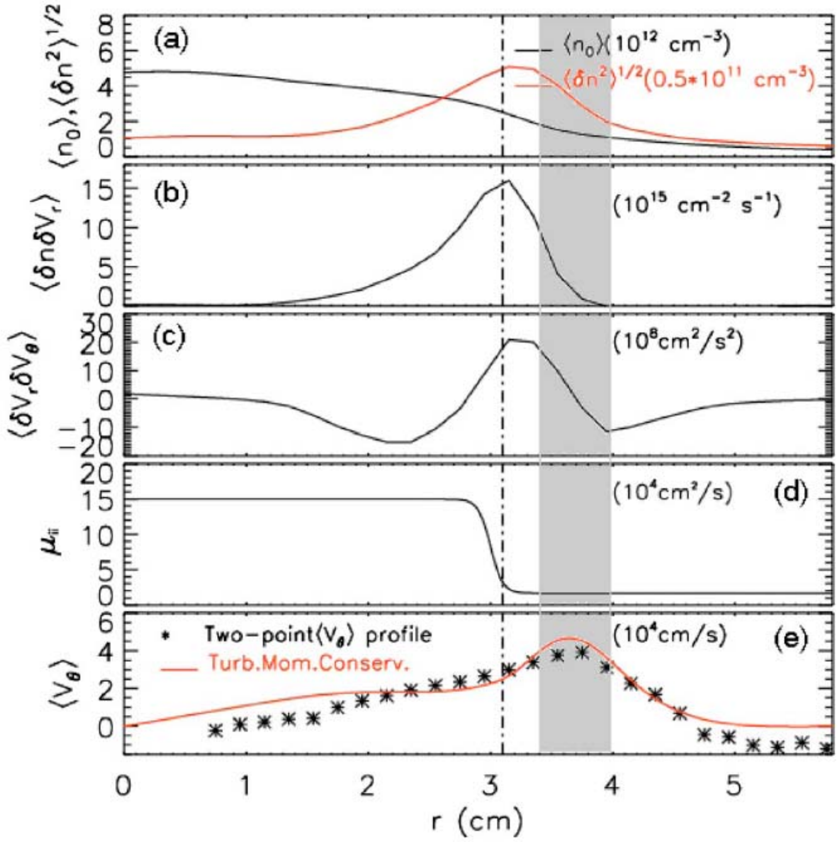

Figure 2.12 Plasma equilibrium profiles. (a) Density (solid black) and RMS of density fluctuation (solid red). (b) Turbulent particle flux. (c) Reynolds Stress. (d) Estimated ion viscosity. (e) Plasma azimuthal velocity [31].

But other closely related questions remain unanswered, including: why is the momentum concentrated at the edge? What makes the edge region special from other radial positions in the plasma ? Where does the net azimuthal momentum come from?

Recent experiments suggest an edge drive mechanism to explain the origin of the azimuthal momentum [32]. The experiment was based on the calculation of a non-diffusive turbulent momentum transport term which has been also termed the *residual stress*. Generally the Reynolds stress term, which is the total turbulent momentum transport, can be modeled as [35]:

$$\left\langle \tilde{u}_r \tilde{u}_\theta \right\rangle = -\chi_\theta \frac{\partial \left\langle u_\theta \right\rangle}{\partial r} + V_r^{eff} \left\langle u_\theta \right\rangle + S_{r\theta}^{res} \tag{2.2}$$

where χ_θ is the turbulent diffusivity, V_r^{eff} is the convective velocity (pinch velocity), and $S_{r\theta}^{res}$ is the residual stress. Due to the symmetry of the plasma in CSDX, the pinch term is estimated to be zero since it relies on the presence of trapped particles. By estimating turbulent diffusivity from the turbulent correlation time $\chi_\theta = \left\langle \tilde{u}_r^2 \right\rangle \tau_c$ and measuring the azimuthal velocity profile, the diffusive momentum transport term can be constructed and subtracted from the total momentum flux $\left\langle \tilde{u}_r \tilde{u}_\theta \right\rangle$, thus inferring the residual stress term. Figure 2.13 (e) shows the resulting residual stress profile, which peaks at the plasma edge. When combined with a no-slip boundary condition in the outer regions (r>5cm or so) due to strong flow damping by neutral gas in this region, this turbulent stress then gives rise to a net plasma fluid rotation in the observed direction [32].

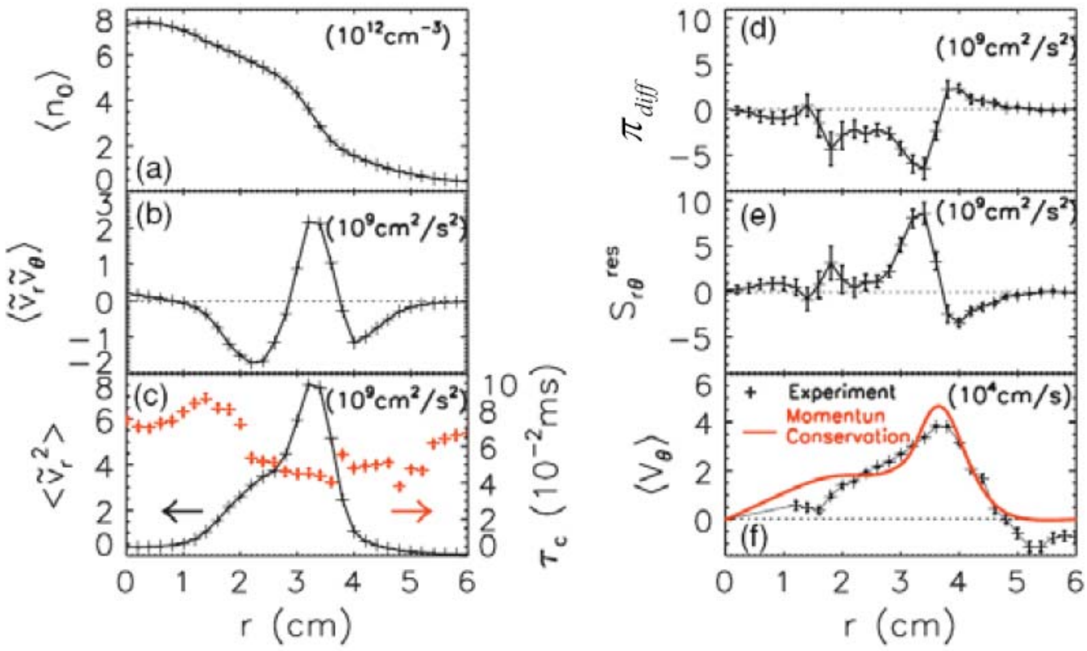

Figure 2.13 Inferring the residual stress term and relevant profiles. (a) Equilibrium density. (b) Reynolds stress. (c) Mean square of turbulent radial velocity. (d) Constructed diffusive turbulent transport term, $\pi_{diff} = -\chi_\theta \frac{\partial \langle u_\theta \rangle}{\partial r}$. (e) Inferred residual stress. (f) Equilibrium azimuthal velocity [32].

2.6 Motivation behind the dissertation

The above sections merely summarize the extensive efforts from both experimentalists and theorists on the turbulence and shear/zonal flows studies. We now have a better understanding of the anomalous transport problems, particularly we have shifted from the basic concept of “drift wave turbulence” to the new “drift wave-zonal flow turbulence” paradigm, which shows that drift waves and zonal flows are inherently interdependent on each other and the plasma system is a self-regulating system. The existence of zero-frequency zonal flow and GAM has been confirmed in experiments through the measurement of their symmetry properties [10, 11, 36, 37]. It is now believed that zonal/shear flows do regulate and suppress turbulence and the cross-field transport but there are only very limited and inconclusive observations actually supporting the turbulence-drive mechanism of shear/zonal flows, especially in tokamaks.

Despite the great efforts spent on this drift wave-zonal flow problem, at least from the experimental side our understanding is very basic and there are far more questions asked than answered. Some of the unanswered questions include: Can we find direct microscopic evidence that shear/zonal flows are really generated by turbulence through nonlinear processes? How big will the zonal flows intensity be? This will involve the linear and nonlinear saturation mechanism of zonal flows, and the branching ratio of energy between turbulence and zonal flows, i.e., what fraction of the free energy will flow to shear/zonal flows and what fraction will flow to turbulence. Of course the effectiveness of the shear/zonal flows back-reaction on turbulence is also very important. What is the origin of intrinsic rotation (which the plasma rotates itself without external momentum input)? This is important since the rotation can lead to a better confinement. In future fusion reactors the H-mode regime will be the operating regime. Thus we at least need to know the origin of the L-H transition. There are limited observations suggesting that shear flow is the key to the L-H transitions and that turbulence feeds the shear flow, but there are contradictory observations as well [34].

Motivated by these considerations this dissertation work was oriented to answer two inherently related questions:

(1) How is the turbulent energy and momentum redistributed over different scales and frequencies? Previous time domain analysis on CSDX showed that turbulence mediates the turbulent momentum transport throughout the plasma, and that the turbulent Reynolds stress profile is quantitatively consistent with the time-averaged azimuthal velocity profile, as seen in the previous section. This proved that turbulence drives the shear flow. But in order to answer what components (frequency or scale) of the turbulence drives the shear flow, we need to directly measure the nonlinear energy transfer between turbulence and shear flows in Fourier domain.

(2) What is the underlying turbulent dynamics that leads to the nonlinear energy and momentum transfer from turbulence into shear flow? To answer this question, we need both the statistical analysis from probe measurement and the dynamic picture from the fast imaging. Answering this question will also help to identify the origin of the sheared flow.

The rest of this dissertation is arranged as the following: Chapter 3 presents all relevant methods used in the dissertation, and comments and discussions are made as needed.

In chapter 4, the turbulent energy transport equations for density and velocity (or potential) fluctuations are derived in the frequency domain, and a detailed design of the dual 3x3 Langmiur probe array used to measure the nonlinear energy transfer rates is given. Bispectral data analysis method has also been explained and discussed. Finally initial experimental results are presented.

Chapter 5 applies this technique and presents the nonlinear energy transfer measurement results, which clearly show that turbulent energy with intermediate frequencies (~10kHz), which correspond to azimuthal mode number m~3 fluctuations, are nonlinearly coupled to low frequency azimuthally symmetric sheared flows. This means that the large-scale sheared azimuthal flows in CSDX are nonlinearly driven by small-scale turbulent fluctuations. The radial flux of vorticity is found to be dominantly responsible for the nonlinear kinetic energy transfer to the sheared flows.

Chapter 6, based on a combined study of the dual 3x3 probe array and fast imaging, proposes a physics picture for the statistical results of nonlinear energy transfer into sheared flows, in which drift wave packet structures with density and vorticity fluctuations are nonlinearly generated in the central plasma pressure gradient region, then as they spiral out and approach an axisymmetric, radially sheared azimuthal flow located at the plasma boundary they are azimuthally tilted, stretched, and finally absorbed into the shear layer. This is the mechanism that amplifies a pre-existing shear flow. Similar mechanisms likely operate at the edge of confined toroidal plasmas and should lead to the amplification of sheared flows at the boundary of these devices as well.

The last chapter 7 concludes the dissertation by a summary and discussions about future plans.

References:

[1] H.T. Evensen, R.J. Fonck, S.F. Paul, G. Rewoldt, S.D. Scott, W.M. Tang and M.C. Zarnstorff, Nucl. Fusion 38, 237 (1998)

[2] C. L. Rettig, T. L. Rhodes, J. N. Leboeuf, W. A. Peebles, E. J. Doyle, G. M. Staebler, K. H. Burrell, and R. A. Moyer, Phys. Plasmas 8, 2232 (2001)

[3] T. L. Rhodes, W. A. Peebles, M. A. Van Zeeland, J. S. deGrassie, R. V. Bravenec, K. H. Burrell, J. C. DeBoo, J. Lohr, C. C. Petty, X. V. Nguyen, E. J. Doyle, C. M. Greenfield, L. Zeng, and G. Wang, Phys. Plasmas 14, 056117 (2007)

[4] J. Wesson, Tokamaks, 2nd edition, Clarendon Press-London 1997

[5] F. Ryter, C. Angioni, A. G. Peeters, F. Leuterer, H. U. Fahrbach, and W. Suttrop, Phys. Rev. Lett. 95, 085001 (2005)

[6] G.D. Conway, C. Angioni, R. Dux, F. Ryter, A.G. Peeters, J. Schirmer, C. Troester, Nucl. Fusion 46, S799 (2006)

[7] F. H. Mull, T. P. Crowley, P. M. Schoch, and K. A. Connor, Rev. Sci. Instrum. 70, 959 (1999)

[8] G. A. Hallock, A. J. Wootton, and R. L. Hickok, Phys. Rev. Lett. 59, 1301 (1987)

[9] C. P. Ritz, R. V. Bravenec, P. M. Schoch, R. D. Bengtson, J. A. Boedo, J. C. Forster, K. W. Gentle, Y. He, R. L. Hickok, Y. J. Kim, H. Lin, P. E. Phillips, T. L. Rhodes, W. L. Rowan, P. M. Valanju, and A. J. Wootton, Phys. Rev. Lett. **62**, 1844-1847 (1989).

[10] A. Fujisawa, K. Itoh, H. Iguchi, K. Matsuoka, S. Okamura, A. Shimizu, T. Minami, Y. Yoshimura, K. Nagaoka, C. Takahashi, M. Kojima, H. Nakano, S. Ohsima, S. Nishimura, M. Isobe, C. Suzuki, T. Akiyama, K. Ida, K. Toi, S. I. Itoh and P. H. Diamond, Phys Rev Lett **93**, 165002 (2004).

[11] A. Fujisawa, K. Itoh, A. Shimizu, H. Nakano, S. Ohshima, H. Iguchi, K. Matsuoka, S. Okamura, T. Minami, Y. Yoshimura, K. Nagaoka, K. Ida, K. Toi, C. Takahashi, M. Kojima, S. Nishimura, M. Isobe, C. Suzuki, T. Akiyama, T. Ido, Y. Nagashima, S. I. Itoh and P. H. Diamond, Phys. Plasmas **15**, 055906 (2008).

[12] D. K. Gupta, R. J. Fonck, G. R. McKee, D. J. Schlossberg and M. W. Shafer, Phys Rev Lett **97**, 125002 (2006).

[13] T Lan, A D Liu, C X Yu, L W Yan, W Y Hong, K J Zhao, J Q Dong, J Qian, J Cheng, D L Yu and

Q W Yang, Plasma Phys. Control. Fusion 50, 045002 (2008)

[14] C. P. Ritz, E. J. Powers, and R. D. Bengtson, Phys. Fluids **B 1**, 153 (1989)

[15] P Manz, M Ramisch, U Stroth, V Naulin and B D Scott, Plasma Phys. Control. Fusion **50** 035008 (2008)

[16] H. Xia and M. G. Shats, Phys. Rev. Lett. 91, 155001 (2003)

[17] A. Fujisawa, Nucl. Fusion **49**, 013001 (2009).

[18] A. Fujisawa et al, J. Phys. Soc. Japan 76, 033501 (2007)

[19] Ido T. et al, Plasma Phys. Control. Fusion 48, S41 (2006).

[20] F. Wagner, G. Becker, K. Behringer, D. Campbell, A. Eberhagen, W. Engelhardt, G. Fussmann, O. Gehre, J. Gernhardt, G. v. Gierke, G. Haas, M. Huang, F. Karger, M. Keilhacker, O. Klüber, M. Kornherr, K. Lackner, G. Lisitano, G. G. Lister, H. M. Mayer, D. Meisel, E. R. Müller, H. Murmann, H. Niedermeyer, W. Poschenrieder, H. Rapp and H. Röhr, Phys Rev Lett **49**, 1408 (1982).

[21] F. Wagner, Plasma Phys. Control. Fusion 49, B1 (2007)

[22] S. M. Kaye, M. G. Bell, K. Bol et al., J Nucl Mater **121**, 115 (1984).

[23] K. H. Burrell, S. Ejima, D. P. Schissel, N. H. Brooks, R. W. Callis, T. N. Carlstrom, A. P. Colleraine, J. C. DeBoo, H. Fukumoto, R. J. Groebner, D. N. Hill, R. M. Hong, N. Hosogane, G. L. Jackson, G. L. Jahns, G. Janeschitz, A. G. Kellman, J. Kim, L. L. Lao, P. Lee, J. M. Lohr, J. L. Luxon, M. A. Mahdavi, C. P. Moeller, N. Ohyabu, T. H. Osborne and D. Overskei, Phys Rev Lett **59**, 1432 (1987).

[24] A. Tanga, K. H. Behringer, A. E. Costley, M. Brusati, B. Denne, A. Edwards, A. Gibson, R. D. Gill, N. Gottardi, R. Granetz, P. J. Harbour, H. Jackel, M. Keilhacker, E. Lazzaro, M. Malacarne, P. D. Morgan, P. Noll, J. Orourke, P. E. Stott, D. R. Summers, J. A. Tagle and P. R. Thomas, Nucl Fusion **27**, 1877 (1987).

[25] V. Erckmann, F. Wagner, J. Baldzuhn, R. Brakel et al., Phys Rev Lett **70**, 2086 (1993).

[26] S. Coda, M. Porkolab, and K. H. Burrell, Phys. Rev. Lett. 273, 125 (2000)

[27] R. A. Moyer et al, Phys. Plasmas 2, 2397 (1995).

[28] M. J. Burin, G. R. Tynan, G. Y. Antar, N. A. Crocker, and C. Holland, Phys. Plasmas **12**, 052320 (2005)

[29] C. Holland, J. H. Yu, A. James, D. Nishijima, M. Shimada, N. Taheri and G. R. Tynan, Phys. Rev. Lett. **96,** 195002 (2006)

[30] G. R. Tynan, C. Holland, J. H. Yu, A. James, D. Nishijima, M. Shimada, and N. Taheri , Plasma Phys. Control. Fusion **48,** S51 (2006)

[31] Z. Yan, J. H. Yu, C. Holland, M. Xu, S. H. Muller, and G. R. Tynan, Phys. Plasmas **15,** 092309 (2008)

[32] Z. Yan, M. Xu, P. H. Diamond, C. Holland, S. H. Muller, G. R. Tynan, J. H. Yu, Phys. Rev. Lett. **104**, 065002 (2010)

[33] J. H. Yu, C. Holland, G. R. Tynan, G. Antar and Z. Yan, J Nucl Mater **363**, 728-732 (2007).

[34] G. R. Tynan, A. Fujisawa and G. McKee, Plasma Phys. Control. Fusion **51**, 13001 (2009).

[35] P. H. Diamond, C. J. McDevitt, O. D. Gurcan, T. S. Hahm, W. X. Wang, E. S. Yoon, I. Holod, Z. Lin, V. Naulin and R. Singh, Nucl Fusion **49**, 045002 (2009)

[36] T. Lan, A. D. Liu, C. X. Yu, L. W. Yan, W. Y. Hong, K. J. Zhao, J. Q. Dong, J. Qian, J. Cheng, D. L. Yu and Q. W. Yang, Plasma Phys Contr F **50**, 095002 (2008).

[37] A. D. Liu, T. Lan, C. X. Yu, H. L. Zhao, L. W. Yan, W. Y. Hong, J. Q. Dong, K. J. Zhao, J. Qian, J. Cheng, X. R. Duan and Y. Liu, Phys Rev Lett **103**, 095002 (2009)

Chapter 3

Experimental setup and data analysis methods

In this chapter, a brief description of the experimental hardware, including the CSDX linear plasma device, relevant diagnostics, as well as the methods used for the data analysis, will be presented.

3.1 CSDX linear plasma device

The Controlled Shear Decorrelation Experiment (CSDX) is a linear cylindrical plasma device at University of California, San Diego, and is shown in figure 3.1 in the following [1]. The cylindrical vacuum chamber is 2.8 m in length and 0.2 m in diameter, and is immersed in a uniform magnetic field generated by a series of solenoidal coils, which can be adjusted continuously from 0 to 1000 Gauss. The field lines terminate on insulated plates on both ends of the machine, which ensure that there is no current running through the end plates, and that the axial current fluctuations introduced by drift waves can only be balanced by cross-field ion polarization drift current given by the equation $\nabla_{\|} J_{\|} = -\nabla_{\perp} J_{\perp}$. The spatial variation of the magnetic field is negligible at the central sections of the device where all Langmiur probe data used in this dissertation were taken. The pressure in the vacuum chamber is maintained by a typical two-step vacuum pumping system with a mechanical pump as the first stage and a turbo pump on the second stage. There are several pressure gauges used to monitor the gas pressure before and during plasma discharges, including a convectron gauge, an ion gauge, and a baratron gauge. The baratron gauge provides a direct measure of the total kinetic pressure, and is functional during plasma discharges. Working gases (typically argon) are injected by mass flow controllers installed at the exit plane of the RF helicon source which is used to ionize the gas to produce plasmas. RF power at 13.56 MHz is coupled to the plasma by an azimuthally symmetric antenna. The RF power could be set to any value between 0 and 3 kW, with a feedback system to ensure the reflected power is less than 30 W. Figure 3.2 shows a picture of the CSDX plasma machine.

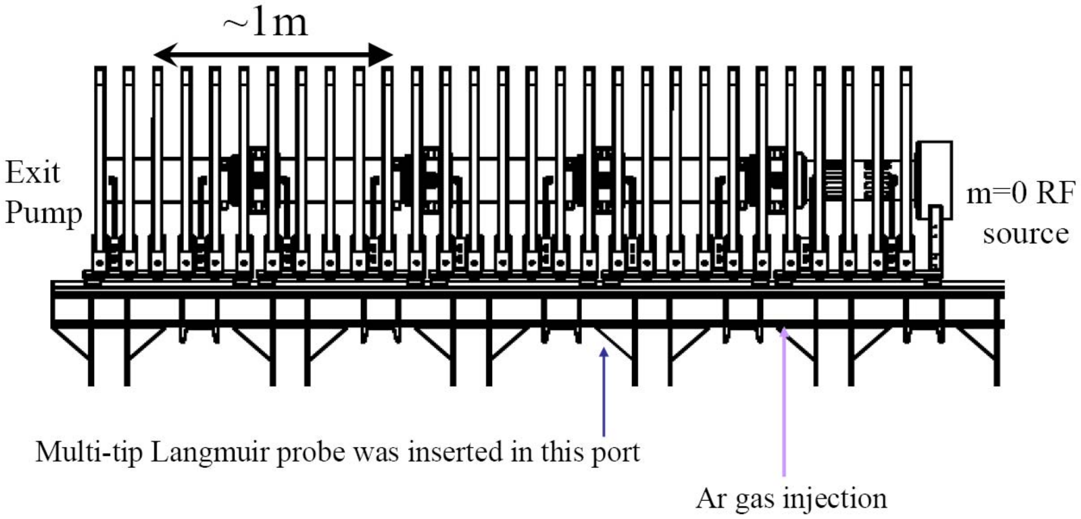

Figure 3.1 Schematic of the Controlled Shear Decorrlation Experiment linear plasma device [1].

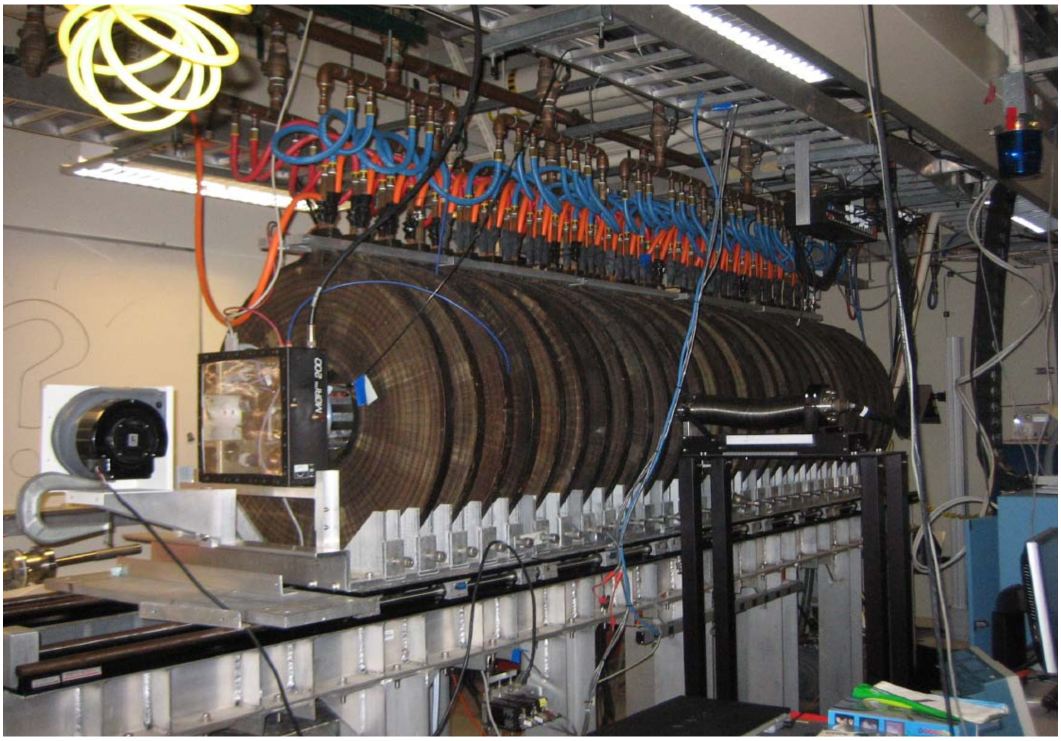

Figure 3.2 Picture of the Controlled Shear Decorrlation Experiment.

3.2 Diagnostics

Most of this thesis work is based on three diagnostics: two different multi-tip electric Langmiur probe arrays for both plasma density and potential measurements, and a fast imaging system for the two-dimensional turbulent density and velocity fluctuations measurements. These diagnostics are very powerful tools to study the drift wave-zonal flow turbulence in CSDX.

3.2.1 The dual 3x3 Langmiur probe array

For a laboratory plasma device, a Langmiur probe is probably the best and widely used diagnostic, simply due to the fact that it is relatively easy to construct; and that it can offer excellent spatial resolution as well as time resolution which most other diagnostics can not offer. In order to measure the nonlinear internal and kinetic energy transfer rates, which will be discussed in the next chapter, a dual 3x3 probe array was designed, built and installed on the machine, which is shown in figure 3.3 [2]

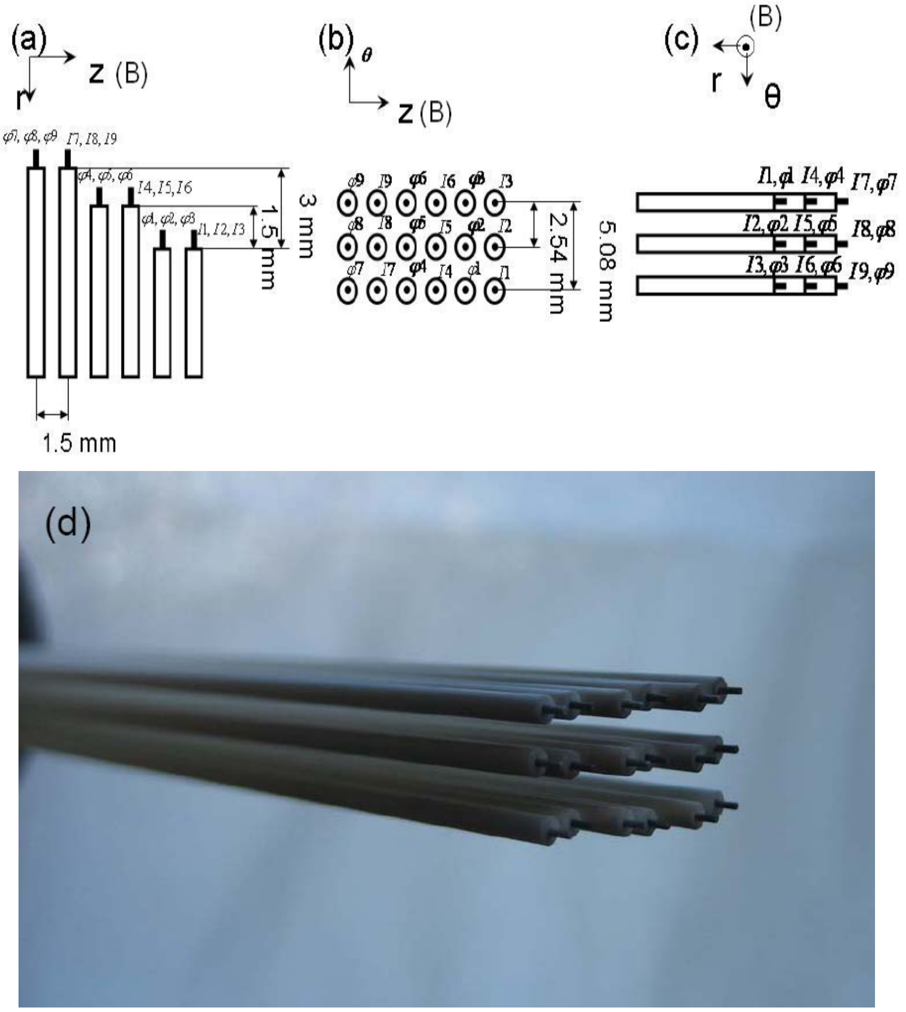
(a)
z (B)
r
φ7, φ8, φ9
I7, I8, I9
φ4, φ5, φ6
I4, I5, I6
φ1, φ2, φ3
I1, I2, I3
1.5 mm
3 mm
1.5 mm
(b)
θ
z (B)
φ9 I9 φ6 I6 φ3 I3
φ8 I8 φ5 I5 φ2 I2
φ7 I7 φ4 I4 φ1 I1
2.54 mm
5.08 mm
(c)
(B)
r
θ
I1, φ1 I4, φ4 I7, φ7
I2, φ2 I5, φ5 I8, φ8
I3, φ3 I6, φ6 I9, φ9
(d)

Figure 3.3 Dual 3x3 Langmiur probe array, of which one 3x3 array (9 channels) is for floating potential and anther 3x3 array is for ion saturation current (or density). These two arrays shift in the axial direction by 1.5 mm [2].

This dual 3x3 array has a total of 18 probe tips arranged in two 3x3 arrays. One 3x3 array gives floating potential $\phi(x, y, t)$ and the other gives density or ion saturation current $n(x, y, t)$. These two arrays are shifted by 1.5 mm in the axial direction (along the B field), and the introduced phase shift due to this 1.5 mm distance is negligible because of the typical long correlation length (meters) in the axial direction. In the azimuthal and radial directions these two arrays are overlapped with each other, hence there will be no phase shift in these two directions. This property is very important because many inferred quantities such as particle flux and internal energy transfer can be affected by the phase shift. During experiments all Isat channels were biased to -25V with respect to the vacuum chamber to make sure thermal electrons ($T_e \sim 3eV$) approaching the Isat probe tips will be rejected by the negative potential. Although generally a more negative bias voltage will guarantee that all electrons are rejected, it is not preferable because of two reasons: 1) the thickness of the plasma sheath, which determines the effective ion current collection area, will expand more at higher bias voltage. Too high a bias will artificially increase the collective surface area hence artificially increase the inferred density. 2) when the bias voltage is too high, ions will bombard the probe tip at very high kinetic energy, and will sputter the probe tip material. The sputtered material such as tungsten will be coated on ceramic tubes, finally making the ceramic tubes conductive. For CSDX, at the typical operation regime (RF power 1.5 kW, B=1000 Gauss, working gas pressure 3.0 mtorr) the on-axis electron temperature is roughly 3 eV [1], and a -25V bias voltage is good choice based on experience.

For potential channels it is preferable to place the high impedance resistors (~100 kOhm) as close as possible to the probe tips, especially when the plasma density is low and probe tip is small.

If the resistor is placed after the coaxial cable (shown by figure 3.4), the probe tip sheath impedance and the cable capacitance will comprise a low pass filter, thus filtering away all high frequency components in the floating potential signal and distort the phase information for low frequency components. For the dual 3x3 probe array, each probe tip is 1.0mm long and 0.33mm in diameter, which gives a very high plasma sheath impedance $R_{plasma} = \frac{k_B T_e}{e I_{isat}} \sim 10 - 20kOhm$ at a density of $\sim 10^{12} cm^{-3}$ at the plasma edge. Typically the cables connecting probe arrays to amplifiers are about 5 m long and with a total capacitance of ~500pF. Then a rough estimation of the bandwidth is given by $f_c = \frac{1}{2\pi[R_{plasma} \,||\, (R_{float} + R_{in})]C_{cable}} \simeq \frac{1}{2\pi R_{plasma} C_{cable}} \sim 15 - 30kHz$. This is not sufficient for measuring turbulent fluctuations with frequencies in the range ~ 10kHz.

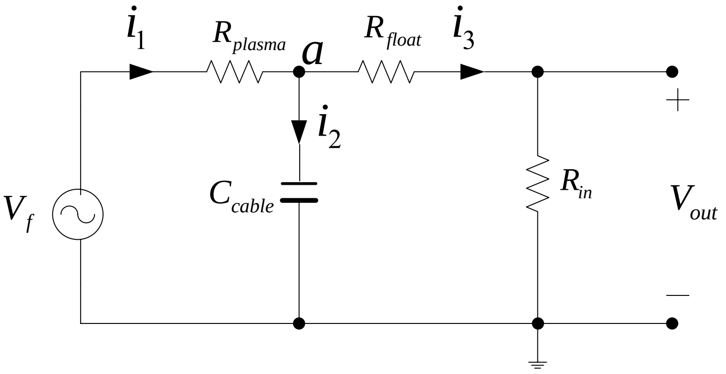

Figure 3.4 Thevinen equivalence for floating potential channels with resistor placed after the cable.

Putting the high impedance resistor close to the probe tip will effectively isolate the cable capacitance and largely increase the bandwidth of the effective transmission line. In this case, the low-pass filter is comprised of C_{cable} and R_{in} as shown in figure 3.5. The corresponding estimated bandwidth is given by $f_c \simeq \frac{1}{2\pi R_{in} C_{cable}} \sim 6.5MHz$ (the input impedance of amplifier is $R_{in} \sim 50Ohm$ typically), much higher than the former case when the resistor is after placed after the coaxial cable.

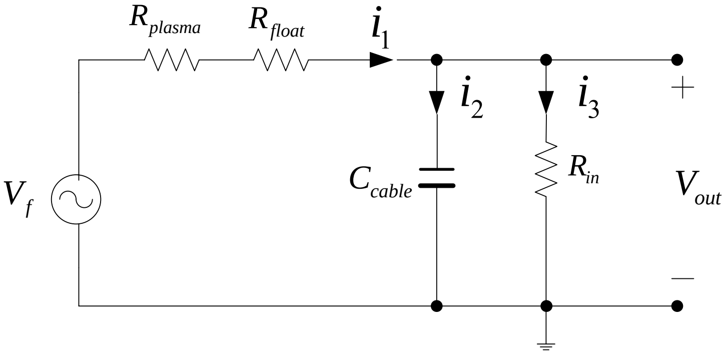

Figure 3.5 Thevinen equivalence for floating potential channels with resistor placed before the cable.

Floating potential is not exactly equal to plasma potential, and for plane probe approximation they are related by $\phi_{plasma} = \phi_{float} + \frac{k_B T_e}{e} \ln[\frac{1}{\alpha_0} (\frac{M_i}{2\pi m_e})^{1/2}]$, where ϕ_{plasma} is the plasma potential, ϕ_{float} is the floating potential, T_e is the electron temperature, M_i is the ion mass and m_e is the electron mass [3]. The plane approximation is valid here since the sheath thickness is much smaller than the tip radius. Depending on different working gases, the coefficient $\chi \equiv \ln[\frac{1}{\alpha_0} (\frac{M_i}{2\pi m_e})^{1/2}]$ is different, where $\alpha_0 \sim 0.5$ is the ratio of the ion density at the probe sheath edge to the local equilibrium plasma density outside the sheath region, and its exact value depends on the conditions in the presheath. Typically $\chi \approx 5.18$ for argon plasmas and $\chi \approx 3.33$ for hydrogen plasmas. For detailed theory about Langmiur probes, please refer to [3, 4]. Since we need plasma potential instead of floating potential to calculate the electric field inside plasmas, we should really measure the plasma potential using such as an emissive probe. But for the dense plasmas of these experiments, it is difficult to get an emissive probe sufficiently hot so that the outgoing thermionically emitted electron flux balances the incoming plasma electron flux and thus obtain an accurate plasma potential measurement. Fortunately a recent study showed that there is not much difference between the floating potential fluctuations and the plasma potential fluctuations [5], which means that we can compute the electric field fluctuations inside plasmas using floating potential.

The CSDX data acquisition system is comprised of secondary amplifiers, a multi-channel digitizer, and relevant electric circuits. All analogue signals from the Langmiur probe array are first amplified and then converted into digital signals by the digitizer, and finally saved into a computer for later analysis. A 16-bit 96-channel digitizer with an input impedance 20 kOhm and a sampling frequency 500 kHz, which gives a Nyquist frequency 250 kHz (well above the drift wave frequency ~ 10 kHz), was used to record the data. In order to get sufficient bandwidth, it is generally required to use low input impedance amplifiers for floating potential channels. Otherwise the low-pass filter comprised of the input impedance and the cable capacitance will filter away high frequency components of the signals. On CSDX a 16-channel amplifier with a gain of 28 and an input impedance of $50\ \Omega$ is used for floating potential measurements. For Isat channels a 16-channel AC coupled amplifier based on current transformer can directly convert the ion saturation current into a voltage signal with an output impedance of $50\ \Omega$ and a bandwidth of more than 1 MHz. For equilibrium and fluctuation density measurement, a DC coupled differential amplifier is used to measure the voltage across a shunt resistor, which can be used to infer the Isat running through the resistor.

3.2.2 The 4-tip turbulent flux Langmiur probe array

A fast scanning 4-tip Reynolds stress probe array, as shown in figure 3.6, was used to measure Isat and floating potentials.

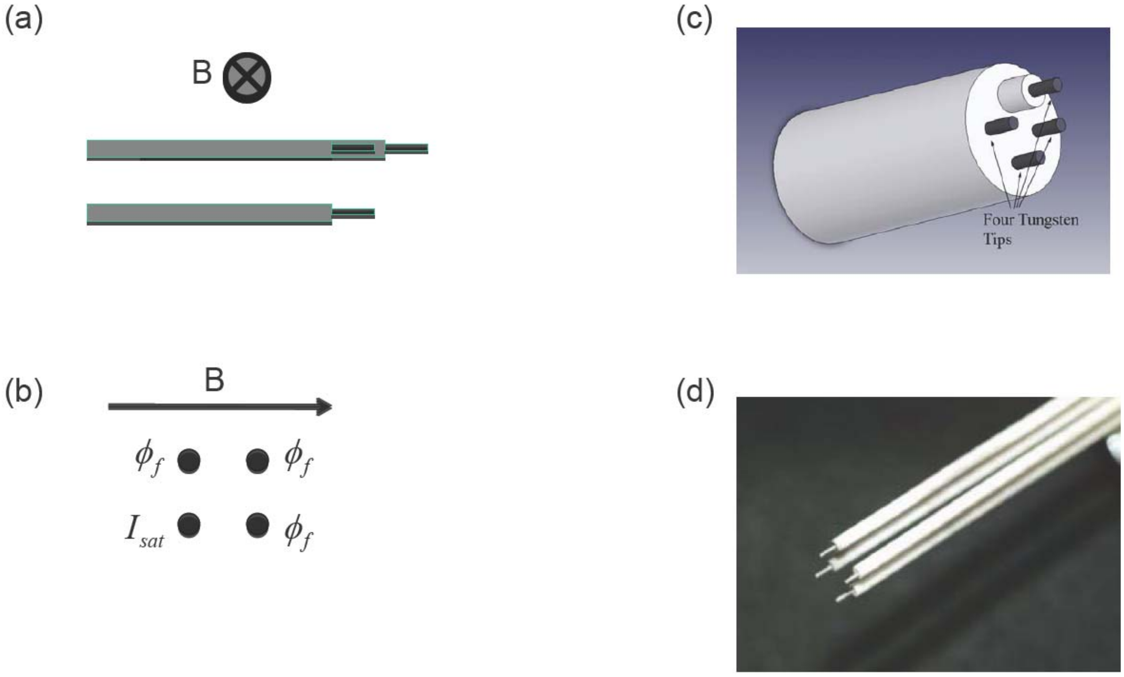

Figure 3.6 The 4-tip turbulent flux probe array. (a) and (b) shows the position relative to the magnetic field line. (c) is a 3D sketch and (d) is a picture of the Langmiur probe array. One of the 3 short tips is for ion saturation current, and the rest (two short tips and one long tip) are for floating potential, as indicated in (b).

This probe is mounted on a pneumatically activated probe drive that scans all radial positions within seconds. With this probe array layout, it can give an estimation of equilibrium density and Reynolds stress profiles, as well as density and potential fluctuations. This probe was separated by a distance of ~ 0.8 m in the axial direction with reference to the 18-tip probe array. Comparison and correlation studies between different probe arrays are then made possible.

3.2.3 Fast imaging diagnostic

Because turbulent eddy structures evolve very rapidly (with the eddy rotation time ~ 10 microseconds) and move around at a high speed ~ 10^5 cm/s, we need a diagnostic that can offer a high spatial resolution (at least can sample hundreds of points in space) at a very high time resolution (~100kHz sample rate), such that we can simultaneously monitor hundreds of points in space to construct the eddies' spatial-temporal dynamics. Langmiur probe arrays mentioned above can offer high temporally resolved signals but for the spatial resolution is inadequate to track the 2-dimensional turbulent evolution. Fast imaging is a very powerful tool that can offer 2-dimensional images with very high spatial resolution (millimeters) at very high time resolution (microseconds). Combining dynamics analysis from fast imaging and the statistical analysis from Langmiur probe measurements we can obtain in-depth pictures of the underlying physics.

The CSDX fast imaging system is composed of a fast camera and the relevant optics that couple the visible light emissions into the camera. A Phantom V. 7.1 fast camera was used, which has a 12-bit CMOS monochrome sensor array with a total of 800x600 pixels. The detailed features of this camera can be found elsewhere [6]. At a resolution of 128x64 pixels the framing rate of this camera can be as high as 100 kHz, which gives a spatial resolution 1-2 mm, when the plasma column cross-section is imaged on the sensor array. The minimum exposure time is 2 microseconds, and is sufficient for studying drift wave turbulence dynamics. The internal/external trigger function can be used to synchronize the camera and Langmiur probe measurements. Images are coupled to the fast camera using a large telescope (28 cm aperture). The optical setup is shown in figure 3.7, and gives an integrated view within +/- 0.7 deg along the magnetic field line. For detailed description of the optical setup please refer to [2].

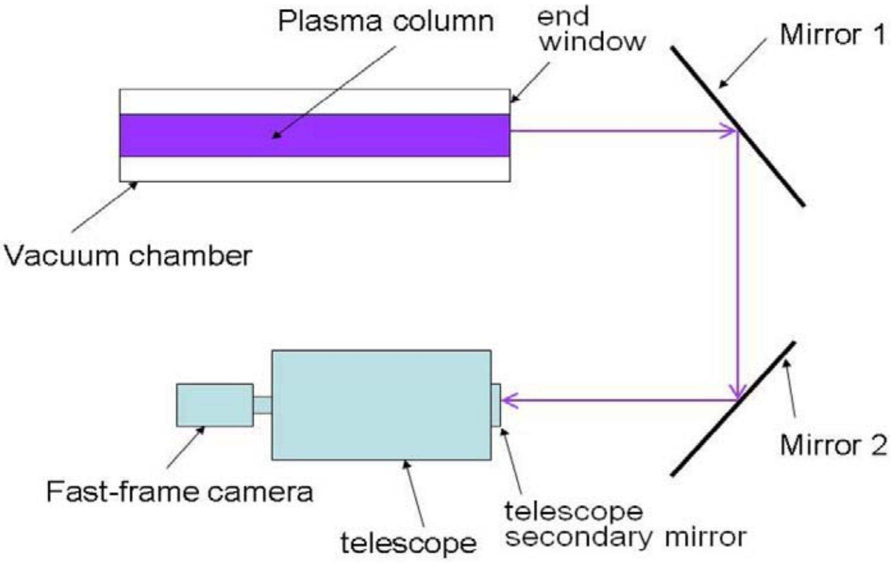
Plasma column
end window
Mirror 1
Vacuum chamber
Mirror 2
Fast-frame camera
telescope
telescope secondary mirror

Figure 3.7 The optical setup of the fast imaging system [2].

Since there is no interference filter used in the experiment, the collected light emissions by the camera were integrated over all wavelengths in the sensitive range of the CMOS sensors. However the collected light intensity fluctuations were shown to be closely correlated with density fluctuations in earlier experiments on CSDX [7]. Figure 3.8 (a) shows the raw ion saturation current fluctuations from Langmiur probe and light intensity fluctuations from fast imaging. Figure 3.8(b) shows a cross-correlation ~0.5 at zero phase delay. The cross-correlation is relatively high considering the contribution from small-scale fluctuations that were not resolved by the camera. The Langmiur probe and fast imaging signals also present very similar statistical properties which also validates the interpretation of light intensity fluctuations as density fluctuations. For more details about the relationship between the probe and the camera measurements please refer to [7].

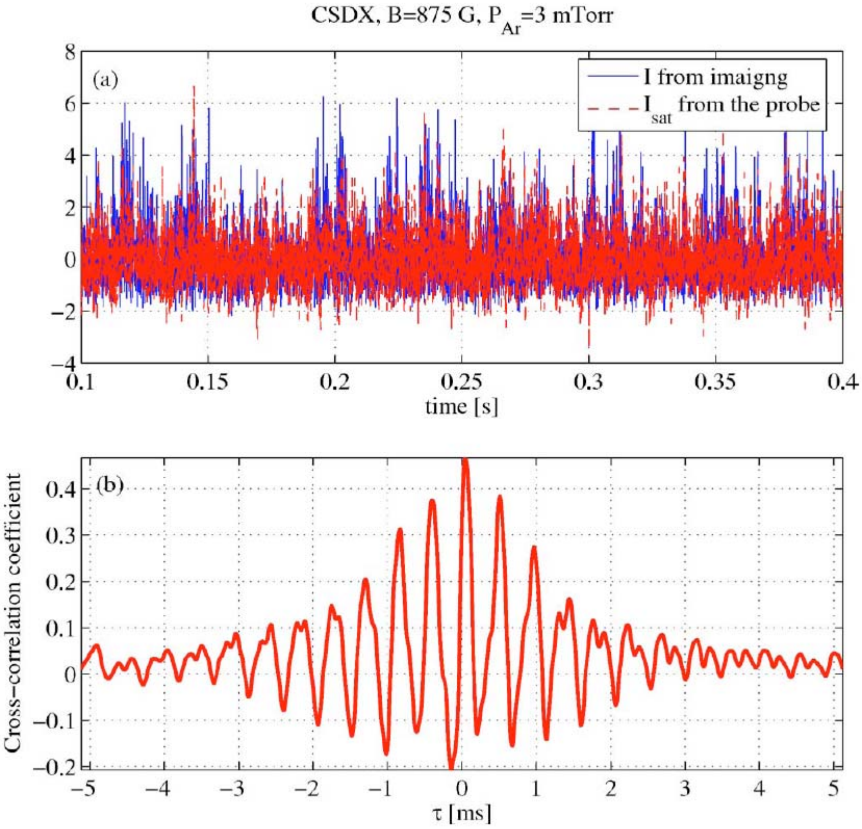

Figure 3.8 (a) Raw ion saturation current signal from Langmiur probe and light intensity fluctuation from fast imaging as a function of time. (b) Cross-correlation between Isat and light intensity fluctuations [7].

3.3 Methods for data analysis

3.3.1 General statistical analysis techniques

In order to get the statistical properties of turbulence, the autospectrum $S_{xx}(f)$, cross-spectrum $S_{xy}(f)$, cross-phase $\alpha_{xy}(f)$, and cross-correlation $C_{xy}(f)$ were all used in this dissertation. The definitions of the above quantities are shown in Eqns (3.1)-(3.4). Bispectral analysis is a key part of this dissertation and will be discussed later.

$$S_{xx}(f)=\left\langle X(f)X^{*}(f)\right\rangle \tag{3.1}$$

$$S_{xy}(f)=\left\langle X(f)Y^{*}(f)\right\rangle \tag{3.2}$$

$$\alpha_{xy}(f)=\arctan\left[\mathrm{Im}(S_{xx}(f))/\mathrm{Re}(S_{xx}(f))\right] \tag{3.3}$$

$$C_{xy}(\tau)=\int_{0}^{T}x(t)y(t-\tau)dt \tag{3.4}$$

In the above equations, $X(f)$ and $Y(f)$ are the Fourier transform of time series $x(t)$ and $y(t)$ respectively, $\langle\ldots\rangle$ denotes the ensemble average, and the star "*" indicates the complex conjugate, "Im" refers to the imaginary part, "Re" refers to the real part, and τ here is the time delay. Time series of density or potential fluctuations can be obtained from the probe or imaging data. Let us take potential $\phi(t)$ as an example. To estimate its autospectrum, as the first step we cut $\phi(t)$ into a set of windowed time series with desired length and denote the ith window as $\phi(t_i)$. We then Fourier transform $\phi(t_i)$ into frequency domain to get $\Phi(f_i)$, and multiply $\Phi(f_i)$ with its complex conjugate to get $\Phi(f_i)\Phi^{*}(f_i)$. Finally we take the ensemble average over all the windows to get the autospectrum $S_{\phi\phi}(f)=\frac{1}{N}\sum_{i=1}^{N}\Phi(f_i)\Phi^{*}(f_i)$, where N is the total number of windows. Other quantities in Eqns (3.2)-(3.4) can be obtained similarly.

In reality the length of data and sample rate are limited. In the Fourier domain the frequency resolution is then determined by the length of each window, and the maximum frequency is limited by the sample rate. The more windows we have, the more likely we will get a convergent spectrum. With finite data length, there is a trade-off between the number of windows and the length for each window, which means that if we want to get higher frequency resolution, we need to sacrifice the convergence. For example, suppose the total length of the time series $\phi(t)$ is T seconds and we use this T seconds of data as one window to do the Fourier transform. Then according to discrete Fourier transform [8] the frequency resolution is $\Delta f = 1/T$, but since we use only one window the obtained Fourier transformed series may be very noisy (i.e., its variance is big).. But if we first divide the T seconds of data into N windows then compute the Fourier transform, for each window the frequency resolution is $\Delta f = 1/NT$, a factor of N lower compared to before. But since the spectrum we get is an averaged value over N windows, the variance level will be a factor of $1/\sqrt{N}$ lower. Thus we can see that the windowed Fourier transform offers spectrum with a lower noise level at the cost of frequency resolution. More details about discrete Fourier transform can be found in [8].

In cases when the data length is very limited like fast scan Langmiur probe data from tokamaks, overlapped or sliding windows are sometimes used to increase the frequency resolution. There are times when spectrum time evolution is needed, sliding window can effectively increase the time resolution, but special attention is needed when interpreting the time and frequency resolutions of the obtained sequence. Finally note that Hanning windows or Hamming windows [9] are often used in order to deal with frequency leakage due to finite window length.

3.3.2 Bispectral analysis and its interpretation

The auto-bispectrum was used in fluid mechanics [10] and introduced by Kim and Powers [11] into plasma signal analysis for studying the quadratic nonlinearity of wave-wave interactions. It is essentially a measure of the phase coherence among different waves. The auto-bispectrum is normally defined as [8]:

$$S_{xxx}(f_1, f_2) \equiv \left\langle X(f)X^*(f_1)X^*(f_2)\right\rangle = \frac{1}{M}\sum_{k=1}^{M}\left[X(f)X^*(f_1)X^*(f_2)\right]_k \tag{3.5}$$

where k indicates the kth realization (or window), and M is the total number of realizations. In the above definition, the summation is the process of phase mixing (or phase canceling). In order to see this more clearly, the auto-bispectrum definition can be rewritten as:

$$\begin{aligned} S_{xxx}(f_1, f_2) &\equiv \frac{1}{M}\sum_{k=1}^{M}\left[X(f)X^*(f_1)X^*(f_2)\right]_k \\ &= \frac{1}{M}\sum_{k=1}^{M}\left[\left|X(f)\right|e^{i\theta(f)}\left|X^*(f_1)\right|e^{-i\theta(f_1)}\left|X^*(f_2)\right|e^{-i\theta(f_2)}\right]_k \\ &= \frac{1}{M}\sum_{k=1}^{M}\left[\left|X(f)\right|\left|X^*(f_1)\right|\left|X^*(f_2)\right|e^{i\delta\theta}\right]_k \end{aligned} \tag{3.6}$$

where $\delta\theta = \theta(f) - \theta(f_1) - \theta(f_2)$. If $\delta\theta$ is a zero-mean symmetrically distributed random variable nothing will survive the phase mixing process, leading a zero auto-bispectrum; if $\delta\theta$ is distributed around one specific value $\left\langle\delta\theta\right\rangle$ throughout all realizations, the auto-bispectrum will equal to $S_{xxx}(f_1, f_2) \approx \frac{1}{M}e^{i\langle\delta\theta\rangle}\sum_{k=1}^{M}\left[\left|X(f)\right|\left|X^*(f_1)\right|\left|X^*(f_2)\right|\right]_k$. So $\left\langle\delta\theta\right\rangle$ determines how much can survive the phase mixing, thus determines the value of auto-bispectrum $S_{xxx}(f_1, f_2)$.

A 3-wave interaction, i.e. two waves beating together to generate the 3rd wave, will result in a phase coherence among $\theta(f)$, $\theta(f_1)$ and $\theta(f_2)$. This means that $\delta\theta$ for all windows is not randomly distributed over $(-\pi,\pi)$ and thus the ensemble averaging gives a non-zero auto-bispectrum. Linear couplings do not survive the averaging since they will lead to a random $\delta\theta$ (due to the random phase of the driving wave).

The normalized auto-bispectrum, i.e. auto-bicoherence, is typically defined as [8]:

$$b_{xxx}^2(f_1, f_2) \equiv \frac{\left|\left\langle X(f)X^*(f_1)X^*(f_2)\right\rangle\right|^2}{\left\langle\left|X(f)\right|^2\right\rangle\left\langle\left|X(f_1)X(f_2)\right|^2\right\rangle} \tag{3.7}$$

Bicoherece is often interpreted as the ratio of the nonlinearly coupled energy to the total energy [11]. Note that bicoherece can only indicate the intensity of the quadratic coupling and can not tell the direction of energy flow. Therefore an auto-bicoherence analysis cannot tell which waves are sources and which waves are generated via nonlinear couplings.

To more clearly see the physics arguments and the symmetry properties of auto-bispectrum and auto-bicoherence, a test signal is generated to simulate the data from experiments:

$$\begin{aligned} x^{(k)}(t) = {} & \cos\left(f_b t+\theta_b^{(k)}\right)+\cos\left(f_c t+\theta_c^{(k)}\right)+\frac{1}{2}\cos\left(f_d t+\theta_d^{(k)}\right) \\ & +\cos\left(f_b t+\theta_b^{(k)}\right)\cos\left(f_c t+\theta_c^{(k)}\right) \\ & + noise^{(k)}(t) \end{aligned} \tag{3.8}$$

where $\frac{f_b}{f_N}=0.220$, $\frac{f_c}{f_N}=0.375$, $f_d = f_b + f_c$, and $\theta_b^{(k)}$, $\theta_c^{(k)}$ and $\theta_d^{(k)}$ are uniformly distributed independent random phases for the kth realization, and $noise^{(k)}(t)$ is the applied

Gaussian distribution noise (-5dB). From the analytical form of $x^{(k)}(t)$ it should be expected that:

(1) Half of the energy at frequency f_d is coupled from f_b and f_c, therefore the auto-bicoherence for the coupling among f_d, f_b and f_c should be 0.5;

(2) All of the energy at frequency $f_c - f_b$ is coupled from f_b and f_c, therefore the auto-bicoherence for the coupling among $f_c - f_b$, f_b and f_c should be 1.0

Figure 3.9 gives autopower, auto-bispectrum, and auto-bicoherence calculated from this test signal. It can be seen from figure 3.9 (b) that the auto-bicoherence is consistent with both of the above statements. Note that in figure 3.9 (d) the 6 different bright spots indicated stand for the same physics process for auto-bicoherence, which will be explained in detail in the next chapter.

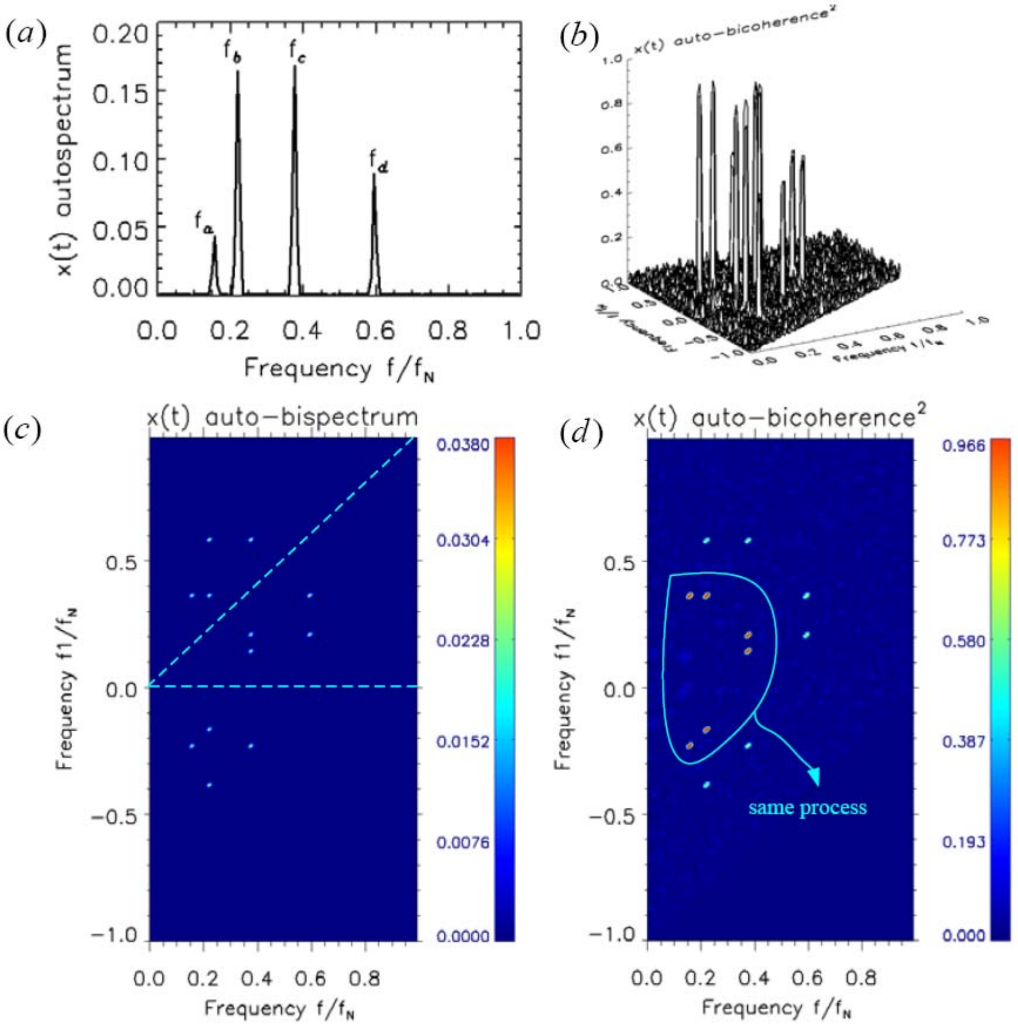

Figure 3.9 (a) auto-spectrum of the test signal x(t). (b) 3D view of the auto-bicoherence. (c) auto-bispectrum, and (d) auto-bicoherence.

The auto-bispectrum and auto-bicoherence can be easily generalized to measure the phase coherence among three different fields [8, 12]:

$$S_{xyz}(f_1, f_2) \equiv \left\langle X(f)Y^*(f_1)Z^*(f_2) \right\rangle = \frac{1}{M}\sum_{k=1}^{M}\left[X(f)Y^*(f_1)Z^*(f_2) \right]_k \qquad (3.9)$$

$$b_{xyz}^2(f_1, f_2) \equiv \frac{\left|\left\langle X(f) Y^*(f_1) Z^*(f_2) \right\rangle\right|^2}{\left\langle \left|X(f)\right|^2 \right\rangle \left\langle \left|Y(f_1) Z(f_2)\right|^2 \right\rangle} \tag{3.10}$$

The cross-bicoherence can still be interpreted as the ratio of coupled energy to the total energy at destination frequency. Similar to the auto-bicoherence, the general cross-bicoherence by itself cannot show the direction of energy flow.

3.3.3 Other techniques used

One way to estimate the time average turbulent velocity is by time delay estimating (TDE) [13]. The underlying principle is straightforward. Suppose that there are two probe tips separated with a distance of $\triangle x$. When a turbulent structure passes one probe tip at time t and passes another one at some later time $t+\tau$, then the turbulent velocity can be estimated as $u = \triangle x / \tau$. The key assumption that the two-point technique based on is the unidirectional feature of flows in the direction of the tip separation, i.e. the direction of the flow velocity, which is the azimuthal direction, is the same as the tip separation direction. Otherwise the interpretation is problematic. In CSDX this assumption is satisfied since the average azimuthal flow is mainly in the electron diamagnetic direction. The time delay τ can be estimated from the peak of the cross-correlation between two tips. Figure 3.10 shows plasma azimuthal velocity estimated by two-point correlation TDE technique from both probe and fast imaging, which is consistent with ion fluid velocity measured by Mach probe, showing that two-point TDE can produce a good approximation. For details and evaluation of this time delay estimation (TDE) technique, please refer to [13].

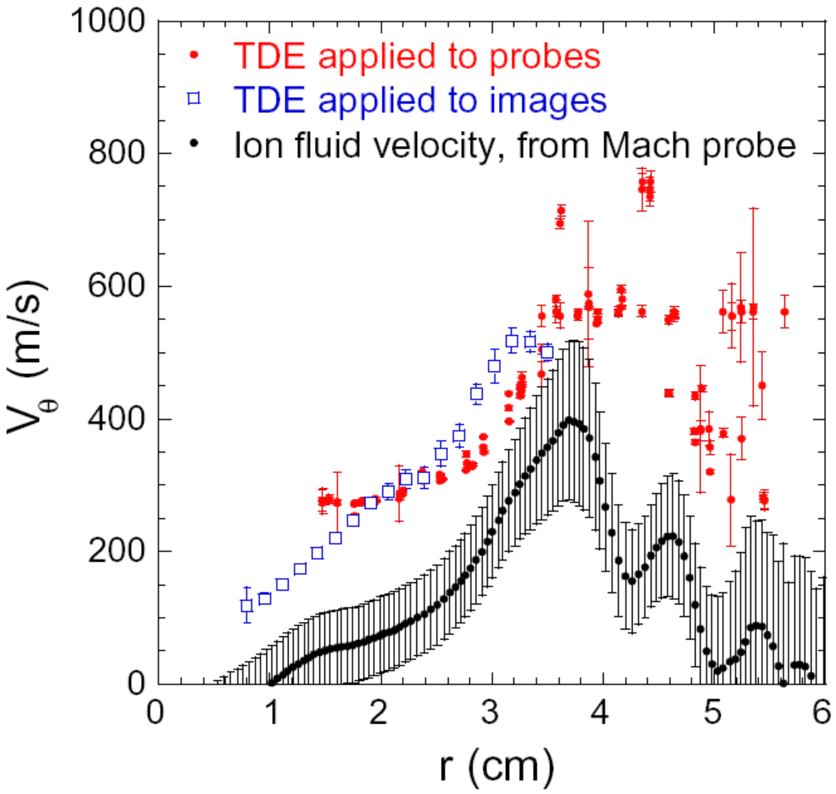

Figure 3.10 The azimuthal velocity measured by two-point correlation TDE from probe and imaging data compared against ion fluid velocity measured by Mach probe [14].

An alternative way to estimate the time average turbulent velocity is by two-point technique, which was first applied by Beall et al.[13]. Since the time delay is essentially a phase delay, alternatively we can first calculate the cross-phase between two channels $\alpha_{xy}(f)$ as is shown in Eqn. (3.3), then the effective wavenumber can be estimated by $k(f)=\alpha_{xy}(f)/\triangle x$, and finally the velocity can be obtained via $u(f)=f/k(f)$. Note that the velocity here is frequency resolved. To have a time average azimuthal velocity, we can average it over all frequencies with cross-power as the weight. Thus this technique is essentially the same as TDE. Both TDE and two-point technique can also be applied to imaging data to extract velocities, which can be used to compare against velocities estimated from Langmiur probe data.

The Reynolds stress, which is the turbulent momentum flux, is estimated via $RS = \langle \tilde{u}_r \tilde{u}_\theta \rangle$, where $\tilde{u}_r$ and $\tilde{u}_\theta$ can be approximated by $\vec{E} \times \vec{B}$ drift velocities, i.e., $\tilde{u}_r = \tilde{E}_\theta / B_0$ and $\tilde{u}_\theta = -\tilde{E}_r / B_0$, and $\langle ... \rangle$ here denotes the ensemble average. As mentioned before, the floating potential can be used to calculate the fluctuating electric field $\tilde{E}_r = -\nabla_r \tilde{\phi}_f$ and $\tilde{E}_\theta = -\nabla_\theta \tilde{\phi}_f$ by assuming that temperature fluctuation is negligible.

CSDX discharge conditions are highly stable and repeatable, which means that the plasma turbulence is stationary. This is very important because we need long sequences of data to get statistically converged values when estimating plasma parameters such as autospectra, Reynolds stress, and plasma velocities, etc. from turbulent fluctuations. The current CSDX 96-channel data acquisition system can store up to 8 seconds of data at a sample rate of 500 kHz for one shot. Because CSDX plasma is stable and all shots taken under the same discharge conditions (magnetic field, gas pressure, etc.) are with the same statistical properties, we can take as many shots as needed to compute the statistics to the desired convergence. Typically for each channel about 10 seconds (~ 5 million sample points) of probe data were taken, and they were divided into more than 1000 realizations to compute ensemble averages. Therefore the corresponding statistical uncertainties of the estimated parameters are very small and typically are within the thickness of the produced curves. Bispectra converge more slowly compared to quantities like autopower, particle fluxes, etc., but 1000 realizations are enough to get good convergence as will be shown in the next chapter.

All the contents of the next chapter, including text and data, has been published as it appears in “Study of nonlinear spectral energy transfer in frequency domain”, M. Xu, G. R. Tynan, C. Holland, Z. Yan, S. H. Muller, J. H. Yu, Phys. Plasmas **16** 042312 (2009). The dissertation author is the primary investigator and author of this article.

References:

[1] M. J. Burin, G. R. Tynan, G. Y. Antar, N. A. Crocker, and C. Holland, Phys. Plasmas **12**, 052320 (2005)

[2] Z. Yan, Ph.D. thesis, Turbulence-driven shear flow and self-regulating drift wave in a cylindrical plasma device (2008)

[3] F. F. Chen, Lecture Notes on Langmuir Probe Diagnostics, IEEE-ICOPS meeting, Jeju, Korean, June 2005.

[4] F. F. Chen, Phys. Plasmas 8, 3029 (2001)

[5] N. Mahdizadeh, F. Greiner, M. Ramisch, U. Stroth, W. Guttenfelder, C. Lechte and K. Rahbarnia, Plasma Phys Contr F **47** (4), 569-579 (2005).

[6] http://www.visionresearch.com.

[7] G. Y. Antar, J. H. Yu, and G. R. Tynan, Phys. Plasmas, 14, 022301 (2007)

[8] Powers, E.J., Hong, J.Y, and Ritz, Ch.P, “Applied Digital Time Series Analysis (Preliminary Version),” copyright 1986 by E. J. Powers

[9] Eric W. Weisstein (2003). CRC Concise Encyclopedia of Mathematics. CRC Press.

[10] K. Hasselman, W. Munk, and C. MacDonald, “Bispectra of Ocean Waves“, Time Series Analysis, M. Rosenblatt, Ed., New York: Wiley, 1963, pp. 125-130.

[11] Y. C. Kim and E. J. Powers, IEEE Trans. Plasma Sci. **PS-7** No. 2 120-131 (1979)

[12] B. Ph. Van Milligen, T. Kalhoff, M. A. Pedrosa, and C. Hidalgo, Nucl. Fusion 48, 115003 (2008).

[13] J. M. Beall, Y. C. Kim, and E. J. Powers, J. Appl. Phys. 53, 3933 (1982)

[14] J. H. Yu, C. Holland, G. R. Tynan, G. Antar and Z. Yan, J Nucl Mater **363**, 728-732 (2007)

Chapter 4

Study of nonlinear spectral energy transfer in frequency domain

4.1 Introduction

The study of nonlinear dynamics of drift wave turbulence, and specifically the study of how large spatial scale fluctuations and zonal flows are generated by nonlinear processes and of how the resulting shear flows affect the turbulent density fluctuation scale lengths directly addresses the underlying physics for zonal/shear flow generation [1, 2], gyro-Bohm/Bohm scaling [3] and the origins of critical gradient transport scaling in magnetically confined plasmas [4], as well as provides tests of fundamental turbulence theory. As a result, the nonlinear spectral energy transfer mediated via wave-wave coupling has received significant attention, as given in Ref. [1, 5-10]. The bispectrum, which is related to the degree of phase correlation among three waves, was introduced to the plasma physics community by Kim and Powers [11] to study the quadratic nonlinearity of plasma fluctuations, and was motivated by earlier applications of this technique to neutral fluid turbulence, see, for example, Ref. [12-14]. By assuming the detailed form of three-wave coupling and deriving a power balance equation, Kim went further and developed a way to experimentally determine the coupled energy flow among different spectral components [10]. In that work, the wave coupling coefficient had to be known a priori in order to know this power transfer due to the three-wave coupling.

Using a single field model suitable for turbulence with very small parallel electron dissipation, Ritz et al [15] then developed and subsequently Kim et al [16] refined a method which enables one to quantitatively estimate the growth rate γ_k, dispersion relation $\bar{\omega}_k$ and the wave-wave coupling coefficient $\Lambda_k^Q(k_1, k_2)$, from which the power transferred through nonlinear coupling can be calculated from experimental data. In order to obtain two coupled equations that yield the growth rate, dispersion relation and coupling coefficient, the fourth-order spectral moment that occurs in their work was approximated by the square of the second-order moment using the Millionshchikov approximation [17]. This method was derived in the wavenumber domain and in principle requires a knowledge of the temporal behavior of the Fourier transformed potential $\phi(k,t)$ (which is obtained from simultaneous multipoint turbulence measurements) to perform the calculation. As a result, a simultaneous measurement at a large number of spatially localized points is typically required, which is challenging due to practical (i.e. large number of channels) and physical (i.e. measuring turbulence properties without much disturbance) limitations. These works then used the Taylor frozen flow hypothesis to relate wavenumber to frequency, and then argued that the energy transfer could then be studied in the frequency domain, thereby avoiding the requirement for a large number of spatial measurements.

Another concern in applying these techniques arises from the multi-field nature of plasma turbulence. Turbulence in magnetic fusion plasmas is characterized by fluctuations in density, potential, temperature, and magnetic field and these fluctuations can influence the turbulence dynamics and resulting transport. All the methods mentioned above assume that the observation of one field is sufficient to describe the nonlinearity in the plasma, and the effects introduced by cross-field interaction are small. For example, turbulence in magnetic fusion confinement devices clearly exhibits multi-field dynamics as shown e.g. by the fact that the normalized amplitudes of density and potential fluctuations are not equal [18], in clear violation of the underlying assumptions of all single-field drift turbulence models. Furthermore in the edge plasma region where these techniques are usually applied there is a large phase shift between the density and potential fluctuations [18], again invalidating the fundamental model on which these single-field energy transfer models are based. In low temperature plasmas found e.g. in the CSDX device [19] used in this work, the measured density and potential fields have a cross-correlation significantly less than unity as shown by figure 4.3(d), and have a non-zero density-potential cross-phase, again in clear violation of the assumptions of single field models. Similar observations hold for the turbulence in the edge and scrape-off layer region of confinement experiments. As a result, studies of turbulence nonlinear dynamics that are to be compared against such experiments should include at least two fields (e.g. at least density and velocity or electrostatic potential as well as temperature fluctuations if those are important for the turbulence dynamics) and cannot rely upon models that are based upon the single field model of drift turbulence.

Nonlinear energy transfer in simple models of drift-wave turbulence has been extensively studied by many groups using both analytic and computational approaches (see, for instance, the work by Camargo et al [20] for a comprehensive numerical investigation of the issue). Recently Manz et al [21] analyzed experimental measurements in wavenumber space using a single-field model applied separately to density and potential measurements and showed that turbulent density fluctuation energy was transferred to small scales, while turbulent kinetic energy was transferred to large scales. The first use of a multi-field approach to study nonlinear turbulence dynamics via direct calculation of cross-bispectra was performed by Holland et al [22] using beam emission spectroscopy data. The results showed that radially sheared, oscillating poloidal velocity of a geodesic acoustic mode caused the density fluctuation energy to move towards higher frequency. A brief discussion of multi-field nonlinear energy transfer in drift turbulence was also included in a recent review paper [23].

In this chapter, we develop a technique to study the nonlinear transfer of turbulence energy in the frequency domain in a system that is described by two fluctuating fields (density and potential). By combining the derived energy balance equations with a cross-bispectral analysis of the nonlinear terms, the nonlinear energy transfer due to the wave-wave interactions of the drift fluctuations can be determined. Although it is not discussed here, the technique can also be extended in a straightforward manner to turbulence involving temperature fluctuations.

The rest of this chapter is arranged as follows: Section 4.2 presents the theoretical derivation and interpretation of nonlinear energy transfer coefficients and their realization in experiments. Section 4.3 gives a brief description about the experimental setup. Section 4.4 is a sample of experimental results of nonlinear energy transfer. Section 4.5 includes a summary of the contents and some discussions.

4.2 Theoretical derivation and interpretation of nonlinear energy transfer terms

Although a similar derivation of spectral energy transfer terms was reported, as given in Ref. [20], and in particular the derivation and study of internal energy transfer in frequency space has been published in Ref. [22], a brief derivation for both internal and kinetic energy transfer terms in frequency domain is included here to help to understand the experimental results from both technical and physical perspective of views. The three-wave coupling enters when a Fourier transform is performed on either the continuity or momentum equation, with the convective derivative $\underline{u}\cdot\nabla n$ or $\underline{u}\cdot\nabla\underline{u}$, where $\underline{u}$ is the fluid velocity that is approximated by $\underline{u}\approx-\frac{\nabla_\perp\phi\times\underline{B}}{B^2}$ in the following derivation. From the electron momentum and electron continuity equations, an energy transport equation for the spectra of density fluctuations is derived in the frequency domain.

The electron continuity equation:

$$\frac{\partial n_e}{\partial t}+\nabla_\perp\cdot(n_e\underline{u}_{e\perp})+\frac{\partial}{\partial z}(n_e u_{e\parallel})=0 \tag{4.1}$$

in which the electron velocity perpendicular to magnetic field is dominated by $\underline{E}\times\underline{B}$ and diamagnetic drifts, can be written as (with the unit vector in the magnetic field direction denoted by $\hat{z}$ and the quasi-neutral assumption $n_e\approx n_i=n$ applied):

$$(\frac{\partial}{\partial t}+\underline{u}_\perp\cdot\nabla_\perp)n=-\frac{\partial}{\partial z}(nu_\parallel) \tag{4.2}$$

where $\underline{u}_\perp=\frac{\hat{z}\times\nabla_\perp\phi}{B}$ is the $\underline{E}\times\underline{B}$ velocity. The plasma density fluctuations can be represented in the frequency domain by $n(\underline{x},t)=\sum_\omega n_\omega(\underline{x},t)e^{i\omega t}$ where we have allowed the coefficients to possibly vary in time (we discuss this point at length below). A similar expression can be used to decompose the velocity into the frequency domain. Therefore we can then write the time derivative in equation (4.2) as:

$$
\begin{aligned}
\frac{\partial n(\underline{x},t)}{\partial t} &= \frac{\partial}{\partial t}\sum_{\omega} n_{\omega}(\underline{x},t)e^{i\omega t} \\
&= \sum_{\omega}[e^{i\omega t}\frac{\partial n_{\omega}(\underline{x},t)}{\partial t} + i\omega e^{i\omega t} n_{\omega}(\underline{x},t)] \\
&= \sum_{\omega}[(\frac{\partial}{\partial t} + i\omega)n_{\omega}(\underline{x},t)]e^{i\omega t}
\end{aligned}
\tag{4.3}
$$

As we discuss below, there are limitations on the rate of change of the frequency components which must be tested empirically from experimental data. Next, we Fourier transform equation (4.3) into the frequency domain, and denoting $n_{\omega}(\underline{x},t)$ as n_{ω} we then have:

$$
\frac{\partial}{\partial t}n_{\omega} + i\omega n_{\omega} + \sum_{\omega_1}(\underline{u}_{\perp\omega-\omega_1}\cdot\nabla_{\perp})n_{\omega_1} = -\frac{\partial}{\partial z}\mathrm{F}(nu_{\parallel}) \tag{4.4}
$$

Where F denotes the Fourier transform. Multiply both sides by the conjugate of n_{ω}, i.e. n_{ω}^{*}

$$
n_{\omega}^{*}\frac{\partial n_{\omega}}{\partial t} + i\omega|n_{\omega}|^2 + \sum_{\omega_1} n_{\omega}^{*}(\underline{u}_{\perp\omega-\omega_1}\cdot\nabla_{\perp})n_{\omega_1} = -n_{\omega}^{*}\frac{\partial}{\partial z}\mathrm{F}(nu_{\parallel}) \tag{4.5}
$$

Adding the above equation to its conjugate and ensemble averaging over a sufficient number of realizations, we can form an ensemble-averaged energy conservation equation in the frequency domain:

$$
\Rightarrow \left\langle \frac{1}{2}\frac{\partial|n_{\omega}|^2}{\partial t}\right\rangle = \left\langle -\mathrm{Re}[\sum_{\omega_1} n_{\omega}^{*}(\underline{u}_{\perp\omega-\omega_1}\cdot\nabla_{\perp})n_{\omega_1}]\right\rangle + \left\langle -\mathrm{Re}[n_{\omega}^{*}\frac{\partial}{\partial z}\mathrm{F}(nu_{\parallel})]\right\rangle \tag{4.6}
$$

The above equation (4.6) simply states that the rate of change of internal energy at the frequency ω is determined by quadratic coupling, linear growth or damping at ω, and parallel dissipation of parallel electron motion. The physical meaning of each term is given below:

$\left\langle \frac{1}{2}\frac{\partial|n_{\omega}|^2}{\partial t}\right\rangle$ is the rate of change of density fluctuation spectra n_{ω}^2 (denoted as the internal energy) at one specific spatial position;

$\left\langle -\mathrm{Re}[\sum_{\omega_1} n_\omega^* (\underline{u}_{\perp\omega-\omega_1}\cdot\nabla_\perp) n_{\omega_1}] \right\rangle$ is the nonlinear wave-wave coupling term that determines how much energy flows into or out of the Fourier component at the frequency of ω due to 3-wave coupling. This quadratic nonlinear term comes from the Fourier transform of the convective derivative, which is in the form of a convolution, and thus imposes a selection rule $\omega = \omega_1 + \omega_2$ on the nonlinear coupling. Since this nonlinear coupling term is related to density auto-spectrum, it is called the internal energy transfer term, denoted as T_n here.

Assuming an isothermal plasma, $u_{\|}$ can be obtained from the parallel component of the electron momentum equation. Substituting this result into equation (4.6), and using the normalizations $\hat{n}_e \equiv \frac{\tilde{n}_e}{n_{e0}}$, $\hat{\phi} \equiv \frac{e\phi}{k_B T_e}$, $\hat{t} \equiv \frac{t}{1/\Omega_{ci}}$, $\hat{\nabla}_\perp \equiv \rho_s \nabla_\perp$, $\frac{\partial}{\partial z} = \frac{1}{\lambda_{efree}}\frac{\partial}{\partial \hat{z}}$, and $\hat{L}_{nr} \equiv L_{nr}/\rho_s$, where $\rho_s \equiv \frac{c_s}{\Omega_{ci}} = \sqrt{\frac{k_B T_e}{M\Omega_{ci}^2}}$ is the effective ion Larmor radius calculated with electron temperature, $\lambda_{efree} = \frac{u_{the}}{\nu_{ei}} = (\frac{k_B T_e}{m_e})^{1/2} \frac{m_e}{n_e e^2 \eta}$ is the electron mean free path and $L_{nr} \equiv \frac{n_0(x)}{\nabla_r n_0}$ is the local density gradient scale length, and we drop the $\widehat{(\ )}$ notation, the internal energy equation becomes:

$$\begin{aligned}\left\langle \frac{1}{2}\frac{\partial |n_\omega|^2}{\partial t} \right\rangle &= \left\langle -\mathrm{Re}[\sum_{\omega_1} n_\omega^* (\hat{z}\times\nabla_\perp \phi_{\omega-\omega_1}\cdot\nabla_\perp) n_{\omega_1}] \right\rangle \\ &\quad - \left\langle \frac{1}{L_{nr}} \mathrm{Re}[n_\omega^* \nabla_\theta \phi_\omega] \right\rangle + \left\langle \frac{\nu_{ei}}{\Omega_{ci}} \mathrm{Re}[n_\omega^* \frac{\partial^2}{\partial z^2}(n_\omega - \phi_\omega)] \right\rangle \end{aligned} \tag{4.7}$$

Here we have invoked the quasi-neutrality assumption, and the term $-\left\langle \frac{1}{L_{nr}} \mathrm{Re}[n_\omega^* \nabla_\theta \phi_\omega] \right\rangle$ indicates that energy can be extracted from the mean density gradient and hence is the linear driving term, and $\left\langle \frac{\nu_{ei}}{\Omega_{ci}} \mathrm{Re}[n_\omega^* \frac{\partial^2}{\partial z^2}(n_\omega - \phi_\omega)] \right\rangle$ means that energy can be dissipated via electron-ion collision hence is the parallel dissipation term. The above equation (4.7) forms the basis of one of the coupled Hasegawa-Wakatani [24] equations; however here it is expressed solely in the frequency domain without the corresponding spatial Fourier transform used in that original work.

By performing a similar process on the ion momentum equation, with the same normalizations as before, an energy balance equation related to velocity fluctuation can be obtained:

$$\begin{aligned}\left\langle \frac{1}{2} \frac{\partial |\nabla_\perp \phi_\omega|^2}{\partial t} \right\rangle &= \left\langle -\mathrm{Re} \sum_{\omega_1} (\hat{z} \times \nabla_\perp \phi_\omega^*) \cdot [(\hat{z} \times \nabla_\perp \phi_{\omega-\omega_1} \cdot \nabla_\perp)(\hat{z} \times \nabla_\perp \phi_{\omega_1})] \right\rangle \\ &+ \left\langle \frac{\mu_\perp}{\Omega_{ci} \rho_s^2} \mathrm{Re}[(\hat{z} \times \nabla_\perp \hat{\phi}_\omega^*) \cdot \nabla_\perp^2 (\hat{z} \times \nabla_\perp \hat{\phi}_\omega)] \right\rangle + \left\langle -\frac{\nu_{i-n}}{\Omega_{ci}} |\nabla_\perp \phi_\omega|^2 \right\rangle\end{aligned} \tag{4.8}$$

where $\mu_\perp$ is the ion viscosity, ν_{i-n} is the ion-neutral collision rate and neutrals have been assumed to have negligible velocity.

The kinetic energy balance equation involves only the plasma potential, in which $\left\langle \frac{1}{2} \frac{\partial |\nabla_\perp \phi_\omega|^2}{\partial t} \right\rangle$ is the rate of change of the $\underline{E} \times \underline{B}$ velocity fluctuation energy at one specific spatial position, and the term $\left\langle -\mathrm{Re} \sum_{\omega_1} (\hat{z} \times \nabla_\perp \phi_\omega^*) \cdot [(\hat{z} \times \nabla_\perp \phi_{\omega-\omega_1} \cdot \nabla_\perp)(\hat{z} \times \nabla_\perp \phi_{\omega_1})] \right\rangle$ determines how much energy is nonlinearly coupled into or out of the frequency ω. Again, a selection rule $\omega = \omega_1 + \omega_2$ is imposed on the nonlinear coupling in order for the ensemble average to have a finite value. This nonlinear term is called the kinetic energy transfer term, T_u, due to the fact that it is related to the perpendicular kinetic energy evolution. Finally, the term $\left\langle \frac{\mu_\perp}{\Omega_{ci}\rho_s^2} \mathrm{Re}[(\hat{z}\times\nabla_\perp\hat{\phi}_\omega^*)\cdot\nabla_\perp^2(\hat{z}\times\nabla_\perp\hat{\phi}_\omega)] \right\rangle$ gives the rate at which energy can be damped due to ion viscosity, and the term $\left\langle -\frac{\nu_{i-n}}{\Omega_{ci}}\left|\nabla_\perp\phi_\omega\right|^2 \right\rangle$ is a flow damping term due to ion-neutral collisions, or due to any other damping mechanism (e.g. trapped-passing ion collisions in a torus), that is simply proportional to the turbulent kinetic energy and a momentum exchange rate with a background stationary species.

The energy conservation equations (4.7) and (4.8) are simply the Fourier transformed fluid continuity and momentum equations, where the internal and kinetic nonlinear transfer terms T_n and T_u are not related to a specific pre-assumed wave coupling form, and are simply derived from the convective derivatives in the continuity and momentum equations, and where the velocity in the convective derivative is dominated by the ExB and diamagnetic drift terms. Therefore the properties of internal and kinetic energy transfer terms are very basic and physical.

By expanding the vector identities for a magnetized plasma with $\mathbf{B} = B\hat{z}$, the internal and kinetic energy transfer terms can be rewritten as:

$$\begin{aligned} T_n(\omega) &\equiv \left\langle -\mathrm{Re}[\sum_{\omega_1} n^*_\omega (\hat{z}\times\nabla_\perp\phi_{\omega-\omega_1}\cdot\nabla_\perp)n_{\omega_1}] \right\rangle \\ &\approx \left\langle \mathrm{Re}[\sum_{\substack{\omega_1=-f_{nyq} \\ |\omega-\omega_1|\le f_{nyq}}}^{\omega_1=+f_{nyq}} n^*_\omega (\frac{\partial\phi_{\omega-\omega_1}}{\partial y}\frac{\partial n_{\omega_1}}{\partial x} - \frac{\partial\phi_{\omega-\omega_1}}{\partial x}\frac{\partial n_{\omega_1}}{\partial y})] \right\rangle \end{aligned} \tag{4.9}$$

$$\begin{aligned} T_u(\omega) &\equiv \left\langle -\mathrm{Re}\sum_{\omega_1}(\hat{z}\times\nabla_\perp\phi^*_\omega)\cdot[(\hat{z}\times\nabla_\perp\phi_{\omega-\omega_1}\cdot\nabla_\perp)(\hat{z}\times\nabla_\perp\phi_{\omega_1})] \right\rangle \\ &\approx \left\langle \mathrm{Re}\sum_{\substack{\omega_1=-f_{nyq} \\ |\omega-\omega_1|\le f_{nyq}}}^{\omega_1=+f_{nyq}} [\frac{\partial\phi^*_\omega}{\partial x}(\frac{\partial\phi_{\omega-\omega_1}}{\partial y}\frac{\partial^2\phi_{\omega_1}}{\partial x^2} - \frac{\partial\phi_{\omega-\omega_1}}{\partial x}\frac{\partial^2\phi_{\omega_1}}{\partial x\partial y}) + \frac{\partial\phi^*_\omega}{\partial y}(\frac{\partial\phi_{\omega-\omega_1}}{\partial y}\frac{\partial^2\phi_{\omega_1}}{\partial x\partial y} - \frac{\partial\phi_{\omega-\omega_1}}{\partial x}\frac{\partial^2\phi_{\omega_1}}{\partial y^2})] \right\rangle \end{aligned} \tag{4.10}$$

where x (y) denote the radial (azimuthal or poloidal) directions respectively.

With energy balance equations (4.7) and (4.8), it can be seen that T_n and T_u are actually energy flow rate. If T_n is positive while all other terms in (4.7) are constant, then the energy term $|n_\omega|^2$ will grow; if T_n is negative then $|n_\omega|^2$ decreases. Similarly positive T_u renders a growth in $|\nabla\phi_\omega|^2$ while negative T_u renders a decrease in $|\nabla\phi_\omega|^2$. Therefore the bispectral terms T_n and T_u in the energy balance equations not only can tell how various three-wave interactions transfer energy into or out of fluctuations with frequency ω, but also can be used to determine the rate and direction of the nonlinear energy transfer.

By splitting the T_n and T_u into parts, more detailed insight into the origins of the nonlinear energy transfer mechanisms can be obtained. For example, if the first part,

$\mathrm{Re}[\frac{1}{M}\sum_{k=1}^{M}\frac{\partial\phi_{\omega}^{*}}{\partial x}\frac{\partial\phi_{\omega-\omega_1}}{\partial y}\frac{\partial^2\phi_{\omega_1}}{\partial x^2}]_k$, of the expanded form of the kinetic energy transfer term is positive (where k denotes the k-th ensemble of a total of M available ensembles), it means $|\nabla_{\perp}\phi_{\omega}|^2$ is gaining energy because $\frac{\partial\phi_{\omega-\omega_1}}{\partial y}$ and $\frac{\partial^2\phi_{\omega_1}}{\partial x^2}$ interact to give energy to $\frac{\partial\phi_{\omega}}{\partial x}$. Or physically this means that $u_{\theta}(\omega)$ gains energy from the radial velocity $u_r(\omega-\omega_1)$ and the azimuthal velocity shear $\partial u_{\theta}(\omega_1)/\partial r$.

If the Fourier transformed conservation equation (e.g. Eqn 4.4 or 4.8) is to exist for all frequencies, it is necessary that the equation satisfies a slowly varying assumption for all frequencies of interest. Thus if the conservation equation is written as $A(t)=0$ then the Fourier transform $A_{\omega}(t)$ will exist only if $\frac{1}{A_{\omega}(t)}\frac{\partial A_{\omega}(t)}{\partial t} << \omega$ for the frequencies of interest. The validity of this assumption must be verified from the experimental data.

The calculation and interpretation of the above T_n and T_u needs a thorough understanding of the 3-field cross-bispectrum. The auto-bispectrum introduced by Kim and Powers [11] can be easily generalized to measure the phase coherence among three different fields. The cross-bispectrum is defined as

$$\hat{S}_{XYZ}(f_1,f_2)\equiv E[X(f)Y^*(f_1)Z^*(f_2)]=\frac{1}{M}\sum_{k=1}^{M}[X(f)Y^*(f_1)Z^*(f_2)]_k \qquad (4.11)$$

Writing each signal in terms of an amplitude and phase, it can alternatively be written as,

$$\hat{S}_{XYZ}(f_1,f_2)\equiv\frac{1}{M}\sum_{k=1}^{M}[\ |X(f)Y^*(f_1)Z^*(f_2)|\,e^{i\delta\theta}]_k \qquad (4.12)$$

where $\delta\theta\equiv\theta_X(f)-\theta_Y(f_1)-\theta_Z(f_2)$ denotes the phase mismatch for a given ensemble. Clearly if $\delta\theta$ varies randomly across the ensemble average (i.e. if the random phase approximation is satisfied) then $\hat{S}_{XYZ}(f_1, f_2)$ will vanish; alternatively if $\delta\theta$ has a reproducible range of values across the ensemble average then $\hat{S}_{XYZ}(f_1, f_2)$ will have a finite value and, since the cross bispectrum is related to the energy transfer in the Fourier domain, there will be a finite exchange of energy between the frequencies involved in such cases. The calculation region can be greatly reduced because of the symmetry properties of the cross-bispectrum and by the fact that often the fluctuation frequencies of interest are much smaller than the Nyquist frequency. Figure 4.1 shows the typical calculation region for the 3-field cross-bispectrum with green (light grey), red (grey), and blue (dark grey) triangles, where the interested frequencies (assumed $\leq 9.5KHz$ for the test data used in this illustration) are much smaller than the typical Nyquist frequency. Suppose that 3 different plasma waves with frequencies, e.g. $8KHz$, $6KHz$ and $2KHz$, interact with each other. There will be a total of 6 different permutations for this interaction as shown by table 4.1, where each column stands for a different physical coupling process since it involves coupling among 3 fields (X, Y and Z). For 1-field couplings where X=Y=Z, i.e. the auto-bispectrum or auto-bicoherence, these 6 different combinations stand for exactly the same physical process.

Table 4.1. A layout of all possible combinations of 3-wave interactions with different frequencies $8KHz$, $6KHz$ and $2KHz$.

X	8KHz	8KHz	6KHz	6KHz	2KHz	2KHz
Y	2KHz	6KHz	8KHz	-2KHz	8KHz	-6KHz
Z	6KHz	2KHz	-2KHz	8KHz	-6KHz	8KHz

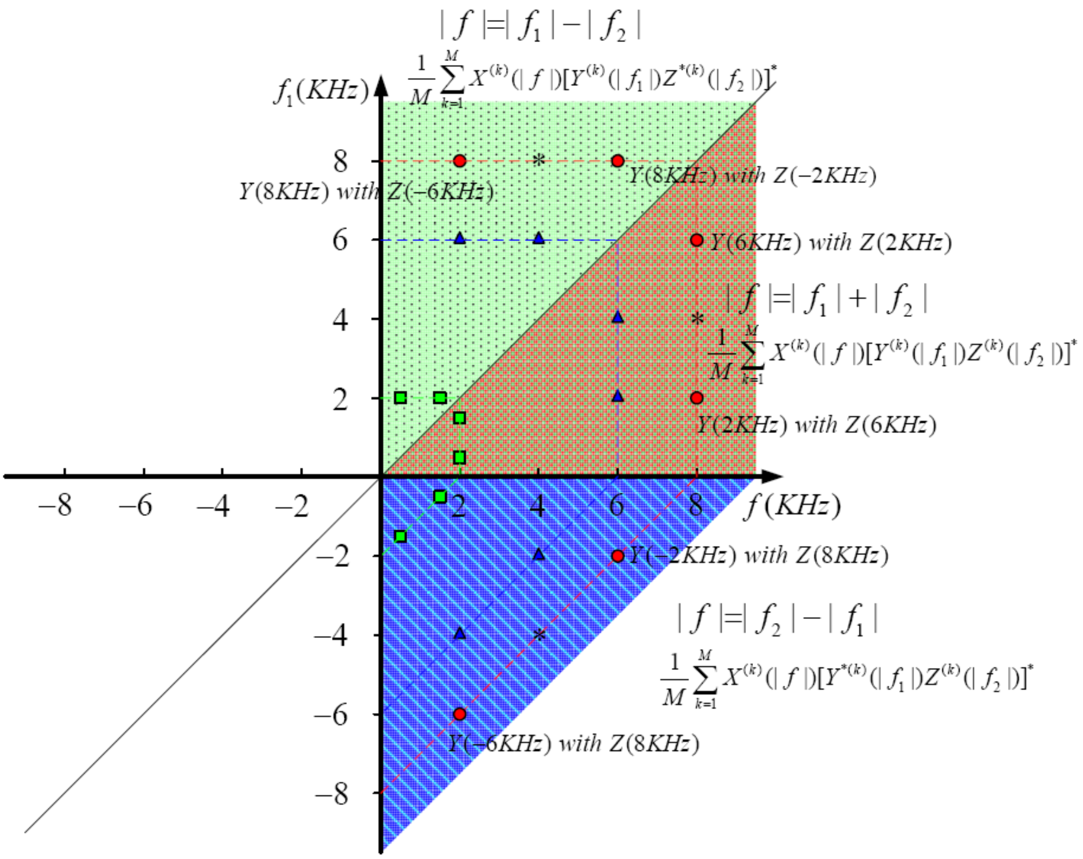
$|f|=|f_1|-|f_2|$
$\frac{1}{M}\sum_{k=1}^{M} X^{(k)}(|f|)[Y^{(k)}(|f_1|)Z^{*(k)}(|f_2|)]^*$
$f_1(KHz)$
8
6
4
2
−2
−4
−6
−8
$Y(8KHz)$ with $Z(-6KHz)$
$Y(8KHz)$ with $Z(-2KHz)$
$Y(6KHz)$ with $Z(2KHz)$
$|f|=|f_1|+|f_2|$
$\frac{1}{M}\sum_{k=1}^{M} X^{(k)}(|f|)[Y^{(k)}(|f_1|)Z^{(k)}(|f_2|)]^*$
$Y(2KHz)$ with $Z(6KHz)$
−8
−6
−4
−2
2
4
6
8
$f(KHz)$
$Y(-2KHz)$ with $Z(8KHz)$
$|f|=|f_2|-|f_1|$
$\frac{1}{M}\sum_{k=1}^{M} X^{(k)}(|f|)[Y^{*(k)}(|f_1|)Z^{(k)}(|f_2|)]^*$
$Y(-6KHz)$ with $Z(8KHz)$

Figure 4.1. Calculation region for 3-field (X,Y, Z) cross-bispectrum and cross-bicoherence. The x-axis is for field X and y-axis is for field Y.

Red (grey): $f,\ f_1,\ f_2 > 0$, means that the way $Y(f_1)$ and $Z(f_2)$ interact is via the summation condition $|f|=|f_1|+|f_2|$, and the phase relation is $\theta_X(f)=\theta_Y(f_1)+\theta_Z(f_2)$.

For the green region the frequencies satisfy the condition: $f,\ f_1 > 0$ and $f_2 < 0$ and satisfy a frequency relation $|f|=|f_1|-|f_2|$ and phase relation $\theta_X(f)=\theta_Y(f_1)-\theta_Z(|f_2|)$.

For the blue region the frequencies satisfy the condition $f,\ f_2 > 0$ and $f_1 < 0$, and satisfy the frequency relation $|f|=|f_2|-|f_1|$ and phase relation is $\theta_X(f)=\theta_Y(f_2)-\theta_Z(|f_1|)$.

In figure 4.1, with the x-axis for field X and y-axis for field Y, all the 6 different combinations are indicated accordingly by the red dots. In the region with red (grey) color ($f,\ f_1,\ f_2 > 0$) $Y(f_1)$ and $Z(f_2)$ interact so that $|f| = |f_1| + |f_2|$, and the phase relation is $\theta_X(f) = \theta_Y(f_1) + \theta_Z(f_2)$. E.g., for the dot at $(f = 8KHz, f_1 = 2KHz)$ we can infer that f_2 corresponding to field Z must be $6KHz$, and the phase relation for this coupling must be $\theta_X(8KHz) = \theta_Y(2KHz) + \theta_Z(6KHz)$. in the green (light grey) region, $f,\ f_1 > 0$ and $f_2 < 0$, the frequency relation is $|f| = |f_1| - |f_2|$, and the phase relation is $\theta_X(f) = \theta_Y(f_1) - \theta_Z(|f_2|)$. in the blue (dark grey) region, $f,\ f_2 > 0$ and $f_1 < 0$, the frequency relation is $|f| = |f_2| - |f_1|$, and the phase relation is $\theta_X(f) = \theta_Y(f_2) - \theta_Z(|f_1|)$. Since the frequency selection rule for 3-wave coupling is typically written as $f = f_1 + f_2$, negative frequencies are used here to correspond to physical processes when two frequencies subtract to generate the third, e.g. f_1 subtract f_2 to generate f.

4.3 Experimental measurement of multi-field nonlinear energy transfer

To experimentally determine the internal energy transfer term T_n one can measure the density and potential fluctuations, compute their derivatives in the radial and azimuthal directions, Fourier transform those quantities into frequency domain to find n_ω, $\frac{\partial n_\omega}{\partial x}$, $\frac{\partial n_\omega}{\partial y}$ and $\frac{\partial \phi_\omega}{\partial x}$, $\frac{\partial \phi_\omega}{\partial y}$, and finally construct T_n by convolution. For the kinetic energy transfer T_u, plasma potential and its first and second derivatives are needed.

The quantities needed to infer both T_n and T_u can be obtained experimentally using the spatial layout of density and potential measurements shown in figure 4.2 where the radial direction is denoted as $\hat{x}$, and the azimuthal or poloidal direction is denoted as $\hat{y}$ direction.

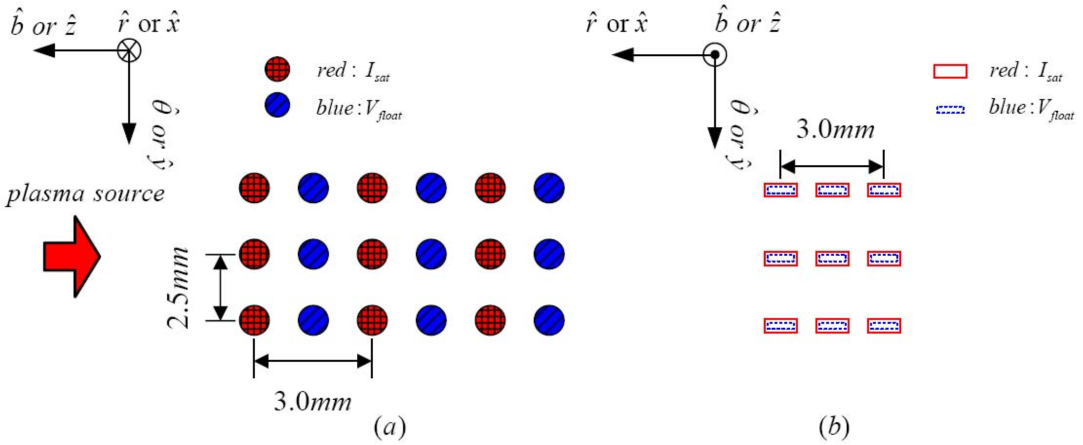
$\hat{b}$ or $\hat{z}$
$\hat{r}$ or $\hat{x}$
$\hat{\theta}$ or $\hat{y}$
plasma source
$red: I_{sat}$
$blue: V_{float}$
2.5mm
3.0mm
(a)
$\hat{r}$ or $\hat{x}$
$\hat{b}$ or $\hat{z}$
$\hat{\theta}$ or $\hat{y}$
3.0mm
$red: I_{sat}$
$blue: V_{float}$
(b)

Figure 4.2. Spatial layout of the measurement grid points. (b) is the side view of (a). All the probe tips are identical, but the V_{float} tips were purposely drawn smaller in (b) in order to distinguish the I_{sat} tips from V_{float} tips. All the derivatives $\frac{\partial \phi}{\partial x}$, $\frac{\partial \phi}{\partial y}$, $\frac{\partial^2 \phi}{\partial x^2}$, $\frac{\partial^2 \phi}{\partial y^2}$ and $\frac{\partial^2 \phi}{\partial x \partial y}$ can be computed using finite difference method from the 9 channels of potential (blue). n, $\frac{\partial n}{\partial x}$ and $\frac{\partial n}{\partial y}$ can be computed from the 9 channels of density (red).

In this figure, potential fluctuation channels are indicated by blue while the density channels are denoted by red. The finite difference method can then be used to compute estimates of the derivatives. For example, the central finite difference approximation can be used to calculate

$\left.\frac{\partial\phi}{\partial x}\right|_{x=x_i} \approx \frac{\phi_{i+1}-\phi_{i-1}}{2\Delta x}$ with a leading error of $(\Delta x)^2$, and $\left.\frac{\partial^2\phi}{\partial x^2}\right|_{x=x_i} \approx \frac{\phi_{i-1}+\phi_{i+1}-2\phi_i}{(\Delta x)^2}$ with a leading error proportional to $(\Delta x)^2$. With additional grid points, a higher accuracy of finite difference can be achieved. In our experiments, the choice of Δx should be much less than the size of typical turbulent structures, and at the same time large enough so that the phase difference among adjacent tips is measureable. In our experiment, the typical turbulent correlation lengths are $0.6 \sim 2cm$ [25]; the ion sound radius $\rho_S = \frac{C_s}{\Omega_{C_i}} \sim 1cm$ and the spatial separation between tips is 1.5mm in radial direction and 2.5mm in azimuthal direction. We find that the typical phase shift between spatially separated probe tips is ~2-3 radian, which is significantly larger than the statistical uncertainty estimated as << 0.1 radian in the cross phase shift measurements. Actually the statistical noise is not a concern when computing the CSDX plasma turbulence statistics due to the reasons mentioned in the previous chapter.

Because all the derivatives are computed in a rectangular coordinate for cylindrical plasmas in our experiment, it is required that the plasma scale is much larger than the scale of the measurement array. Alternatively one can layout the grid points on magnetic surfaces, and correspondingly use a cylindrical coordinate to compute all the derivatives. The layout in figure 4.2 is setup such that the center of potential channels are the same as the center of density channels in both azimuthal and radial directions, which makes every calculated derivative centered and thus eliminates the phase shift in both radial and azimuthal directions. If the two 3x3 array are spatially shifted by a displacement vector $\delta\mathbf{x}$ relative to each other, then the phase shift $\mathbf{k}\cdot\delta\mathbf{x}$ incurred from this effect due to the wavenumber **k** would need to be accounted for in computing the cross spectral quantities. As long as this shift is small compared to the turbulence scale lengths, then such a correction can in principle be applied. In our experiment, the two 3x3 arrays are shifted by 1.5mm along the magnetic field line, but the corresponding phase shift is negligible since $k_{\|} \ll k_{\perp}$ for the fluctuations. Generally the density and potential (or velocity) field can be measured in a variety of ways, such as Langmiur probe, heavy ion beam probe (HIBP) [26] or velocimetry of beam emission spectroscopy (BES) [27]. For the study of plasmas in linear devices or edge plasmas in Tokamaks, a multi-point Langmiur probe array is a good candidate for its excellent spatial resolution, relative easiness to design and construct, and the lower cost compared to other techniques. However, we explicitly note that such nonlinear energy transfer studies are also possible with these other diagnostic approaches provided that the necessary multipoint data can be obtained.

Using the approach discussed above, multifield nonlinear energy transfer measurements have been carried out on the CSDX device at the University of California, San Diego. For the experiments reported here the discharges were operated with 1000 Gauss magnetic field and 3.0mtorr argon filling pressure, the helicon plasma source was operated at 13.56 MHz with a power of 1.5KW; the resulting plasma had a peak on-axis density $\sim 10^{13}\,\mathrm{cm}^{-3}$ and on-axis electron temperature $\sim 3\ \mathrm{eV}$. The plasma source has a diameter of 10 cm, and the vacuum chamber has a diameter of 20 cm. Further details about the device and characteristics of the plasma and of the transition to a state of weak turbulence can be found elsewhere [19, 28].

A dual 3×3 tip Langmiur array was built and installed on CSDX, which enables us to simultaneously measure 9 channels of plasma density and 9 channels of floating potential on a

$x-y$ grid as shown in Figure 4.2. Therefore all the quantities needed for constructing the internal and kinetic energy transfer terms can be obtained by this probe array. Although for the purpose of measuring energy transfer only the first derivatives of density are needed, thus 4 channels of density are enough, the 5 redundant density channels either can be used to compute the second derivatives or can be setup for other purposes such as triple probe array [29] to measure plasma potential and electron temperature. A general concern could be that the layout of Isat and floating potential tips would introduce a shadowing effect among them, especially between Isat and floating potential tips, and thus could distort the measured bispectra. Experiments have been carried out to compare the obtained kinetic energy transfer coefficients at the conditions with or without Isat bias voltage. No significant differences have been found between these two cases suggesting that any such shadowing effects are small.

4.4 Experimental results

Figure 4.3 shows the typical profiles of CSDX plasma operated with a magnetic field of 1000 Gauss, an argon fill pressure of 3.0mtorr and an RF power input of 1.5KW. The plasma density profile presented in figure 4.3(a) is measured by the 18-tip probe array. Figure 4.3(b) shows the plasma azimuthal velocity profile calculated from 2D visible light imaging using a time delay estimation technique [30]. We find that the azimuthal velocity grows and decays with a frequency of ~250Hz; the radial profiles show that the shearing rate also varies in magnitude at the same frequency [31]. Previous results, which were obtained by ensemble averaging over many such oscillation cycles showed that the resulting time-averaged shear flow is consistent with the measured time-averaged turbulent Reynolds stress and the estimated damping profiles [1]. As we show below, the bispectral calculation shows that both internal and kinetic energy are transferred from drift turbulence to this velocity oscillation. Figure 4.3(c) is the time-averaged electron temperature profile taken from a previous published chapter [28]

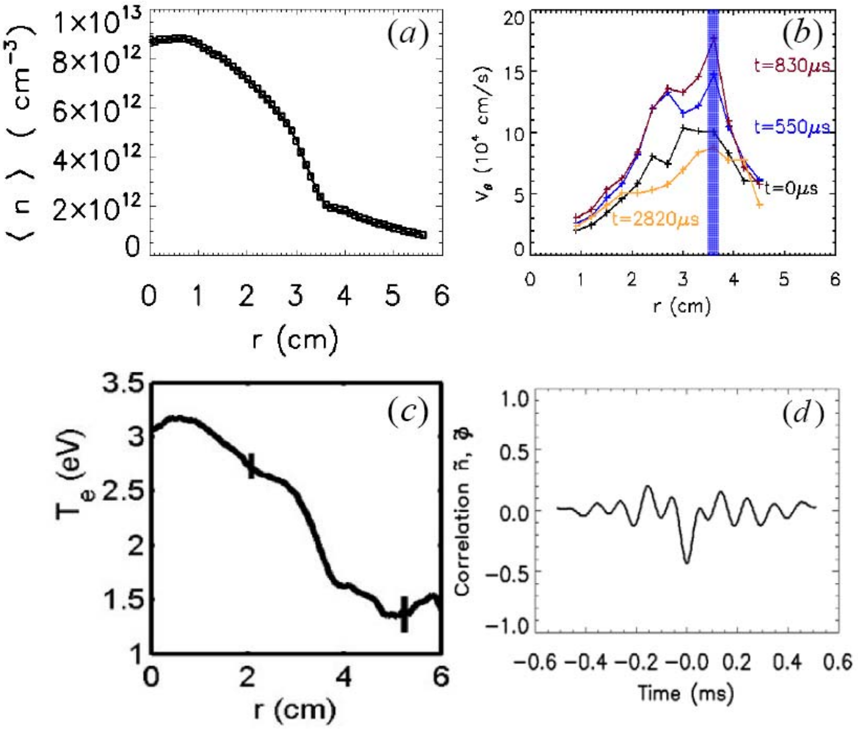

Figure 4.3 (a) Time-averaged plasma density. (b) Time resolved plasma azimuthal velocity profile calculated from 2D visible light imaging using Time Delay Estimation [31]. It is found that the velocity at the shadowed region $r \sim 3.6cm$ develops and decays at the frequency around 250Hz. (c) Time-averaged electron temperature profile [28]. (d) Correlation between density and potential fluctuations at shear layer.

All the potential and density channels were simultaneously sampled at 500 kHz, and the total sampling time was 10 seconds giving a total of 5 million sampling points for each channel. These time series were then divided into one to several thousand independent realizations to produce statistically converged bispectra using ensemble averaging. Figure 4.4 shows the convergence test for the bispectral calculation of the internal and kinetic energy transfer terms $T_n(f, f_1)$ and $T_u(f, f_1)$ at the frequencies $f = 0.25KHz$ and $f_1 = 10.25KHz$. We can see that both the internal and kinetic bispectra are reasonably converged when at least ~1000 realizations are used. As is shown below, the existence of very slowly varying nonlinearly driven fluctuations such as zonal flows imposed a physics requirement for high frequency resolution. This requirement, combined with the large number of ensembles required for convergence implies the requirement for long time series (with ~10^7 samples per channel) and highly stationary experimental conditions. A similar number of realizations are required to converge at other combinations of f and f1.

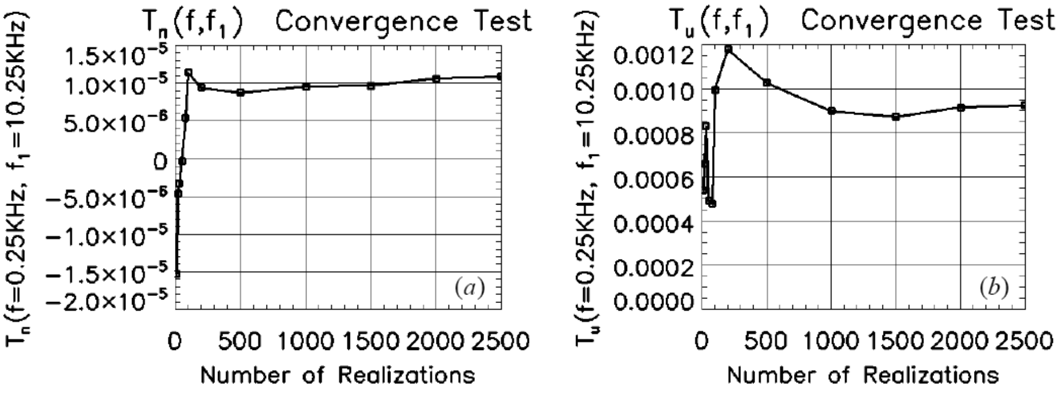

Figure 4.4 Convergence test for the bispectral calculation for the internal and kinetic energy transfer terms $T_n(f, f_1)$ and $T_u(f, f_1)$ at the frequencies $f = 0.25KHz$ and $f_1 = 10.25KHz$. (a) is for $T_n(f = 0.25KHz, f_1 = 10.25KHz)$ and (b) is for $T_u(f = 0.25KHz, f_1 = 10.25KHz)$.

Before examining the nonlinear turbulence energy transfer processes of interest, it is important to determine if the ansatz $\frac{1}{|n_{\omega}(\underline{x},t)|}\frac{\partial|n_{\omega}(\underline{x},t)|}{\partial t} \ll \omega$ is satisfied. To determine this, the experimentally measured density was first normalized by its time-averaged value to give n(x,t), and then band pass filtered for several representative frequency ranges. The relevant frequency ranges are chosen based upon previously published spectral results [19] and plotted as function of time in figures 4.5(a), 4.5(b) and 4.5(c). Figure 4.5(a) corresponds to the band pass filtered over a range $0.2 \sim 0.5\text{KHz}$, in which the envelope of density fluctuations varies with a period of $15 \sim 20\text{ms}$ ($50 \sim 67\text{Hz}$) a factor of 6 slower than the corresponding phase change frequency approximated by the center value of the filter. Figure 4.5(b) is density fluctuation filtered by $0.8 \sim 1.2\text{KHz}$, where the envelope shows a period of $6 \sim 9\text{ms}$ ($110 \sim 170\text{Hz}$), i.e. a factor of ~10x slower variation than the fluctuation frequency. Figure 4.5(c) is the density fluctuation filtered by $9.0 \sim 10.0\text{KHz}$, and the envelope has a period of $2.0 \sim 2.3\text{ms}$ ($430 \sim 500\text{Hz}$) which again is a factor of ~10-20x longer than the fluctuation period under consideration. Thus from figures 4.5(a), 4.5(b) and 4.5(c) we can tell that for the conditions of these experiments the amplitude of density fluctuations varies on a timescale that is a factor of ~5-20x slower than the corresponding phase changes. By following the same process, it has been verified that this is also true for $\nabla_{\perp}\phi$. Figures 4.5(d) through 4.5(f) show similar results calculated for the left hand side of Eq. (4.2) from measured data. We therefore conclude from this study that the slowly varying assumption is reasonably well satisfied by the experimental data.

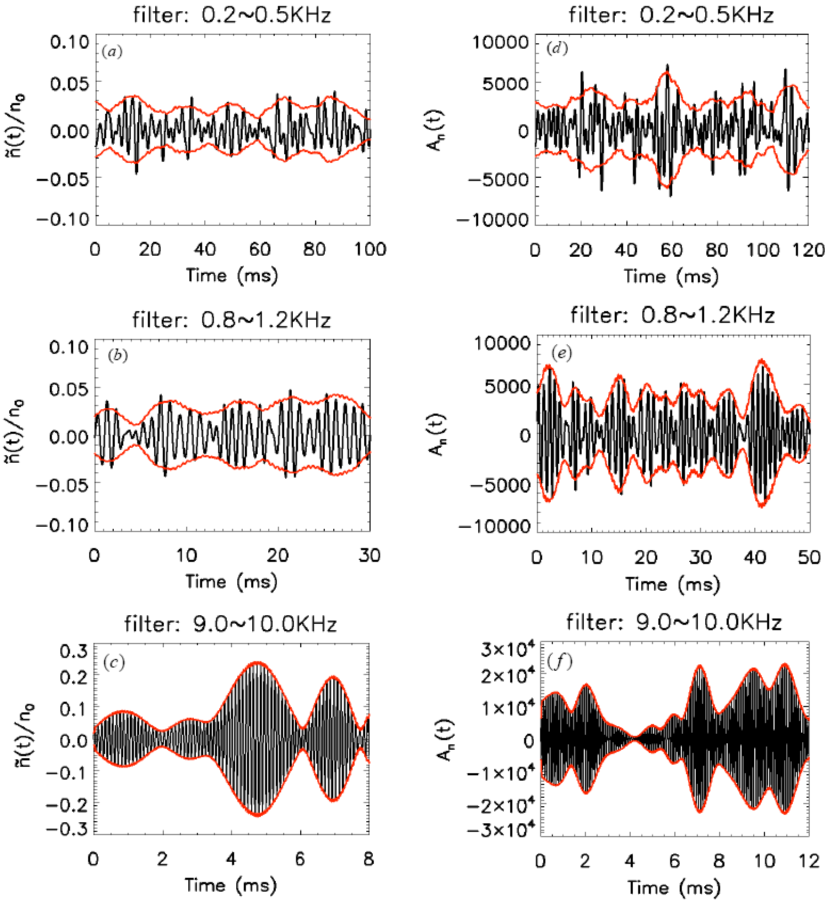

Figure 4.5 (a)0.2~0.5kHz band-pass-filtered density fluctuation $\tilde{n}(t)$ plotted as a function of time. The envelope shows a period of 15-20 ms, indicating a slowly variation of the spectra at 0.2~0.5kHz. (b) 0.8~1.2kHz band-pass-filtered density fluctuation. The envelope has a period of 6-9 ms. (c) 9.0~10kHz filtered density fluctuation with a enveloped period of 2-4 ms. (d) 0.2~0.5kHz band-pass-filtered total derivative of density fluctuation $A(t) \equiv (\frac{\partial}{\partial t} + \vec{u}\cdot\nabla)n(t)$ plotted as a function of time. The envelope shows a period of 15-20 ms, indicating a slowly variation of the spectra at 0.2~0.5kHz. (e) 0.8~1.2kHz band-pass-filtered total derivative of density fluctuation. The envelope has a period of 8-10 ms. (f) 9.0~10kHz filtered total derivative of density fluctuation with a enveloped period of 3-5 ms.

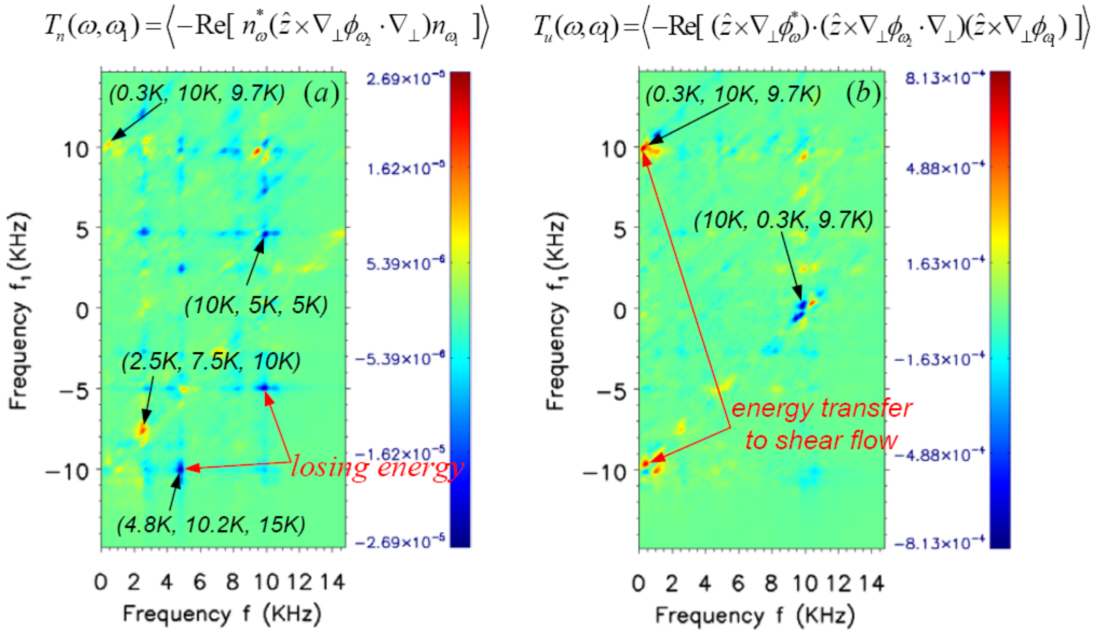

Figure 4.6. Measurement is taken at $r = 3.6cm$, magnetic field 1000Gauss, RF power 1.5KW and pressure 3.0mtorr. (a) Bispectral internal energy transfer $T_n(\omega,\omega_1)$ (in both (a) and (b) the x-axis corresponds to ω and y-axis corresponds to ω_1 in equation (4.7) and (4.8), and notation $\omega_2 = \omega - \omega_1$). (b) Bispectral kinetic energy transfer $T_u(\omega,\omega_1)$

The internal and kinetic energy transfer functions derived in this manner are shown in figure 4.6, which was obtained when the probe was centered on the shear layer located at r=3.6cm, with magnetic field 1000Gauss, RF power 1.5KW and pressure 3.0mtorr. These conditions are the same as those used to study the origin of the shear layer in previous work [1, 5]. In computing the bispectra in figure 4.6, for each channel a total of 5 million samples were divided into 1200 ensembles, with 4096 samples in each ensemble. Since a sampling frequency of 500KHz was used when acquiring the data, the frequency resolution in figure 4.6 is about 120Hz. Figure 4.6(a) shows the internal energy transfer $T_n(\omega, \omega_1)$, and figure 4.6(b) shows the kinetic energy transfer coefficient $T_u(\omega, \omega_1)$.

From the energy balance equation (4.7) and (4.8), we know that positive (negative) internal or kinetic energy transfer means that fluctuations at frequency ω gain (lose) energy through the wave-wave interaction with ω_1 and $\omega - \omega_1$. In both plots the x-axis is ω and y-axis is ω_1. Several prominent 3-wave coupling triplets are indicated in these two figures, such as the triplet $(10K,\ 5K,\ 5KHz)$ in Figure 4.6(a). The negative value for $T_n(\omega, \omega_1)$ at $(\omega = 10KHz,\ \omega_1 = 5KHz)$ means that density fluctuation n at 10KHz loses energy to either $\nabla_\perp \phi$ at 5KHz or $\nabla_\perp n$ at 5KHz ($\omega - \omega_1 = 5KHz$). There is an uncertainty of which frequency is receiving energy because we can only tell from the energy conservation equation (4.7) that the frequency ω is gaining or losing energy, but it is not possible to determine into which wave the energy is moving. Similarly in figure 4.6(b) the positive value for $T_u(\omega, \omega_1)$ at $(\omega = 0.3KHz,\ \omega_1 = 10KHz)$ means that the velocity ($\hat{z} \times \nabla_\perp \phi / B$) at 9.7KHz interact with the vorticity $\nabla_\perp^2 \phi$ at 10KHz to transfer energy to the velocity fluctuation occurring at 0.3KHz.

The frequency and wave number resolved two-point estimated spectrum has been measured on CSDX [1], which shows that small scale drift turbulence is typically with a k_θ bigger than 1cm^{-1} and with a frequency of several KHz to 20KHz; while large scale azimuthal flow has both the k_θ and frequency close to zero. By using this measured local spectra, we can conclude that the positive value for $T_u(\omega, \omega_1)$ at $(\omega = 0.3KHz,\ \omega_1 = 10KHz)$ in figure 4.6(b) is a clear sign of energy transfer from a turbulent flow to a large-scale shear flow, since we have found that this 0.3KHz velocity fluctuation is associated with the slow evolution of the sheared zonal flow as summarized above and shown in detail elsewhere [31]. In figure 4.6(b) the negative value for T_u at $(\omega = 10KHz,\ \omega_1 = 0.3KHz)$ means the velocity at 10KHz loses energy through 3-wave coupling with $\nabla_\perp^2 \phi$ at 0.3KHz and the velocity at 9.7KHz. If we expand T_u into 4 different parts and calculate them separately from experimental data, we will find that there is one part, $\mathrm{Re}\{\frac{1}{M}\sum_{k=1}^{M}[\frac{\partial \phi_\omega^*}{\partial x}\frac{\partial \phi_{\omega-\omega_1}}{\partial y}\frac{\partial^2 \phi_{\omega_1}}{\partial x^2}]_k\}$, that dominates others. This means that the nonlinear kinetic energy transfer to azimuthal shear flow is mostly due to the radial flux of vorticity (due to the fact that in the experimental data $\frac{\partial^2 \phi}{\partial x^2}$ dominates $\frac{\partial^2 \phi}{\partial y^2}$ and $\frac{\partial^2 \phi}{\partial x \partial y}$ in the expansion form of $\nabla_\perp^2 \phi$). Or it can be interpreted that azimuthal velocity shear couples with radial velocity to transfer energy to shear flow. The internal energy transfer also has a similar feature. These relevant arguments and physical interpretation will be discussed in detail in the next chapter.

4.5 Summary and discussions

In this chapter, a method for studying the nonlinear energy transfer with a two-field (density and potential) model, including both theoretical derivation and experimental setup, are proposed and explained. Experimental results measured at the shear layer give a clear picture of wave coupling and energy transfer. This is the first time that nonlinear energy transfer is experimentally studied using a two-field model in frequency domain.

Calculating bispectrum (essentially a convolution) is slow and computationally expensive.

Instead of doing convolutions in frequency domain, an alternate way to calculate the nonlinear energy transfer coefficients is to first construct an effective time series in real time domain using time series of density and potential, then take the Fourier transform of the constructed time series to get energy transfer coefficients. This approach is much faster than directly calculating bispectra in frequency domain. For example, the internal energy transfer coefficient can be formulated as:

$$T_n \equiv \left\langle -\mathrm{Re}\sum_{\omega_1} n_\omega^* (\hat{z}\times\nabla_\perp\phi_{\omega-\omega_1}\cdot\nabla_\perp) n_{\omega_1} \right\rangle \approx \left\langle \mathrm{Re}\sum_{\substack{\omega_1=-f_{nyq} \\ |\omega-\omega_1|\le f_{nyq}}}^{\omega_1=+f_{nyq}} n_\omega^* \left(\frac{\partial\phi_{\omega-\omega_1}}{\partial y}\frac{\partial n_{\omega_1}}{\partial x} - \frac{\partial\phi_{\omega-\omega_1}}{\partial x}\frac{\partial n_{\omega_1}}{\partial y}\right) \right\rangle$$

(4.13)

But it can also be reformulated as:

$$T_n \equiv \left\langle -\mathrm{Re}\sum_{\substack{\omega_1,\omega_2 \\ \omega=\omega_1+\omega_2}} n_\omega^* (\hat{z}\times\nabla_\perp\phi_{\omega_1}\cdot\nabla_\perp) n_{\omega_2} \right\rangle = \left\langle \mathrm{Re}\{\,[\mathrm{FFT}(n)]^* \mathrm{FFT}[\frac{\partial\phi}{\partial y}\frac{\partial n}{\partial x} - \frac{\partial\phi}{\partial x}\frac{\partial n}{\partial y}]\,\} \right\rangle$$

(4.14)

According to equation (4.14), one can first construct a time series $\frac{\partial\phi}{\partial y}\frac{\partial n}{\partial x} - \frac{\partial\phi}{\partial x}\frac{\partial n}{\partial y}$, then take the cross-power of density n and this effective time series. Note that this approach can only produce the coefficients summed over ω_1. When one desires to determine the interacting triplets, then the results contained in figures 4.6(a) and 4.6(b) are needed and the method computing convolution should be used. Due to finite signal sampling frequency of real data acquisition systems, these two methods may produce slightly different curves (difference comes from the fact that Fast Fourier Transform of a finite time series is defined from circular convolution instead of a linear convolution). However, when the sampling frequency is sufficiently high, the difference is negligible. We plan to discuss this approach and comparing it to the cross-bispectral technique in a separate chapter.

The method proposed in this chapter is completely in frequency domain. The disadvantage of this approach is that it is not formulated in wavenumber space which may make comparison with analytic theory and simulation more difficult (although in principle simulations can calculate these quantities in frequency space exactly, provided that they are run for enough time and that any possible frame transformation between laboratory and plasma center of mass frame due to bulk rotation is accounted for). One way to overcome this difficulty could be combining these results with a measured dispersion relation to relate frequencies to azimuthal wave numbers. Also note that in this experiment, the floating potential instead of plasma potential is used to calculate electric field and the fluid velocity. This approach has essentially neglected the effect introduced by electron temperature fluctuations. One interesting future work could be including density, potential and temperature fluctuations to study the quadratic nonlinearity in a 3-field model via a straightforward extension of this approach to a system that includes particle, momentum and heat conservation equations.

All the contents of the next chapter, including text and data, has been published as it appears in “Fourier-domain study of drift turbulence driven sheared flow in a laboratory plasma”, M. Xu, G. R. Tynan, C. Holland, Z. Yan, S. H. Mueller, J. H. Yu, Phys. Plasmas 17, 032311 (2010). The dissertation author is the primary investigator and author of this article.

References:

[1] G. R. Tynan, C. Holland, J. H. Yu, A. James, D. Nishijima, M. Shimada, N. Taheri, Plasma Phys. Control. Fusion **48** S51-S73 (2006)

[2] P. H. Diamond, S. I. Itoh, K. Itoh, and T. S. Hahm, Plasma Phys. Control. Fusion **47** R35-R161 (2005)

[3] F. W. Perkins, C. W. Barnes, D. W. Johnson, S. D. Scott, M. C. Zarnstorff, M. G. Bell, R. E. Bell, C. E. Bush, B. Grek, K. W. Hill, D. K. Mansfield, H. Park, A. T. Ramsey, J. Schivell, B. C. Stratton, and E. Synakowski, Phys. Fluids B **5**, 477 (1993)

[4] J. P. Christiansen, P. M. Stubberfield, J. G. Cordey, C. Gormezano, C. W. Gowers, J. O'rourke, D. Stork, A. Taroni, and C. D. Challis, Nucl. Fusion **33** 863 (1993)

[5] C. Holland, J. H. Yu, A. James, D. Nishijima, M. Shimada, N. Taheri, and G. R. Tynan, Phys. Rev. Lett. **96** 195002 (2006)

[6] G. R. Tynan, R. A. Moyer, and M. J. Burin, Phys. Plasmas **8** 2691 (2001)

[7] A. Hasegawa and C. G. Maclennan, Phys. Fluids **22** (11) 2122-2129 (1979)

[8] C. P. Ritz and E. J. Powers, Physica **20**D 320-334 (1986)

[9] J. S. Kim, R. J. Fonck, R. D. Durst, E. Fernandez, P. W. Terry, S. F. Paul, and M. C. Zarnstorff, Phys. Rev. Lett. **79** 841-844 (1997)

[10] Y. C. Kim, J. M. Beall, E. J. Powers, and R. W. Miksad, Phys. Fluids **23** (2) 258-263 (1980)

[11] Y. C. Kim and E. J. Powers, IEEE Trans. Plasma Sci. **PS-7** No. 2 120-131 (1979)

[12] C. W. Van Atta, and J. C. Wyngaard, J. Fluid Mech. **72**, 673 (1975)

[13] T. T. Yeh, and C. W. Van Atta, J. Fluid Mech. **58**, 233 (1973)

[14] C. W. Van Atta, and W. Y. Chen, J. Fluid Mech. **38**, 743 (1969)

[15] C. P. Ritz, E. J. Powers, and R. D. Bengtson, Phys. Fluids **B 1** (1) 153-163 (1989)

[16] J. S. Kim, R. D. Durst, R. J. Fonck, E. Fernandez, A. Ware, and P. W. Terry, Phys. Plasmas **3** (11) 3998-4009 (1996)

[17] M. D. Millionshchikov, Dokl. Akad. Nauk SSSR **32** 611 (1941)

[18] G. A. Hallock and A. J. Wootton, Phys. Rev. Lett. **59** 1301 (1987)

[19] M. J. Burin, G. R. Tynan, G. Y. Antar, N. A. Crocker, and C. Holland, Phys. Plasmas **12** 052320 (2005)

[20] S. J. Camargo, D. Biskamp and B. D. Scott, Phys. Plasmas **2** 48 (1995)

[21] P Manz, M Ramisch, U Stroth, V Naulin and B D Scott, Plasma Phys. Control. Fusion **50** 035008 (2008)

[22] C. Holland, G. R. Tynan, R. J. Fonck, G. R. Mckee, J. Candy and R. E. Waltz, Phys. Plasmas **14** 056112 (2007)

[23] G. R. Tynan, P. H. Diamond, O. Gurcan, C. Holland, S. H. Muller, M. Xu, Z. Yan, J. Yu, P. Manz, M. Ramisch, U. Stroth, Y. Nagashima, S. I. Itoh, M. Yagi, S. Inagaki, A. Fujisawa, N. Kasuya, K. Itoh, T. Windisch, O. Grulke, T. Klinger, 22nd IAEA Fusion Energy conference, Geneva, Switzerland, 2008, IAEA-CN-165/EX/P5-40

[24] A. Hasegawa and M. Wakatani, Phys. Rev. Lett. **50** 682 (1983)

[25] Z. Yan, J. H. Yu, C. Holland, M. Xu, S. H. Muller, and G. R. Tynan, Phys. Plasmas **15** 092309 (2008)

[26] P. M. Schoch, A. Carnevali, K. A. Conner, T. P. Crowley, J. C. Forster, R. L. Hickok, J. F. Lewis, J. G. Schatz, Jr., and G. A. Hallock, Rev. Sci. Instrum. **59**, 1646 (1988)

[27] G. R. Mckee, R. J. Fonck, D. K. Gupta, D. J. Schlossberg, and M. W. Shafer, Rev. Sci. Instrum. **75** 3490-3492 (2004)

[28] G. R. Tynan, M. J. Burin, C. Holland, G. Antar, and N. Crocker, Phys. Plasmas **11** 5195 (2004)

[29] J. Wesson, Tokamaks, 2nd edition, Clarendon Press-London 1997, pp519

[30] J. H. Yu, C. Holland, G. R. Tynan, G. Antar and Z. Yan, J Nucl Mater **363**, 728-732 (2007)

[31] Yan Z., Turbulenct-driven shear slow and self-regulating drift wave turbulence in a cylindrical plasma device, PhD Thesis, University of California, San Diego (2008).

Chapter 5

Fourier-domain study of drift turbulence driven sheared flow in a laboratory plasma

5.1 Introduction

Turbulent nonlinear energy transfer is important since it is directly related to questions of how plasma fluctuation energy is redistributed and how large scale structures, e.g. zonal flows, are formed. Great efforts [Ref. 1-7] have been put into this issue ever since Ritz et al [8] experimentally measured the nonlinear energy transfer using a one-field model. Because it is difficult to measure plasma potential in large tokamaks (especially when a large number of spatial channels are needed) linear plasma machines become ideal devices to study the nonlinear dynamics involving turbulence and shear flows. Earlier work [9] in the CSDX device suggested that turbulent energy is nonlinearly coupled to the linearly stable low k_θ zonal flow region, and further time-domain investigations by Tynan et al [2] and Holland et al [3] provided direct experimental support for the drift-turbulence-driven mechanism of zonal flows in this plasma. In that work, the experimentally measured Reynolds Stress was used in a turbulent azimuthal momentum conservation analysis, which produced a time-averaged azimuthal velocity profile that agrees reasonably well with experimental measurements. The dynamic interplay between zonal flows and drift turbulence has also been studied in detail by Yan et al [10], which showed that a slow variation in the shear flow is accompanied by a corresponding variation in the Reynolds Stress.

In this chapter we report the results from a direct nonlinear energy transfer measurement based on the technique described in the former chapter, which gives a frequency domain measurement of the nonlinear convective terms in the continuity and momentum equations. These measured nonlinear energy transfer rates were then mapped into the azimuthal wavenumber domain using experimentally measured dispersion relation. The results show clearly a net energy transfer from the linearly unstable drift wave turbulence region with intermediate frequencies to both low frequency and high frequency regions. A comparison with linear stability of drift waves is also reported here. The content of this chapter is deeply related to the issue of turbulent transport in magnetically confined fusion as seen in [11-16].

This chapter is organized as follows. Section 5.2 gives a description of the experimental setup, section 5.3 shows the detailed nonlinear energy transfer measurement, section 5.4 shows results from the linear eigenmode analysis and finally section 5.5 gives a summary and a discussion of the results.

5.2 Experimental setup

As discussed in our earlier work [1] and in the previous chapter, by Fourier transforming the momentum and continuity equations, ensemble-averaged energy transport equations for the spectra of density and potential fluctuations can be derived in frequency domain, where the internal and kinetic energy transfer rates come from convective derivatives $\vec{u}\cdot\nabla n$ and $\vec{u}\cdot\nabla\vec{u}$, and are defined, respectively, as;

$$T_n(f,f_1) \equiv -\mathrm{Re}\left\langle n_f^*\left(\vec{u}_{\perp f_2}\cdot\nabla_\perp\right)n_{f_1}\right\rangle = -\mathrm{Re}\left\langle n_f^*\left(\hat{z}\times\nabla_\perp\phi_{f_2}\cdot\nabla_\perp\right)n_{f_1}\right\rangle \tag{5.1}$$

$$\begin{aligned} T_u(f,f_1) &\equiv -\mathrm{Re}\left\langle \vec{u}_{\perp f}^*\cdot\left(\vec{u}_{\perp f_2}\cdot\nabla_\perp\vec{u}_{\perp f_1}\right)\right\rangle \\ &= -\mathrm{Re}\left\langle\left(\hat{z}\times\nabla_\perp\phi_f^*\right)\cdot\left[\left(\hat{z}\times\nabla_\perp\phi_{f_2}\cdot\nabla_\perp\right)\left(\hat{z}\times\nabla_\perp\phi_{f_1}\right)\right]\right\rangle \end{aligned} \tag{5.2}$$

where $\langle\ \rangle$ denotes the ensemble average, the asterisk denotes the complex conjugate and $\perp$ denotes the plane perpendicular to the magnetic field. The velocity $\vec{u}_\perp$ is the $\vec{\mathrm{E}}\times\vec{\mathrm{B}}$ velocity defined as $\vec{u}_\perp \equiv \hat{z}\times\nabla_\perp\phi$, and $f \equiv f_1 + f_2$. A positive (negative) $T_n(f,f_1)$ or $T_u(f,f_1)$ means that fluctuations at the frequency f gain (lose) energy from (to) frequencies f_1 and f_2 through 3-wave coupling. In order to determine these two terms, the plasma density fluctuations $\tilde{n}$ and their first derivative $\nabla_\perp\tilde{n}$ as well as the potential fluctuations $\tilde{\phi}$ and their first and second derivatives $\nabla_\perp\tilde{\phi}$ and $\nabla_\perp^2\tilde{\phi}$ need to be experimentally measured. These measurements were performed with a dual 3x3 probe array centered at the same radial location [1]. These quantities were then Fourier transformed into the frequency domain to compute the corresponding convolutions and finally ensemble-averaged over a sufficient number of realizations to reach statistically converged bispectra.

The dual 3x3 Langmuir probe array, described in detail in Chapters 2 and 3, was installed at z=75 cm (here z=0 is defined as the interface between the source belljar and the vacuum chamber). The output analog signals from the probe array are simultaneously sampled and stored at a high time resolution (500 kHz). The measurement circuits have sufficiently high bandwidth such that for the drift turbulence signals (< 25 kHz) the phase shifts introduced by the signal conditioning circuits are negligibly small ($< 0.5^{\circ}$). The 3x3 array for density channels and the 3x3 array for potential channels were centered at the same spatial point in both azimuthal and radial directions, but shifted by 1.5 mm along the magnetic field line. Since the turbulent correlation length along magnetic field line is much larger than 1.5 mm, the resulting phase shifts are also negligible. The machine runs in a steady state, which makes the measurement of long time sequences possible to achieve statistically converged bispectra.

5.3 Experimental results

For convenience the basic profiles such as plasma density, potential, particle flux, etc. for the CSDX plasma have been reproduced here in figure 5.1. For more details about how these profiles were obtained, the reader is referred to previous work from the CSDX device [17].

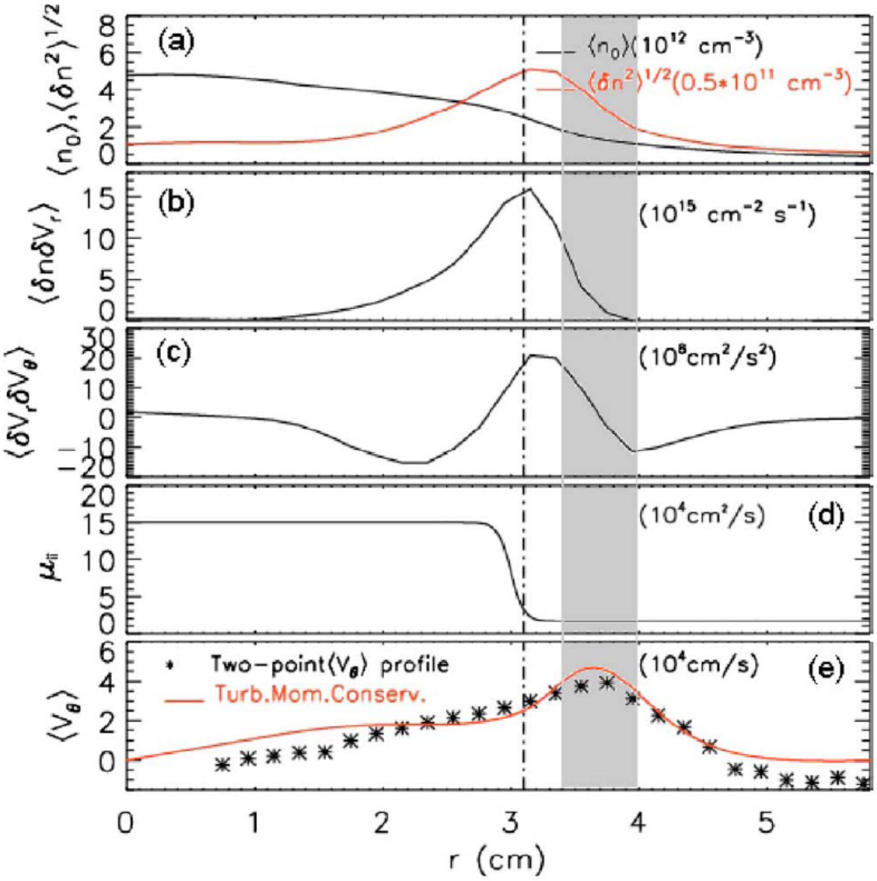

Figure 5.1 Equilibrium radial profiles for CSDX. (a) Time-averaged density (solid black) and RMS of density fluctuation (solid red). (b) Time-averaged turbulent particle flux. (c) Time-averaged Reynolds Stress. (d) Estimated ion viscosity. (e) Plasma azimuthal velocity [17].

The results shown in this chapter were measured at the plasma discharge condition: argon fill gas with a pressure 3.2 mtorr, magnetic field strength of 1000 Gauss and RF power 1.5 kW with reflected power less than 20 W, in order to allow direct comparison with previously published time domain results [2, 3, 10, 17, 18]. As we can see from the spectra in figures 5.2 (a) through 5.2(c), the plasma at this condition is in a weak turbulent state, in which the fluctuations have a significant degree of frequency broadening but still reasonably follow the linear dispersion relation (see figures 5.6 (a) and 5.6 (b)), with coherent modes coexisting with broadband turbulent fluctuations. Both the density and potential spectra peak at around 5 kHz and 10 kHz, which have been identified as m>0 collisional drift waves [9]. The potential and azimuthal velocity spectra also exhibit peaks at very low frequencies ($\leq 1 \sim 2$ kHz). These low frequency fluctuations have been associated with the slow evolution of the m=0 radially sheared flows [10]. The spectra of density and potential fluctuations are significantly different, particularly at frequencies of 2.5kHz and below, and their cross correlation is significantly less than unity [1].

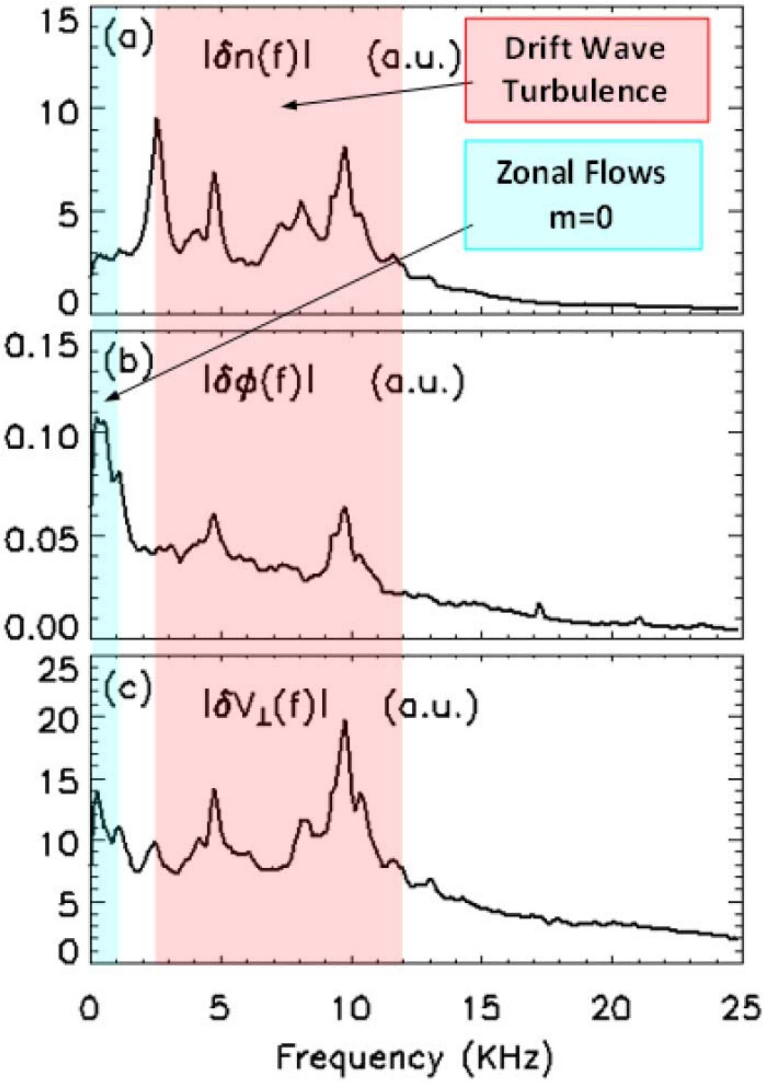

Figure 5.2 Typical autospectra (a) density, (b) potential, and (c) perpendicular velocity for the weakly turbulent plasmas in CSDX. Measurement was taken at argon pressure 3.2 mTorr, magnetic field 1000 Gauss, and RF power 1.5 kW by the dual 3x3 Langmuir probe array centered at the radial position r=3.6 cm.

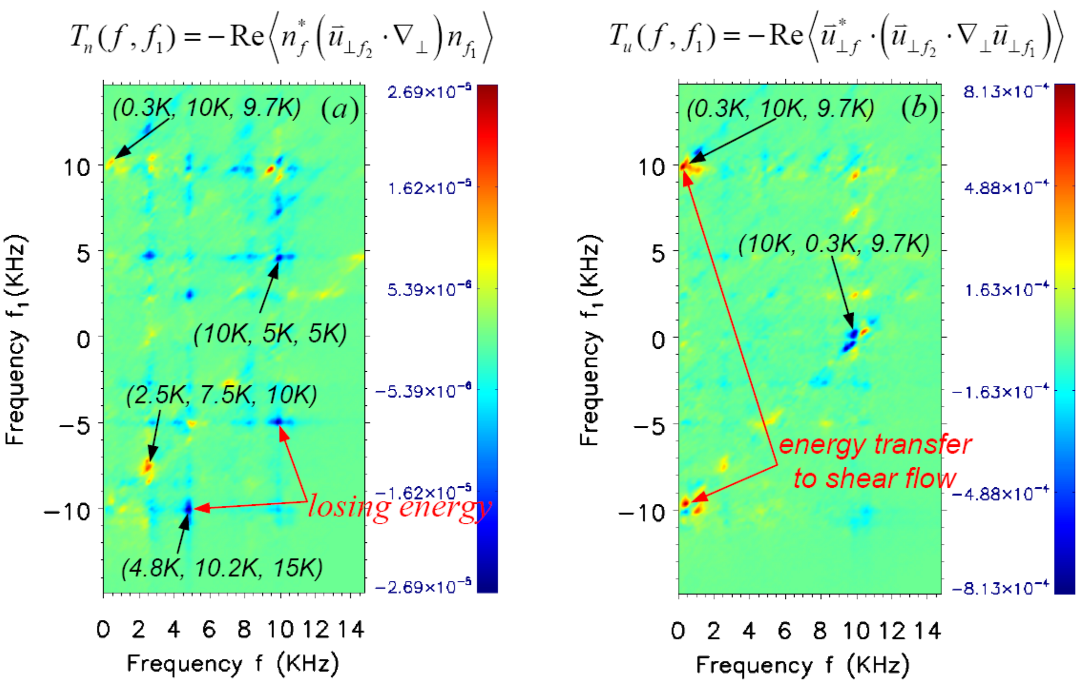

Figure **5.3** The experimentally measured nonlinear energy transfer rates. (a) Internal energy transfer. (b) Kinetic energy transfer [1]. In both figures positive (negative) values correspond to a positive (negative) energy transfer to either density or perpendicular velocity fluctuations. Several prominent frequency triplets (f, f_1, f_2) are highlighted.

The nonlinear internal and kinetic energy transfer rates $T_n(f,f_1)$ and $T_u(f,f_1)$, given by Eq. (5.1) and (5.2), have been measured using the dual 3x3 probe array at argon pressure 3.2 mTorr and magnetic field 1000 Gauss. The probe array was centered at r = 3.6 cm, which lies at the inner radius of the shear layer (Fig 5.1e). About 5 million sampling points on each channel were divided into roughly 1200 independent realizations to perform the bispectral calculation with good frequency resolution ($\Delta f \sim 120Hz$). As has been shown in Chapter 3 and in the literature [1] both $T_n(f,f_1)$ and $T_u(f,f_1)$ will converge once the number of realizations reaches ~ 1000.

For convenience, figures from that earlier chapter showing the 2-dimensional $T_n(f, f_1)$ and $T_u(f, f_1)$ at this discharge condition are reproduced and shown here as figure 5.3, where the positive peak at $f = 0.3\ kHz,\ f_1 = 10\ kHz$ in figure 5.3(b) clearly indicates that slowly varying zonal flows are coupled to drift wave turbulence and gain kinetic energy from ~ 10 kHz drift wave turbulences through 3-wave coupling.

If we sum $T_n(f, f_1)$ over the frequency f_1, we find the net internal energy transfer rate for the frequency f, i.e. $T_n(f) = \sum_{f_1} T_n(f, f_1)$, which gives the total net internal energy transfer into (or out of) frequency f from all other frequencies. Figures 5.4(a) and 5.4(b) show the net internal energy transfer and the net kinetic energy transfer respectively computed in this manner. Here a negative value means that frequency f is losing energy and a positive value means that it is gaining energy. We can clearly see that the drift turbulence region (which corresponds to several kHz to ~ 12 kHz [9]) loses internal and kinetic energy to both low and high frequencies. The large positive peak in the low frequency region (f<2 kHz) in figure 5.4(b), which has been shown to correspond to m=0 zonal flows (see figure 5.2(b)), gain net kinetic energy, while the large negative peak at f ~ 10 kHz shows that fluctuation at this frequency loses kinetic energy. An examination of $T_u(f, f_1)$ in figure 5.3(b) shows that the nonlinear zonal flow drive is dominated by the transfer of energy from these 10 kHz drift fluctuations. It can be inferred that the strongest flow drive comes from $k_\theta \rho_S \approx 1$ fluctuations since the 10 kHz fluctuations can be mapped to an m=3 mode using the experimentally measured dispersion relation shown in figure 5.6(b), and for the m=3 mode $k_\theta = m/r \sim 0.8\ cm^{-1}$ and $\rho_s \sim 1\ cm$.

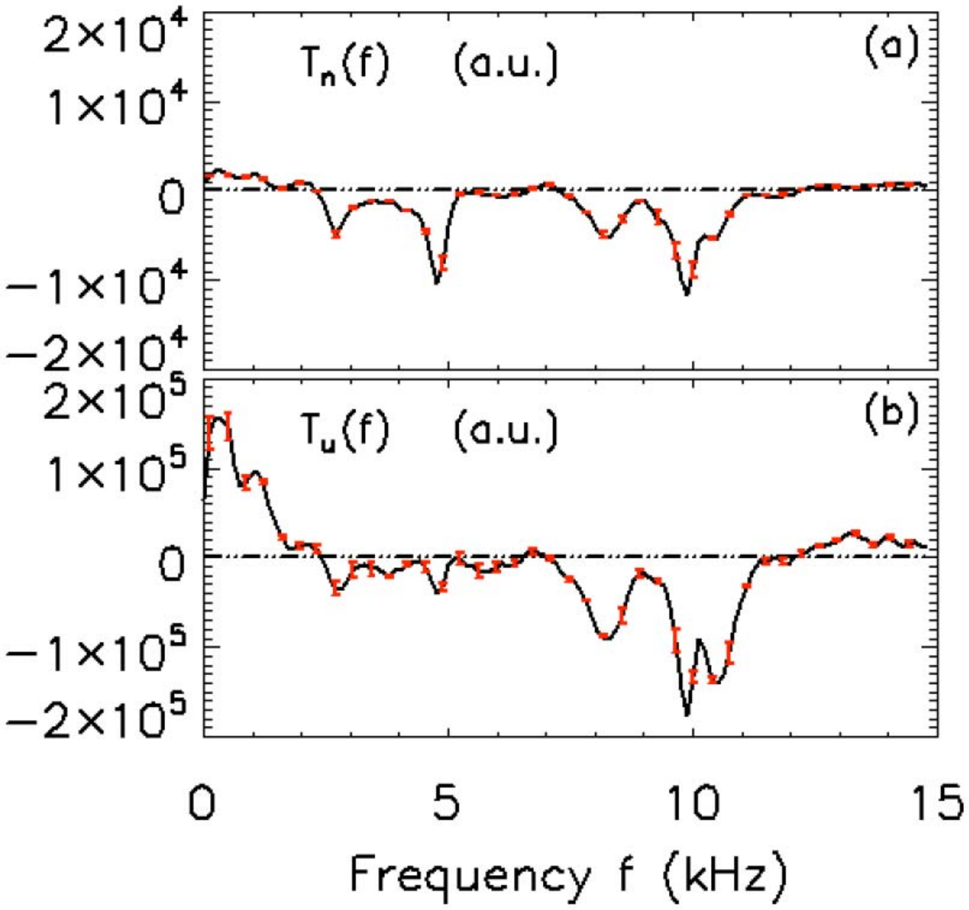

Figure **5.4** Net energy transfer rates (a) internal (b) kinetic. Here a positive value at one specific frequency means that density (or perpendicular velocity) fluctuation at this frequency gains energy, while a negative value means losing energy.

Since the total normalized fluctuation energy in the system can be defined as $E_{total} \equiv |\tilde{n}(f)|^2 + |\tilde{u}_\perp(f)|^2$ and the internal and kinetic energy transfer rates quantitatively indicate the amount of energy redistributed among different frequencies through nonlinear processes, it is useful to sum the internal and kinetic energy transfer rates to get a net rate of the total fluctuation energy transfer, $T_{total}(f) \equiv T_n(f) + T_u(f)$. The bispectral results show that generally the magnitude of kinetic energy transfer rate is at least a factor of 5 bigger than that of the internal energy transfer rate. With figures 5.4(a) and 5.4(b) this means that the total energy transfer rate follows the kinetic energy transfer rate and the bulk of the total fluctuation energy is nonlinearly transferred to low frequency zonal flow region. This could be understood by noting that the total fluctuation energy can be rewritten as $E_{total} \sim \left(\left| \frac{\tilde{n}(r)}{n_0(r)} \right|^2 + k_\perp^2 \rho_s^2 \left| \frac{\tilde{\phi}(r)}{k_B T_{e0}(r)} \right|^2 \right)$ and in our experiment $\rho_s = C_s / \Omega_{ci} \sim 1\ \mathrm{cm}$, implying that the second term on the RHS should dominate if the fluctuation amplitudes of the two fields are comparable. At the shear layer for the m=3 mode $k_\theta = m/r \sim 0.8\ \mathrm{cm}^{-1}$ and $k_r >> k_\theta$ since the measured turbulence correlation length in azimuthal direction is roughly a factor of 3 higher than the turbulence correlation length in radial direction at the shear region [17]. We thus estimate that $k_\perp \rho_s \sim 3$. In our experiment the locally normalized density and potential fluctuations are about the same magnitude, i.e. $\left| \frac{\tilde{n}(r)}{n_0(r)} \right| \sim \left| \frac{\tilde{\phi}(r)}{k_B T_{e0}(r)} \right|$. Combining the above we then find that the kinetic fluctuation energy is roughly a factor of 10 higher than the density fluctuation energy. This is consistent with the measured results showing that the nonlinear kinetic energy transfer rate is much bigger than the internal energy transfer rate.

From Eqns. (5.1) and (5.2), we can see that the internal and kinetic energy transfer terms can both be divided into components. For example $T_u(f, f_1)$ is comprised of 4 different parts $-\mathrm{Re}\left\langle u_{y,f}^* \, u_{x,f_2} \frac{\partial u_{y,f_1}}{\partial x} \right\rangle$, $-\mathrm{Re}\left\langle u_{y,f}^* \, u_{y,f_2} \frac{\partial u_{y,f_1}}{\partial y} \right\rangle$, $-\mathrm{Re}\left\langle u_{x,f}^* \, u_{x,f_2} \frac{\partial u_{y,f_1}}{\partial y} \right\rangle$ and

$-\mathrm{Re}\left\langle u_{x,f}^{*}\ u_{y,f_2}\frac{\partial u_{x,f_1}}{\partial y}\right\rangle$. A similar set of expressions can be written for $T_n(f, f_1)$. By calculating each of these components separately and summing the resulting bispectra over f_1, the contribution from each part to the total net energy transfer rate can be found. The results of this calculation are shown in figures 5.5(a) and 5.5(b). The net internal energy transfer (Fig. 5.5 (a)) shows that the term $-\mathrm{Re}\left\langle n_{f}^{*}\ u_{x,f_2}\frac{\partial n_{f_1}}{\partial x}\right\rangle$ (red dash) closely follows the total internal energy transfer (solid black line), while the term $-\mathrm{Re}\left\langle n_{f}^{*}\ u_{y,f_2}\frac{\partial n_{f_1}}{\partial y}\right\rangle$ (blue dot) is much smaller. We therefore conclude that the term $-\mathrm{Re}\left\langle n_{f}^{*}\ u_{x,f_2}\frac{\partial n_{f_1}}{\partial x}\right\rangle$ (corresponding to a radially directed $\vec{\mathrm{E}}\times\vec{\mathrm{B}}$ velocity interacting with a radial density gradient) is the major player for redistributing internal energy among different frequencies via nonlinear wave-wave coupling. This result would seem to make intuitive sense, since the radial density gradient is the dominant source of free energy in the system and is advected by radial motion induced by the drift wave instability.

We can also see in figure 5.5(b) that the term $-\mathrm{Re}\left\langle u_{y,f}^{*}\ u_{x,f_2}\frac{\partial u_{y,f_1}}{\partial x}\right\rangle$ dominates the net kinetic energy transfer. Because $\frac{\partial \tilde{u}_y(t)}{\partial x}$ is the azimuthal flow shearing rate, it is clear that the slowly varying azimuthal velocity oscillations $u_y(f)$ at f=200-300Hz gains energy due to the interaction between $\tilde{u}_x(t)$ at frequency $f_2 = f - f_1$ and the azimuthal shearing rate at frequency f_1. By noting that vorticity can be written as $\nabla_{\perp}^{2}\phi(t)=\frac{\partial^2\phi(t)}{\partial x^2}+\frac{\partial^2\phi(t)}{\partial y^2}$ and that

$\left|\frac{\partial^2\tilde{\phi}(t)}{\partial x^2}\right| >> \left|\frac{\partial^2\tilde{\phi}(t)}{\partial y^2}\right|$ in our experiments, we can take $\frac{\partial^2\tilde{\phi}(t)}{\partial x^2}$ approximately to be vorticity, and hence $\tilde{u}_x(t)\frac{\partial\tilde{u}_y(t)}{\partial x} = \tilde{u}_x(t)\frac{\partial^2\tilde{\phi}(t)}{\partial x^2} \approx \tilde{u}_x(t)\nabla_\perp^2\tilde{\phi}(t)$ is approximately the instantaneous radial flux of vorticity associated with perpendicular velocity fluctuations. This result then suggests that one can also view the shear flow as being generated by a flux of vorticity which accumulates at the shear layer and reinforces or amplifies the shear flow. By noting that, for divergence-free flows such as $\vec{E}\times\vec{B}$ drifts, we can write $\frac{\partial}{\partial x}\left\langle\tilde{u}_x\tilde{u}_y\right\rangle = \left\langle\tilde{u}_x\tilde{\omega}_z\right\rangle$ where $\tilde{\omega}_z \equiv \left(\nabla\times\tilde{u}\right)_z$ is the vorticity of the fluctuating velocity in the x-y plane [19, 20], this interpretation can be seen to be entirely consistent with the results of Holland et al [3] which showed that the time-averaged Reynolds Stress was consistent with the observed shear flow profile and estimated damping processes. The results here therefore suggest that the transient vorticity flux $\tilde{u}_x(t)\frac{\partial^2\tilde{\phi}(t)}{\partial x^2}$ is responsible for the transfer of turbulent energy in frequency space, and specifically is responsible for the transfer of turbulent momentum with higher frequency into the slowly oscillating (i.e. low frequency) shear flows. This result provides a consistent and complementary picture of the fluctuations drive mechanism of shear flows to the earlier time-domain picture which attributes the shear flow drive to an accumulation of turbulent momentum within the shear layer.

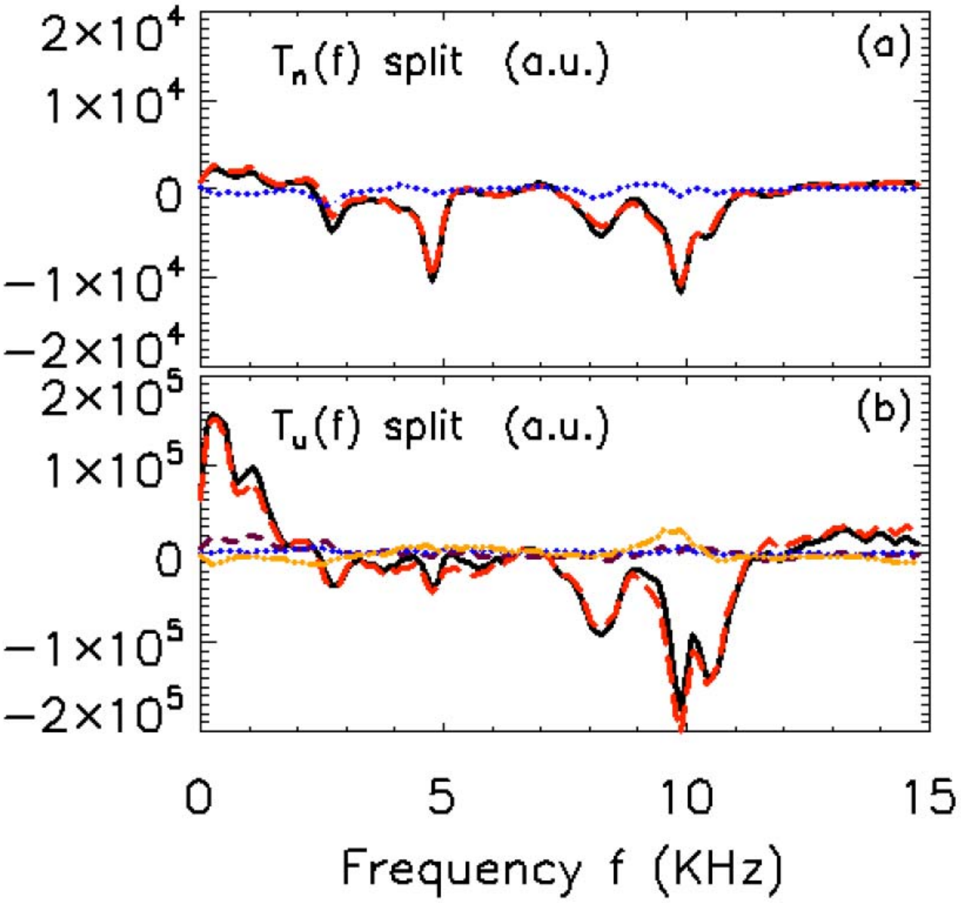

Figure **5.5.** (a) Contributions to the net internal energy transfer rate due to $-\mathrm{Re}\left\langle n_f^* \ u_{x,f_2} \frac{\partial n_{f_1}}{\partial x} \right\rangle$ (red dash) and $-\mathrm{Re}\left\langle n_f^* \ u_{y,f_2} \frac{\partial n_{f_1}}{\partial y} \right\rangle$ (blue dot). The total value is indicated by the solid black line. (b) Contributions to the net kinetic energy transfer rate due to $-\mathrm{Re}\left\langle u_{y,f}^* \ u_{x,f_2} \frac{\partial u_{y,f_1}}{\partial x} \right\rangle$ (red long dash), $-\mathrm{Re}\left\langle u_{y,f}^* \ u_{y,f_2} \frac{\partial u_{y,f_1}}{\partial y} \right\rangle$ (purple short dash), $-\mathrm{Re}\left\langle u_{x,f}^* \ u_{x,f_2} \frac{\partial u_{y,f_1}}{\partial y} \right\rangle$ (blue dot), and $-\mathrm{Re}\left\langle u_{x,f}^* \ u_{y,f_2} \frac{\partial u_{x,f_1}}{\partial y} \right\rangle$ (orange dash dot). The total kinetic energy transfer rate is indicated by the solid black line.

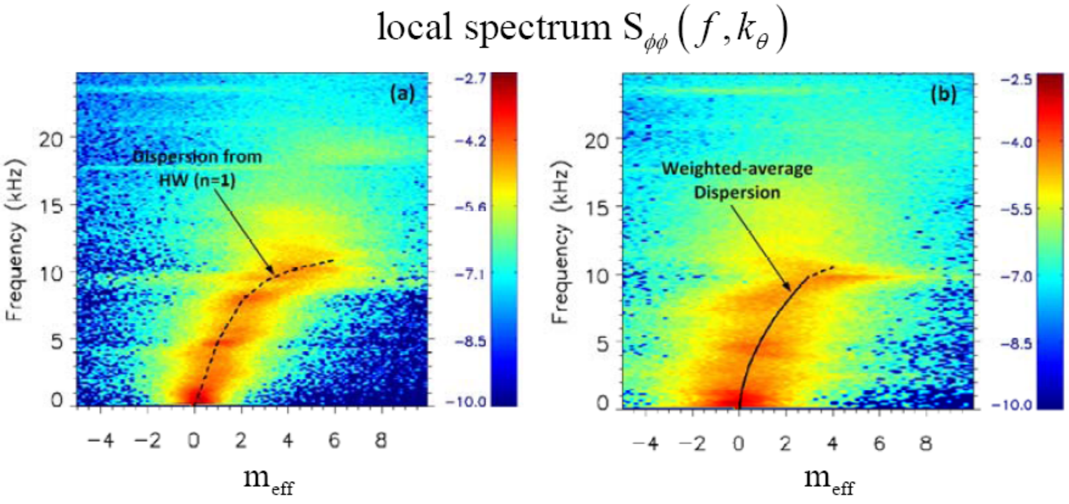

Figure 5.6 Two-point spectrum $S(f,k_\theta)$ from potential (with the intensity in log scale). (a) Dispersion measured at r = 2.6 cm (strong density gradient region) and the black dashed line is for the real part of the linear eigenmode frequencies of the first radial eignemode branch (n=1) calculated from the linear dispersion relation Eq. (5.3) with Doppler shift accounted (using typical CSDX parameters $T_e \sim 2.0\ eV$, $L_n \sim 2.5\ cm$, $a = 10.0\ cm$, $\nu_{i\text{-}n} \sim 6.0\ kHz$ and $\mu_{ii} \sim 2.0\times10^4\ cm^2/s$). The effective azimuthal mode number is a continuous variable defined as $m \equiv k_\theta r$. (b) Dispersion measured at r = 3.6 cm (maximum shear region), and the black solid line indicates the weighted-average values, which were used to map the nonlinear transfer rate in the frequency space into the wavenumber space.

5.4 Linear stability analysis with comparison to experiment

The idea that linearly unstable modes release free energy into finite amplitude fluctuations, and the energy of these fluctuations is then nonlinearly transferred into linearly damped or stable fluctuations is assumed implicitly in nearly all turbulence models of drift turbulence, and yet this model has never received direct experimental scrutiny (see e.g. the Hasegawa-Wakatani collisional drift-wave model [21]). These results do permit us to infer the energy transfer rates, and to compare then against a linear stability analysis and the measured saturated turbulent power spectra in order to determine if the observations are consistent with such an ansatz for the balance of linear release of free energy, nonlinear energy transfer, and damping via linear processes.

We proceed by first assuming that the equilibrium density is of Gaussian form $n_0(r) = n_0 \exp\left(-0.5\left(r/L_n\right)^2\right)$ (which is close to the profile shown in Fig 5.1(a)). Using this profile in the linearized Hasegawa-Wakatani collisional drift turbulence model (thought to be appropriate for this experiment) written in a cylindrical geometry, we find the linear dispersion relation

$$-ik_{mn}^2\omega_{mn}^2 + \left[\omega_{\|}\left(1+k_{mn}^2\right)+\nu_k\right]\omega_{mn} - \omega_{\|}\left(m\frac{\rho_s}{L_n} - i\nu_k\right) = 0 \tag{5.3}$$

Here k_{mn} is the effective radial wavenumber denoted by $k_{mn} = X_{mn}/a$, where X_{mn} is the nth zero of $J_m(x)$ and a is the radius of the plasma cylinder. $\omega_{\|} = k_{\|}^2 v_{Te}^2/\nu_{ei}$ is the parallel electron adiabatic parameter (assumed constant here) and $\nu_k = \left(\nu_{i-n} + \mu_{ii}k_{mn}^2\right)k_{mn}^2$ is a dimensionless measure of perpendicular dissipation due to the combined effect of the ion-neutral collision frequency ν_{i-n} and the ion-ion collisional viscosity. More details about this calculation can be found elsewhere [22]. By using typical CSDX parameters for the 1000 Gauss case with an average electron temperature $T_e \sim 2.0\ eV$, density gradient scale length $L_n \sim 2.5\ cm$, plasma radius $a = 10.0\ cm$, an average ion neutral collision rate $\nu_{i\text{-}n} \sim 6.0\ kHz$, and an average ion collisional viscosity $\mu_{ii} \sim 2.0\times10^4\ cm^2/s$ [3], we can solve the complex eigenfrequencies ω_{mn} from the linear dispersion relation and thus find the real frequencies and the growth rates for each eigenmode. The Doppler shift introduced by the mean $\vec{\mathrm{E}}\times\vec{\mathrm{B}}$ flow associated with the azimuthal flow has been taken into account by adding a frequency shift given by $k_\theta \langle V\rangle_\theta$, where the value of $\langle V_\theta\rangle$ measured by a Mach probe [18] was used. This Doppler shifted frequency ω_{mn} (real part) for n=1 is shown as the black dashed line in figure 5.6(a). Note that in these figures the effective azimuthal modenumber, m_{eff}, is a continuous variable defined as $m_{eff} = k_\theta r$.

By using two azimuthally separated Langmuir probes, the spectrum $S(f, k_\theta)$ can be measured and a mapping between frequencies and azimuthal mode numbers can be established [23]. Figure 5.6(a) shows the two-point k-spectrum measured at r = 2.6 cm at the strong density gradient region, where the x-axis is the azimuthal mode number and the y-axis is frequency. Figure 5.6(b) is the dispersion relation measured at r = 3.6 cm at the maximum shear region. We can see that the spectrum exhibits strong dispersion for $m \geq 3$, and several azimuthal mode numbers $m \sim 3-6$ are degenerate with frequency f ~ 10 kHz. It is interesting to note that the strong nonlinear interaction of these degenerate fluctuations is what leads to the very low frequency ($f \sim 200-300\ \mathrm{Hz}$) m=0 sheared flow fluctuation (shown in Fig. 5.2); this observation may be the m=0 limit of the more general nonlinear convective cell generation mechanism discussed by Shukla [24].

With the experimentally measured k-spectrum in figure 5.6 (b), we can now map the measured energy transfer rates from the frequency domain to the azimuthal wavenumber domain. To do this, for each frequency a weighted-average value $\overline{k}_\theta(f) \equiv \int_0^\infty S(f,k_\theta)k_\theta dk_\theta / \int_0^\infty S(f,k_\theta)dk_\theta$ was obtained by averaging over the two-point spectrum in figure 5.6(b), then those values for different frequencies were smoothed to get the black solid line in Fig. 5.6(b). The resulting effective curve $F\left(\overline{\mathrm{k}}_\theta\right)$ was used to map the net energy transfer rates into the wavenumber domain. Figure 5.7(a) shows the mapped kinetic energy transfer rate $T_u\left(\overline{k}_\theta(f)\right)$ by the red solid curve and the mapped internal energy transfer rate $T_n\left(\overline{k}_\theta(f)\right)$ by the blue dashed line. The results show that the zonal flow (m ~ 0 mode) gains net kinetic energy while fluctuations with m = 1, 2, 3 etc.lose kinetic energy. The mapping for $m \geq 4$ has large uncertainties when the mapping frequencies approach ~ 10 kHz due to the frequency degeneracy seen in figure 5.6 (b). However it is still very clear from figure 5.6 (b) that the major zonal flow driving frequency range 9 ~ 11 kHz corresponds to azimuthal modes $\mathrm{m} \geq 3$, implying that the kinetic energy carried by fluctuations with higher azimuthal wavenumber is nonlinearly transferred to m ~ 0 mode where it is (presumably) damped away through collisional processes. The driving source for those waves with higher azimuthal mode numbers still needs to be identified. As we show next, the m=1 ~ 10 modes are linearly unstable thus they can tap energy directly from density gradient; in addition they can interact nonlinearly with each other to re-arrange the energy spectrum.

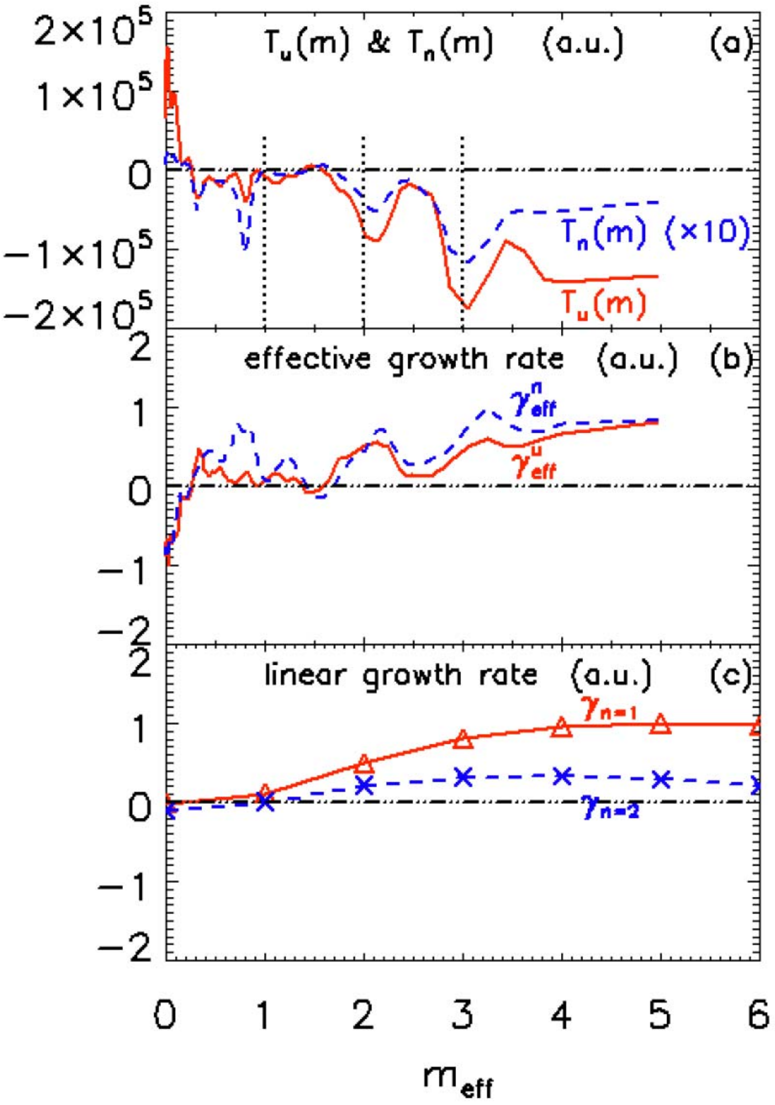

Figure **5.7** (a) Nonlinear energy transfer rates mapped from frequency domain to wavenumber domain using the experimentally measured k-spectrum $S(f, k_\theta)$ presented in figure 5.6(b). The red solid line is for $T_u(m)$ and the blue dashed line is for $T_n(m)$. (b) Effective growth rates inferred from the nonlinear net energy transfer rates. The red solid line is for γ^u_{eff} and the blue dash line is for γ^n_{eff}. (c) Linear growth rates from Hasegawa-wakatani model. The red solid line is the growth rate of the first linear radial eigenmode n=1, $\gamma_{n=1}$, and the blue dashed line is for the second radial eigenmode n = 2, $\gamma_{n=2}$.

In figure 5.6(a) the real parts of the linear eigenfrequencies for the first radial eigenmode were plotted as the black dashed line, which agrees well with the experimentally measured k-spectrum. The imaginary parts of the linear eigenfrequencies (i.e. the linear growth rates) for the first and second radial eigenmodes computed from this linear stability analysis are plotted in figure 5.7(c). We find that the $m \geq 1$ modes on the n=1 and n=2 branches are both linearly unstable. Furthermore, we note that the unstable (stable) regions correspond to the regions where $T_u < 0$ ($T_u > 0$), consistent with expectations for a stationary spectrum established by balancing the linear growth/decay against the nonlinear energy transfer. To test the consistency of this spectrum balance picture, we can lump the linear effects into an effective linear growth/damping rate, γ_{eff}^{u}, and rewrite the frequency-domain kinetic energy transport equation (see Ref 1) as:

$$\left\langle \frac{1}{2}\frac{\partial\left|\tilde{u}_{\perp f}\right|^2}{\partial t}\right\rangle = T_u(f) + \gamma_{eff}^{u}(f)\left\langle |\tilde{u}_{\perp f}|^2\right\rangle \tag{5.4}$$

For a time stationary plasma the left-hand side of the equation (5.4) is zero. By dividing the equation by $\left\langle |\tilde{u}_{\perp f}|^2\right\rangle$ we can infer an effective linear growth/damp rate as $\gamma_{eff}^{u}(f) \equiv -\frac{T_u(f)}{\left\langle |\tilde{u}_{\perp f}|^2\right\rangle}$, which can be compared with the analytically calculated linear grow rate from equation (5.3). The red solid line in figure 5.7(b) shows the result. We note that the sign of γ_{eff}^{u} agrees with the linear stability analysis, and the relative magnitudes of the unstable region, where $\gamma_{eff}^{u} > 0$ and where both $\gamma_{n=1} > 0$ and $\gamma_{n=2} > 0$, is in rough agreement. However, we also note that γ_{eff}^{u} for $m_{eff} \approx 0$ is significantly more negative than $\gamma_{n=1}$ and $\gamma_{n=2}$ at $m_{eff} \approx 0$. This result, which is found by balancing the time-averaged zonal flow amplitude against the nonlinear energy transfer into the zonal flow, suggests that some additional damping mechanism (e.g. a shear flow instability unrelated to the damping mechanism that are contained in the linear stability analysis) may influence the zonal flow saturation. Additional work is required to determine if this is indeed the case.

5.5 Summary and discussion

We have shown in this chapter that the directly measured nonlinear energy transfer rates for both velocity and density fluctuations are negative at intermediate frequencies and positive in both low and high frequency regions, indicating that turbulent energy is nonlinearly transferred to low frequency zonal flows and to regions at higher frequencies, where the energy is then presumably dissipated. In addition, we find that the radial flux of vorticity, equivalent to gradient of the turbulent Reynolds stress, is dominantly responsible for redistributing turbulent kinetic energy among different frequencies (or different scales). Thus the vorticity flux can be thought of as having two equivalent roles: it leads to the transport of momentum in configuration space and to the spreading of energy among different spatiotemporal scales in the Fourier domain.

We also compared the net nonlinear transfer results against a linear eigenmode calculation based on the Hasegawa-Wakatani model. Despite the use of very simplified profiles (flat electron temperature, ion viscosity profiles, etc.), the comparison shows that the linearly unstable fluctuations correspond to the regions where the nonlinear transfer leads to a loss of energy. Conversely, the linearly stable fluctuations correspond to regions that receive nonlinearly transferred energy. Linear analysis also shows that $m \geq 1$ modes of the first two radial eigenmodes n=1 and n=2 are unstable at the typical CSDX condition, suggesting that these two radial eigenmodes could play a role in driving the zonal flows.

The observation that zonal flows are driven predominantly by the radial flux of vorticity, combined with the observation that the shear layer is spatially separated from the strong gradient region (which presumably is where drift fluctuations originate) suggests a picture where drift fluctuations with finite vorticity are generated at one location and then propagate outward and then interact with and reinforce a pre-existing shear layer. In the next chapter we use direct visualization of the fluctuations to obtain a deeper understanding of this result.

All the contents in the next chapter, including text and data, has been submitted for publication as it appears in “Generation of a Sheared Plasma Rotation by Emission, Propagation and Absorption of Drift Wave Packets”, M. Xu, G. R. Tynan, P. H. Diamond, S. H. Muller, C. Holland, J. Yu , Z. Yan, Phys. Rev. Lett. (2010). The dissertation author is the primary investigator and author of this article.

References:

[1] M. Xu, G. R. Tynan, C. Holland, Z. Yan, S. H. Muller, J. H. Yu, Phys. Plasmas **16** 042312 (2009)

[2] G. R. Tynan, C. Holland, J. H. Yu, A. James, D. Nishijima, M. Shimada, and N. Taheri , Plasma Phys. Control. Fusion **48** S51-S73 (2006)

[3] C. Holland, J. H. Yu, A. James, D. Nishijima, M. Shimada, N. Taheri and G. R. Tynan, Phys. Rev. Lett. **96** 195002 (2006)

[4] J. S. Kim, R. D. Durst, R. J. Fonck, E. Fernandez, A. Ware, and P. W. Terry, Phys. Plasmas **3** (11) 3998-4009 (1996)

[5] S. J. Camargo, D. Biskamp and B. D. Scott, Phys. Plasmas **2** 48 (1995)

[6] P Manz, M Ramisch, U Stroth, Plasma Phys. Control. Fusion **51** 035008 (2009)

[7] C. Hidalgo, C. Silva, M. A. Pedrosa, E. Sanchez, H. Fernandes, and C. A. F. Verandas, Phys. Rev. Lett. **83**, 2203 (1999)

[8] C. P. Ritz, E. J. Powers, and R. D. Bengtson, Phys. Fluids **B 1** (1) 153-163 (1989)

[9] Burin M J, Tynan G R, Antar G Y, Crocker N A and Holland C, Phys. Plasmas **12** 052320 (2005)

[10] Z. Yan, G. R. Tynan, C. Holland, M. Xu, S. H. Muller, J. H. Yu, Phys. Plasmas **17** 032302 (2010)

[11] G. R. Tynan, A. Fujisawa and G. Mckee, Plasma Phys. Control. Fusion **51**, 113001 (2009)

[12] P.H. Diamond, C.J. McDevitt, Ö.D. Gürcan, T.S. Hahm, W. X. Wang, E.S. Yoon, I. Holod, Z. Lin, V. Naulin and R. Singh, *Nucl. Fusion* **49** 045002 (2009)

[13] C. Hidalgo, B. Gonçalves, C. Silva, M. A. Pedrosa, K. Erents, M. Hron, and G. F. Matthews, Phys. Rev. Lett. **91**, 065001 (2003)

[14] P. H. Diamond, S. I. Itoh, K. Itoh, and T. S. Hahm, Plasma Phys. Control. Fusion **47** R35-R161 (2005)

[15] A. Fujisawa, K. Itoh, H. Iguchi, K. Matsuoka, S. Okamura, A. Shimizu, T. Minami, Y. Yoshimura, K. Nagaoka, C. Takahashi, M. Kojima, H. Nakano, S. Ohsima, S. Nishimura, M. Isobe, C. Suzuki, T Akiyama, K. Ida, K. Toi, S.-I. Itoh, and P. H. Diamond, Phys. Rev. Lett. **93**, 165002 (2004)

[16] A. Fujisawa, K. Itoh, A. Shimizu, H. Nakano, S. Ohshima, H. Iguchi, K. Matsuoka, S. Okamura, T. Minami, Y. Yoshimura, K. Nagaoka, K. Ida, K. Toi, C. Takahashi, M. Kojima, S. Nishimura, M. Isobe, C. Suzuki, T. Akiyama, Y. Nagashima, S.-I. Itoh, and P. H. Diamond, Phys. Rev. Lett. **98**, 165001 (2007)

[17] Z. Yan, J. H. Yu, C. Holland, M. Xu, S. H. Muller, and G. R. Tynan, Phys. Plasmas **15** 092309 (2008)

[18] J. H. Yu, C. Holland, G. R. Tynan, G. Antar, and Z. Yan, J. Nucl. Mat, **363-365** 728-732 (2007)

[19] G. I. Taylor, Phil. Trans. Roy. Soc., London A215, 1–26, 1915

[20] P H Diamond, O D Gurcan, T S Hahm, K Miki, Y Kosuga and X Garbet, *Plasma Phys. Control. Fusion* **50** 124018 (2008)

[21] A. Hasegawa and C. G. Maclennan, Phys. Fluids **22** (11) 2122-2129 (1979)

[22] Z. Yan, G. R. Tynan, C. Holland, M. Xu, S. H. Muller, and J. H. Yu, Phys. Plasmas **17** 012302 (2010)

[23] J. M. Beall, Y. C. Kim, and E. J. Powers, J. Appl. Phys. **53**, 3933 (1982)

[24] P. K. Shukla, M. Y. Yu, and K. H. Spatschek, Phys. Rev. A 23, 3247 (1981)

Chapter 6

Generation of a sheared plasma rotation by emission, propagation and absorption of drift wave packets

The generation of intrinsic rotation in toroidally confined plasmas, in which the plasma spontaneously rotates in the toroidal direction without direct toroidal momentum input, has been attributed to the existence of a non-diffusive residual turbulent stress localized to the plasma boundary [1]. Macroscopic measurements in tokamak experiments [2, 3] and recent studies in a linear plasma device [4] provide evidences that such a residual stress does indeed exist at the plasma boundary and plays a role in the generation of intrinsic rotation. However, this earlier work did not identify the operative *microscopic* physics mechanism that leads to the generation of such a stress at the plasma boundary. In this chapter, we show how this residual stress and the associated sheared intrinsic flow are caused by the emission of isotropic turbulent drift vortices from the inner plasma region which spiral outward. As these structures approach the shear layer at the plasma boundary they are stretched azimuthally, become increasingly anisotropic and then are absorbed into the shear layer, thereby transferring their momentum and energy to the shear layer which is consequently amplified. This mechanism is likely to be operative in toroidal confinement devices and also is similar to mechanisms operating in other fluid systems [5], and therefore should be of broad interest.

These experiments were carried out in the Controlled Shear Decorrelation Experiment (CSDX), which is a 2.8 m long linear helicon plasma device. Argon plasmas with an on-axis density ~ 10^{13} cm^{-3} and electron temperature ~3 eV in a 0.1 T magnetic field is produced by a 13.56 MHz half wave-length azimuthally symmetric (i.e. the RF wavefields have azimuthal mode number m=0) helicon source with a radius r_{src}=4.5cm and 1.5kW RF power input (reflected power less than 30 W) and a gas fill pressure of 3.2 mTorr. The exit plane of the source defines the axial position z=0 cm. Doppler broadened central-chord line-averaged argon ion and neutral gas temperatures are ~0.7 and ~0.5 eV respectively. Details of the apparatus and earlier physics results can be found in the literature [6-14].

Heat input from the RF source sustains a centrally peaked plasma density (Fig. 6.1(a)) and electron temperature profile [7] (not shown here), thus driving an electron pressure gradient in the region r<5cm, with a peak density gradient located at r=3cm (Fig. 6.1(b)). A time-averaged azimuthally symmetric sheared azimuthal flow, $\langle v_\theta \rangle$, exists [15] (Fig. 6.1(c)), and is consistent with the measured time-averaged turbulent stress and estimated viscous and ion-neutral flow damping [8], thus satisfying the essential criteria for a turbulence-driven sheared zonal flow. This drift is dominated by a plasma fluid flow in the electron diamagnetic drift direction [15] and has a negative vorticity, $\omega_{ZF} = \nabla_r \langle v_\theta \rangle = \left\langle V_E{}' \right\rangle < 0$ in the shear layer at r=3.5-4cm. The plasma column maintains this intrinsic rotation by the combined action of turbulent stresses and a no-slip boundary condition due to ion-neutral drag [4]. We also note that the peak density gradient occurs slightly inside the shear layer.

The sheared flow grows over a few msec period [12] and then undergoes a more rapid (100's of $\mu\mathrm{sec}$) collapse when a plasma blob is ejected into the region r>5cm [17]. During the shear flow growth phase, the turbulence is characterized by fluctuations with azimuthal wavenumber $k_\theta \geq 1cm^{-1}$, corresponding to an effective azimuthal mode number $m_{eff} \equiv k_\theta r \geq 3$ for *r=3 cm* with a frequency $f \geq 6kHz$ [12], while during the collapse phase the central plasma fluctuations are dominated by a global m=1 oscillation with f~2-4kHz. Since in this chapter we are focused on the generation mechanism of the shear flow, we apply a non-recursive finite impulse response (FIR) high-pass digital filter using a Kaiser window to the imaging and probe fluctuation data. This gives an amplitude suppression ratio >5 within 1 kHz of the 5 kHz cutoff frequency and a ratio as high as 10^6 with sufficient frequency width [18], and thereby isolates the growth phase of the sheared flow.

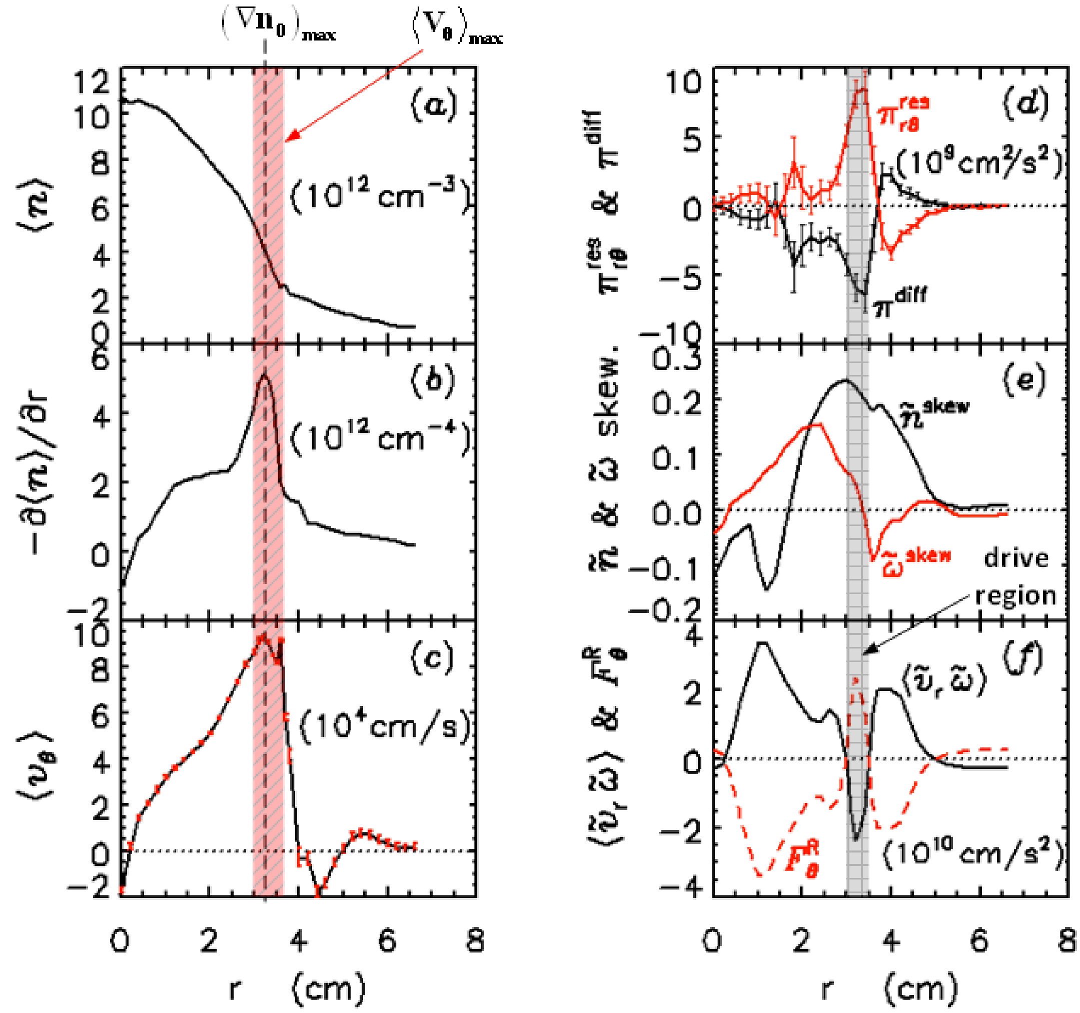

Figure 6.1: Time averaged radial profiles of the CSDX plasma. (a) Time-averaged Density n_0. (b) Gradient of the time-averaged density $-\partial n_0 / \partial r$. (c) Time-averaged azimuthal velocity $\langle V_\theta \rangle$ (d) Residual stress $\pi_{r\theta}^{res}$ (solid red) and the diffusive momentum flux $\pi^{diff} \equiv -\langle \tilde{v}_r^2 \rangle \tau_c \frac{\partial \langle V_\theta \rangle}{\partial r}$ (solid black). (e) Skewness of density (solid black) and vorticity (solid red) fluctuations. (f) Time-averaged radial flux of vorticity $\langle \tilde{v}_r \tilde{\omega} \rangle$ (solid black) and Reynolds force, F_θ^R due to turbulent vorcicity (dashed red).

A 28 cm diameter f/10 telescope coupled to a digital fast-framing (100,000 frames/sec) camera located ~8m away from the object focal plane located at z=75 cm provides a view with viewing sightlines aligned within +/-0.7 deg of the magnetic field lines. The camera detects visible light intensity fluctuations $\tilde{I}_{vis}$ (due primarily to neutral argon emission) as shown in Fig. 6.2. These $\tilde{I}_{vis}$ fluctuations have been shown to be correlated with I_{sat} Langmuir probe fluctuations [19] caused primarily by plasma density fluctuations. The initially isotropic m~3 structures with frequency $f \geq 6kHz$ are born between the plasma center and the maximum density gradient at r~3cm, and propagate primarily in the electron diamagnetic drift direction. We directly measured the nonlinear kinetic energy transfer term $T_u(f) = -\mathrm{Re}\sum_{f_1} \tilde{u}_f \cdot \left(\tilde{u}_{f-f_1} \cdot \nabla \tilde{u}_{f_1}\right)$ with a 3x3 probe array [13] located at z=75cm and centered at r ~2 cm, and then mapped these frequency domain results into the k_θ domain using the measured dispersion relation $k_\theta(f)$ [14]. The result, $T_u(k_\theta)$, is shown in Fig. 6.3 (a) (dotted blue line), and indicates that the m~3 structures born at r=2-3cm are generated by the nonlinear transfer of kinetic energy from other spatial scales with m>0 into the m=3 structures. We therefore conclude that these fluctuations are nonlinearly pumped drift turbulence structures or wave packets.

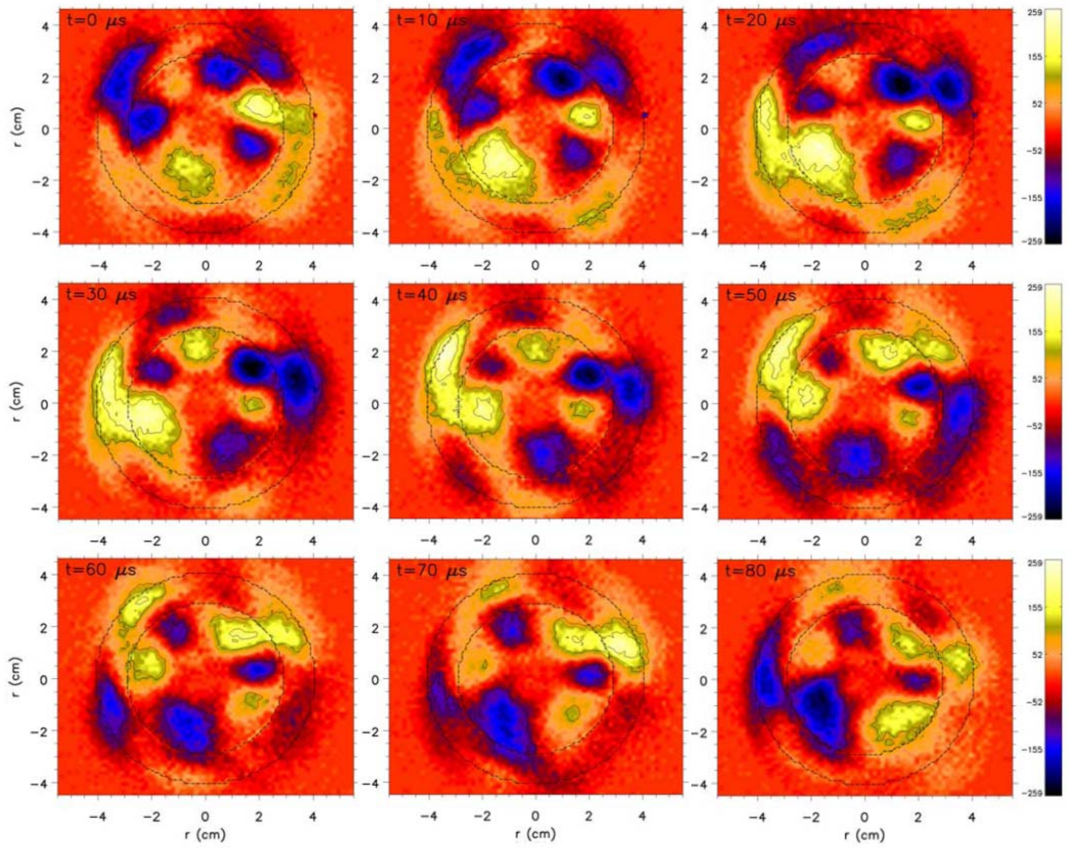

Figure 6.2 Sequential visible light emissions images showing the birth, evolution, and death of vortex-like structures. Radii of r = 3.0 cm and r = 4.0 cm are denoted by the two dashed circles.

Since these structures have correlated density $\tilde{n}$ and potential $\tilde{\phi}$ fluctuations [7], and since the resulting vorticity fluctuations $\tilde{\omega} \equiv \nabla \times \tilde{v}_E$ (where $\tilde{v}_E \equiv \frac{\vec{B} \times \nabla \tilde{\varphi}}{B^2}$ is the fluctuating electrostatic ExB velocity) are given by $\tilde{\omega} \equiv \frac{1}{B} \nabla^2 \tilde{\phi}$, the vorticity fluctuations should be correlated with density fluctuations as expected from the Hasagawa-Wakatani model of collisional drift turbulence, and should have $\frac{d}{dt}\left(\ln n_0 + \frac{\tilde{n}}{n_0} - \frac{e\rho_S^2}{kT_e} \nabla^2 \tilde{\phi} \right) = 0$ in the limit of vanishing cross-field collisional diffusion so that the total potential vorticity

$q \equiv \ln n_0 + \frac{\tilde{n}}{n_0} - \frac{e\rho_S^2}{kT_e}\nabla^2\tilde{\phi} = const$ is an inviscid invariant along fluid trajectories. Here, n_0 varies slowly in time as compared to fluctuating quantities, therefore $q \approx \tilde{q} = const$. Simultaneous measurements of $\tilde{I}_{sat}$ and $\tilde{\omega}$ with the 3x3 probe array [13] show that this is indeed the case (Fig. 6.3 (b) and 6.3(c)) and that the vorticity has roughly a zero time delay with respect to the density fluctuations, suggesting that indeed $\tilde{q}$ is conserved in this region. We can therefore conclude that the fast imaging also reveals the birth, evolution, motion and death of structures with correlated positive and negative density and vorticity fluctuations.

Examining Fig. 6.2 carefully, we also observe that the structure motion contains an outward radial component in addition to the azimuthal component, and thus the structures gradually move outwards in a spiral-shaped trajectory. As the structures approach the shear layer located at r=3.5cm (which is within the region between the two circles shown in each panel of Fig. 6.2) their radial propagation slows as they undergo a "tilt-stretch-absorption" process (TSA). In the course of this their radial correlation length is reduced [10]. They tilt and become increasingly anisotropic and ultimately are absorbed by the shear layer. This TSA behavior is reminiscent of the Howard-Krishnamurti process [5] by which a series of two dimensional convective rolls tilt, stretch and then merge to form a larger scale eddy; the difference here is that a smaller scale eddy or structure is interacting with a pre-existing larger scale m=0 sheared flow. Eddies also occasionally breakup into several smaller scaled eddies.

Probe measurements show that the I_{sat} skewness (Fig. 6.1(e) solid black) changes sign near *r=2cm*, suggesting that the turbulent radial velocity fluctuations give rise to outward (inward) going positive (negative) density perturbations which modulate the density gradient in this region and drive outward particle transport, consistent with previous turbulent particle flux measurements [7]. The vorticity fluctuation skewness is positive in the region between 0<r<3.5cm and is peaked near r=2cm (figure 6.1(e) solid red), indicating that an excess of positive vorticity events occur in the region where the positive density events are born. Correlated measurements of $\tilde{v}_r(t) = -\frac{\nabla_\theta \tilde{\phi}_f(t)}{B}$ and $\tilde{\omega}(t)$ from the 3x3 probe array show a positive flux of vorticity, $\langle \tilde{v}_r \tilde{\omega} \rangle$ (figure 6.1(f) solid black). However, examining Fig. 6.1(e-f) in detail, we find that the vorticity skewness and vorticity flux change sign and become negative in the region 3.0<r<3.5cm. The imaging results (Fig. 6.2) show that the structures, which have vorticity associated with them, are still moving outwards (albeit at a slower rate) and therefore have on average $\tilde{v}_r > 0$ in this region. We can therefore infer that, on average, the sign of the vorticity of the structures is changed in this region. Noting that the m=0 flow shearing rate $\nabla_r \langle v_\theta \rangle = \omega_{ZF} \approx \omega_{sh} \approx -8 \times 10^4 \sec^{-1} < 0$ as discussed above and estimating that $\tilde{\omega} \approx \tau_{eddy}^{-1} \approx \frac{\tilde{\phi}}{BL_\perp^2} \approx 1 - 6 \times 10^4 \sec^{-1}$ for the observed rms floating potential fluctuation amplitude $\tilde{\phi}_f \approx 0.3 - 0.6V$ and perpendicular structure scale length $L_\perp \approx 1 - 2cm$, we find that $|\omega_{ZF}| > |\tilde{\omega}|$. Here τ_{eddy}^{-1} is the eddy rotation rate. Hence a crude estimate based on the Okubo, McWillaims, Weiss criteria [20] for evolution of the local vorticity gradient, namely $\partial_t \nabla \omega \propto \left(V'^2 - \omega^2\right)^{1/2}$, suggests that $\partial_t \nabla \omega > 0$ near the shear layer, where $V' > \omega \sim \frac{1}{\tau_{eddy}}$ as noted above. This steepening of the vorticity gradient drives a forward enstrophy transfer to small scales, which effectively then peels apart the eddy. Thus when the weaker (i.e. $\left|\omega_{ZF}\right| > \left|\tilde{\omega}\right|$) small-scale positive vorticity structure encounters the large-scale shear layer with strong negative vorticity, a progressive merging process occurs during which the outer layers of the smaller structure are sequentially peeled off , leading to the eventual absorption of the smaller structure by the stronger large scale shear flow. This picture is consistent with the vorticity flux profile (Fig. 6.1(f)) and with recently published results from neutral fluids and plasmas [21, 22]. Small structures with negative vorticity, which are rarer in the central plasma region (Fig. 6.1(e)), will be readily absorbed by the negative vorticity mean shear layer. The net contribution from small structures with positive vorticity and those with negative vorticity results in a transfer of the structure's turbulent kinetic energy into the shear layer as shown by measurements of $T_u(k_\theta)$ at r=3.0-4.0cm (Figure 6.3 (a) solid red curve).

For these ExB dominated turbulent flows which have azimuthally invariant fluctuation statistics, the Taylor identity [23] holds and shows that the vorticity flux is related to the turbulent Reynolds stress and Reynolds force F_θ^R exerted by the fluctuations upon the background plasma by the relation $F_\theta^R = -\nabla_r \left\langle \tilde{v}_r \tilde{v}_\theta \right\rangle = -\left\langle \tilde{v}_r \tilde{\omega} \right\rangle$ [23, 24]. Our previous work shows that for the estimated dissipation profiles, F_θ^R is consistent with the mean shear flow, and that the slow variations in F_θ^R are also consistent with slow changes in the shear flow [12]. Examining Fig. 6.1(f), we find that $\left\langle \tilde{v}_r \tilde{\omega} \right\rangle < 0$ for 3<r<3.5cm and has values consistent with the previously published total Reynolds stress profile. The Reynolds force thus amplifies the shear flow in the plasma boundary region, and is consistent with the global turbulent force balance demonstrated in our earlier work. A cross-correlation analysis between the instantaneous fluctuating vorticity flux at variable positions r<3.6cm and the instantaneous turbulent stress at the shear layer at r=3.6cm shows that an increase in vorticity flux from the central plasma region *precedes* an increase in the turbulent stress at the shear layer maximum (Fig. 6.3 (d-g)).

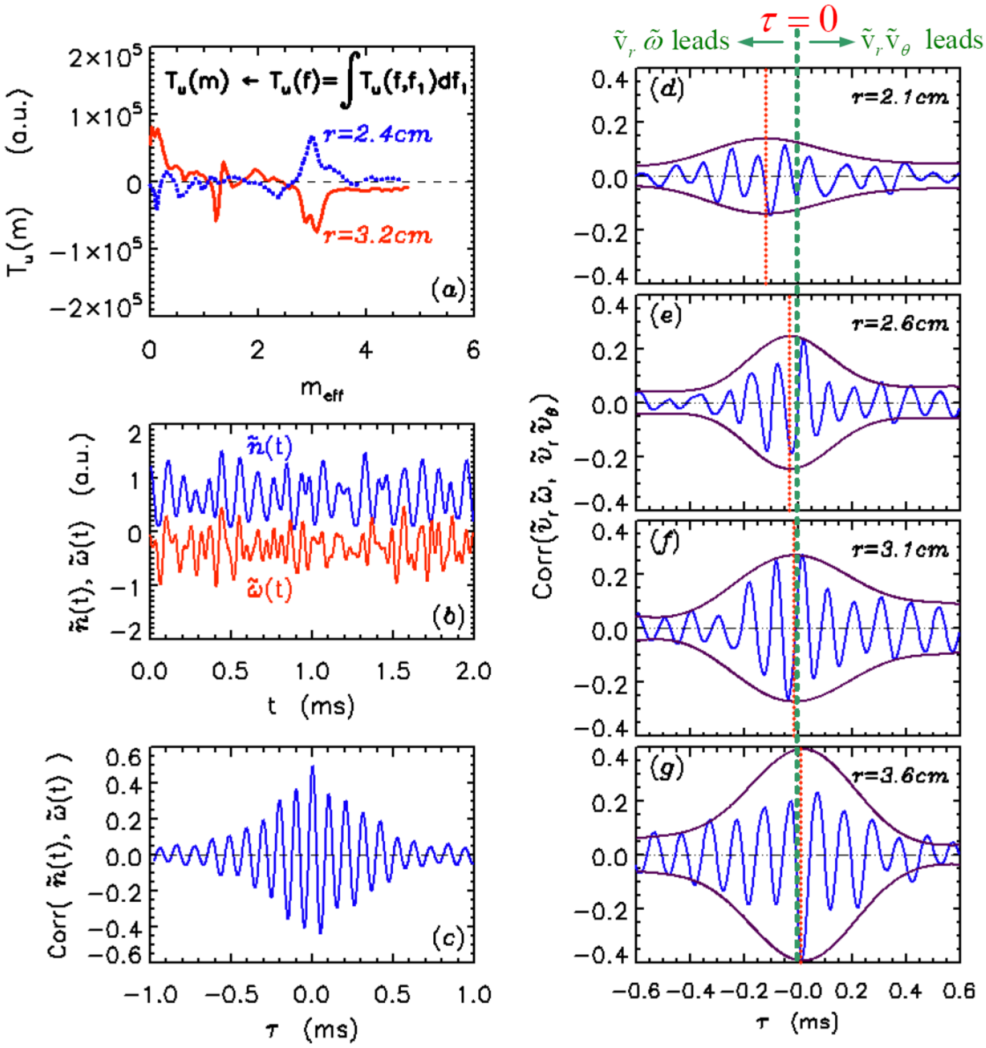

Figure 6.3 (a) Nonlinear kinetic energy transfer vs. effective azimuthal mode number at r=2.4cm (dashed black line) corresponding to the vortex structures generation region and r=3.2cm (solid red line) corresponding to the location of the shear layer. A positive (negative) T_u value indicates a gain (loss) of turbulent kinetic energy through nonlinear processes. The noise level is negligible small as was shown in a former paper [14]. (b) Time resolved density (blue) and vorticity (red) fluctuations. (c) Correlation between density and vorticity fluctuations, which shows that density and vorticity fluctuations have a significant correlation with zero phase shift. (d-g) Cross-correlation between vorticity flux at different radial positions (d-g correspond to r=2.1, 2.6, 3.1, 3,6 cm respectively) and total turbulent stress in the shear layer at r=3.6 cm.

In the above figure an increase in central plasma vorticity flux leads to a subsequent increase in the boundary plasma Reynolds stress ~ 120 microsecond later. Solid blue lines are the calculated correlations. Up-down symmetric envelopes (solid purple line) were computed from the correlations; the center of each envolope is indicated by the dotted red vertical lines. The dotted green line corresponds to zero time delay.

The TSA mechanism may also be understood as a consequence of shear-induced refraction and its impact on wave packet energetics. Since wave packet action density (closely linked to potential enstrophy density) is conserved in a spatio-temporally adiabatic shearing field [25], the wave packet energy density then evolves according to $\frac{d\varepsilon}{dt} = \frac{\partial \omega_k}{\partial k_r} \frac{dk_r}{dt} \frac{\varepsilon}{\omega_k} = -k_\theta v_{gr} \langle V_E' \rangle \varepsilon / \omega_k$ where wave packets obey a dispersion relation ω_k . Since $v_{gr} = -\frac{2 k_r k_\theta \rho_S^2}{1 + k_\perp^2 \rho_S^2} v_*$ and taking $k_r = k_r^{(0)} - k_\theta \left\langle V_E{}' \right\rangle \tau$, this means that $\frac{d\varepsilon}{dt} = \frac{-2 k_\theta^2 \rho_S^2}{\left(1 + k_\perp^2 \rho_S^2\right)} \langle V_E' \rangle^2 \tau_L \varepsilon$ where τ_L denotes the lifetime of the wave packet and we took $\left| k_\theta \left\langle V_E{}' \right\rangle \tau \right| > k_r^{(0)}$ for simplicity. Note that wave packet energy decreases due to shearing, at a rate that is quadratic in the shear strength. As shown elsewhere [25], the total energy is conserved in the course of the straining interaction, so that $\frac{d}{dt}\left(\varepsilon + \langle V_E \rangle^2\right) = 0$ for a suitably normalized shear flow velocity, meaning that flow energy $\langle V_E \rangle^2$ increases at the expense of the wave packet energy. This simple calculation, then, quantifies the intuitive concept of the TSA mechanism, whereby shear flows strain and stretch wave packets, and so ultimately consume their energy. The TSA mechanism may also be viewed as a type of strongly anisotropic inverse cascade, though we emphasize it is not intrinsically statistical.

These results also imply that wave stresses naturally act to amplify sheared flows. This follows simply from the fact that for electrostatic ExB flows $\left\langle \tilde{v}_r \tilde{v}_\theta \right\rangle = \frac{1}{B_0^2} \left\langle k_r k_\theta \left| \tilde{\phi}_k \right|^2 \right\rangle$. So for $k_r = k_r^{(0)} - k_\theta \left\langle V_E{}' \right\rangle \tau$, the shearing breaks symmetry so as to render $\left\langle k_r k_\theta \right\rangle$ unambiguous. Thus $\left\langle \tilde{v}_r \tilde{v}_\theta \right\rangle \approx -k_\theta^2 \rho_S^2 \left\langle \frac{e\tilde{\phi}}{k_B T_e} \right\rangle^2 C_S^2 \left\langle V_E{}' \right\rangle \tau$, and comparison with the discussion above then shows that $\frac{d\varepsilon}{dt} = \left\langle \tilde{v}_r \tilde{v}_\theta \right\rangle \left\langle V_E{}' \right\rangle$, which is clearly equivalent to the Reynolds work performed by the wave stress on the mean shear flow.

Finally, we observe that in toroidal geometry, the TSA realization of the perpendicular stress, $\left\langle \tilde{v}_r \tilde{v}_\perp \right\rangle$, will have a finite toroidal projection, and so may drive intrinsic toroidal rotation. Furthermore, we note that the plasma edge of tokamaks and linear devices has been shown to generate plasma density "blobs" and "holes" [26, 27]; the blobs propagate outwards while the holes propagate inwards and have vorticity associated with them [27, 28]; this region of toroidally confined plasmas has long been known to have a shear layer present due to equilibrium effects at the last closed flux surface. Thus a radial vorticity flux and associated wave stresses must exist at the boundary of the tokamak plasmas and may contribute to shear flow amplification and intrinsic rotation in these devices. Similar experiments should be repeated on large tokamaks to confirm the above physical picture, particularly there will be a clearer scale separation between turbulent correlation lengths and the scale length from generation to damping locations. These results also show that particle flux and vorticity flux are closely related and suggest that potential vorticity conservation plays an important role in momentum transport in confined plasmas, much like in planetary and stellar atmospheres [29]. These issues are now under investigation and will be discussed in future publications [30].

References:

[1] P.H. Diamond, C.J. McDevitt, Ö.D. Gürcan, T.S. Hahm, W. X. Wang, E.S. Yoon, I. Holod, Z. Lin, V. Naulin and R. Singh, Nucl. Fusion **49,** 045002 (2009)

[2] J.E. Rice , W.D. Lee, E.S. Marmar, P.T. Bonoli, R.S. Granetz, M.J. Greenwald, A.E. Hubbard, I.H. Hutchinson, J.H. Irby, Y. Lin , D. Mossessian, J.A. Snipes, S.M. Wolfe and S.J. Wukitch, Nucl. Fusion 44, 379 (2004)

[3] W M Solomon, K H Burrell, J S deGrassie, R Budny, R J Groebner, J E Kinsey, G J Kramer, T C Luce, M A Makowski, D Mikkelsen, R Nazikian, C C Petty, P A Politzer, S D Scott, M A Van Zeeland and M C Zarnstorff, Plasma Phys. Control. Fusion, 49, B313 (2007)

[4] Z. Yan, M. Xu, P. H. Diamond, C. Holland, S. H. Muller, G. R. Tynan, J. H. Yu, Phys. Rev. Lett. **104**, 065002 (2010)

[5] Howard, L. N. and R. Krishnamurti, J. Fluid Mech., **170**, 385 (1986)

[6] G. R. Tynan, A. D. Bailey III, G. A. Campbell, R. Charaton, A. de Chambrier, G. Gibson, D. J. Hemker, K. Jones, A. Kuthi, C. Lee, T. Shoji, and M. Wilcoxson, J. Vac. Sci. Technol A **15**, 2885 (1997)

[7] M. J. Burin, G. R. Tynan, G. Y. Antar, N. A. Crocker, and C. Holland, Phys. Plasmas **12**, 052320 (2005)

[8] C. Holland, J. H. Yu, A. James, D. Nishijima, M. Shimada, N. Taheri and G. R. Tynan, Phys. Rev. Lett. **96** 195002 (2006)

[9] G. R. Tynan, C. Holland, J. H. Yu, A. James, D. Nishijima, M. Shimada, and N. Taheri , Plasma Phys. Control. Fusion **48** S51 (2006)

[10] Z. Yan, J. H. Yu, C. Holland, M. Xu, S. H. Muller, and G. R. Tynan, Phys. Plasmas **15** 092309 (2008)

[11] Z. Yan, G. R. Tynan, C. Holland, M. Xu, S. H. Muller, and J. H. Yu, Phys. Plasmas **17** 012302 (2010)

[12] Z. Yan, G. R. Tynan, C. Holland, M. Xu, S. H. Muller, J. H. Yu, Phys. Plasmas **17** 032302 (2010)

[13] M. Xu, G. R. Tynan, C. Holland, Z. Yan, S. H. Muller, J. H. Yu, Phys. Plasmas **16** 042312

(2009)

[14] M. Xu, G. R. Tynan, C. Holland, Z. Yan, S. H. Mueller, J. H. Yu, Phys. Plasmas **17,** 032311 (2010)

[15] J. H. Yu, C. Holland, G. R. Tynan, G. Antar, and Z. Yan, J. Nucl. Mat, **363-365** 728-732 (2007)

[16] K. H. Burrell, Phys. Plasmas **4**, 1499 (1997)

[17] S H Müller, C Theiler, A Fasoli, I Furno, B Labit, G R Tynan, M Xu, Z Yan, and J H Yu, Plasma Phys. Control. Fusion **51**, 055020 (2009)

[18] Walraven, R., Proc. Digital Equipment User's Society, Davis, CA, Department of Applied Science, University of California, 23–30

[19] G. Y. Antar, J. H. Yu, and G. Tynan, Phys. Plasmas 14, 022301 (2007)

[20] J.C. McWilliams J. Fluid Mech. 146, 21 (1984)

[21] R. R. Trieling, O. U. Velasco Fuentes, and G. J. F. van Heijst, Phys. Fluids **17**, 087103 (2005)

[22] P. Manz, M. Ramisch, and U. Stroth, Phys. Rev. Lett. **103**, 165004 (2009)

[23] G. I. Taylor, Phil. Trans. Roy. Soc., London A215, 1–26, 1915

[24] P H Diamond, O D Gurcan, T S Hahm, K Miki, Y Kosuga and X Garbet, Plasma Phys. Control. Fusion **50** 124018 (2008)

[25] P. H. Diamond, S. I. Itoh, K. Itoh, and T. S. Hahm, Plasma Phys. Control. Fusion **47** R35-R161 (2005)

[26] S. I. Krasheninnikov, Phys. Lett. A **283**, 368 (2001)

[27] J. A. Boedo, D. L. Rudakov, R. A. Moyer et al., Phys. Plasmas **10**, 1670 (2003)

[28] O. Grulke, J. L. Terry, B. LaBombard, and S. J. Zweben, Phys. Plasmas **13**, 012306 (2006)

[29] D.G. Dritschel, M.E. McIntyre, J. Atm. Sciences 65, 855 (2008)

[30] C. McDevitt, P.H. Diamond, O.D. Gurcan, T.S. Hahm, submitted to Phys. Plasmas (2010)

Chapter 7

Summary, discussions and future plans

In this chapter, we first summarize the key objectives and conclusions of this work, then discuss the implications of the work and make suggestions for the future work.

7.1 Summary and conclusions

This dissertation work was oriented to answer two inherently related questions:

(1) How is the turbulent energy redistributed over different turbulent frequencies or scales and in particular what turbulent spatiotemporal scales are involved in sustaining the large scale sheared zonal flow?

(2) What is the microscopic physics mechanism that leads to this nonlinear turbulence drive?

To answer the first question, we developed an experimental technique to directly measure the energy exchange rates among different frequencies, especially between turbulence and shear flows which allows us to determine the energy transfer from turbulence to shear flows through nonlinear processes. This measurement was made possible by experimentally determining the appropriate cross-bispectrum that arises from the convective derivative term in either momentum or continuity equation. When the momentum equation is used to write a kinetic energy conservation equation, and this result was then transformed into frequency domain, the convective nonlinear term gave the nonlinear kinetic energy transfer term $-\mathrm{Re}\left\langle \vec{u}_{\perp f}^{*}\cdot\left(\vec{u}_{\perp f_2}\cdot\nabla_{\perp}\vec{u}_{\perp f_1}\right)\right\rangle$ which we denoted as $T_u(f, f_1)$. The kinetic energy transfer term is basically a cross-bispectrum involving different frequencies, of which the value depends on the coherence among these three different frequencies, i.e., the only process that gives a nonzero $T_u(f, f_1)$ is that two waves with coherent phases beat together to produce the third. By approximating the turbulent velocity by $\vec{E}\times\vec{B}$ velocity $\vec{u}_{\perp} = \hat{z}\times\nabla_{\perp}\phi / B$, all the quantities needed for computing the nonlinear energy transfer term can be measured by a specially designed dual 3x3 Langmiur probe array. Measuring the internal energy transfer was very similar to measuring the kinetic energy transfer. Since this method was directly based on the momentum and continuity equations and no special assumptions were needed, it reveals the first principle physics of the nonlinear energy transfer.

Experiments with this technique showed that both kinetic and internal energy were nonlinearly transferred from turbulences with intermediate frequencies (5-12 kHz) into shear flows with low frequencies (<1 kHz) at the velocity shear region, which is exactly what should be expected for a turbulence-driven shear flow. An examination of the experimentally measured dispersion relation showed that these intermediate frequencies corresponded to fluctuations with an average azimuthal mode number m~3; the fluctuations had a broad spectrum and thus cannot be thought of as coherent waves, but rather would correspond to spatially localized structures. It was also found through experiments that the radial flux of vorticity is dominantly responsible for the kinetic energy transfer to shear flows, which suggested that the vorticity flux mediates the transfer of kinetic energy.

Based on these findings, we then carried out a subsequent study using the dual 3x3 probe array and a fast framing camera coupled to a telescope which provided a physical picture of the underlying microphysics that leads to the observed nonlinear energy transfer. The probe array measurements showed that the intermediate frequency (~ 10 kHz) fluctuations were nonlinearly generated in the inner plasma region r=2-3 cm by extracting energy out of a wide range of drift wave frequencies. Fast imaging also showed very clearly that m~3 coherent turbulent structures are generated at r~2cm. A cross-correlation analysis of these structures using the 3x3 array showed that the structures have a finite vorticity that is in phase with the density fluctuations, indicating that they are in fact drift vortices formed by the nonlinear interaction of multiple drift waves. These structures were then observed to spiral out toward the edge at r=3.5-4 cm, and undergo a tilting, stretching and absorption process at the shear layer located at the plasma boundary. This results in an increase in the turbulent shear stress at the boundary, which gives rise to an amplification of the large scale shear flow. The associated vorticity flux is directly related to and consistent with the turbulent Reynolds stress, which has been previously shown to be consistent with the observed sheared flow. Furthermore, the probe measurements also demonstrated that an increase of vorticity flux in the central plasma region *precedes* the increase of Reynolds stress at the boundary, confirming the causality of the observations.

These observations have significant implications for shear flow formation in toroidal confinement devices. For example, there are many published papers (see e.g. [1, 2] for representative work) showing the propagation of coherent density fluctuations (also known as “blobs”, “avaloids” and/or “intermittent plasma objects”) at the edge of tokamak devices. These earlier works have implied that these discrete structures have a finite vorticity associated with them. Since these structures move radially, it is a straightforward inference to then conclude that a vorticity flux exists at the boundary of these devices as well. This flux is associated with the turbulent Reynolds stress which has been associated with the generation of large scale sheared flows. Furthermore, this same region of the plasma is known to be universally characterized by a pre-existing sheared flow. Thus the conditions that lead to the turbulent amplification of sheared flows at the boundary of these devices exist; the transition from a state of low confinement (L-mode) to high confinement (H-mode) which occurs at the boundary of the plasma might then be associated with a transport of momentum and kinetic energy mediated by these edge plasma blobs.

There are limitations for the experiments on CSDX. First of all, in CSDX the density gradient scale length is about 2 cm while the turbulent correlation length is about 1 cm. Furthermore, the spatial separation between the structure birth location and the absorption location is only about 1.5-2cm. Therefore the spatial scale separation, which is often assumed in theoretical models, is marginal at best and a clearer scale separation, especially if we want to generalize the results measured on a linear device to tokamaks, or to compare with theoretical and computational models is needed. Second, when using the electric field calculated from floating potential instead of plasma space potential to estimate $\vec{E} \times \vec{B}$ velocity, we neglected the temperature fluctuation and assumed it to be small. Although this seems to be reasonable according to published papers [3], we may need to investigate it on CSDX since drift wave turbulence is driven by pressure gradient, and temperature could play a role in the generation of shear flows. Third, all the analyses were done on just one condition (fixed pressure, and RF power), it would be interesting to do a parametric scan to see if at other conditions the physical picture still hold, or some new physics will come out.

7.2 Discussions and future plans

These results suggest several future experiments that would test the key conclusions of this work, and which would provide additional insight into the physics of turbulence-shear flow interactions.

7.2.1 Perturbative and bias experiments on CSDX

So far all the experiments on CSDX, such as the momentum conservation analysis, residual stress measurement, and the nonlinear energy transfer rate estimation, are measurements for the self-organized response of plasmas. If fluctuations can drive shear flow, then externally introduced fluctuations may also drive shear flow. By externally exciting fluctuations in the plasma we can study the shear flow response to externally introduced fluctuations. It is expected that when excited fluctuations are strong, shear flow should be strong; when excited fluctuations are weak, then shear flow should be weak. If this conjecture is confirmed in CSDX, it could be tested on tokamak devices, where it could offer a potential method to control shear flow intensity at the edge of tokamaks and thus offer a way to get a better confined plasma, or at least a way to trig H-mode transition. If externally excited fluctuations do not reinforce shear flow it would be useful to understand why . Another elegant experiment would be using externally applied bias voltage to change the plasma space potential, therefore to introduce a perturbed radial electric field and associated azimuthal ExB drift in the plasma. In particular, it would be interesting to try and cancel out the intrinsic rotation inside CSDX plasma, which is another way to prove the existence of self-generated momentum. Once the sheared flow is cancelled we can do a systematic study of plasma, such as measuring the nonlinear energy transfer rates, particle flux and corresponding phase relations, then compare the results against the case when there is an intrinsic rotation. Finally, the external bias could then be rapidly removed, and the resulting spin-up of the plasma from turbulent momentum transport could be studied.

7.2.2 A systematic study of the transition to turbulent stage

Earlier work in CSDX has shown that the transition from coherent drift wave oscillations to a state of weak drift turbulence can be controlled by increasing the magnetic field from low values (~400 G in Argon) to higher values exceeding ~700 G in Argon. During such a transition, one would then measure all relevant quantities such as density and potential rms fluctuation intensity, particle flux, Reynolds stress, nonlinear energy transfer rate and fast imaging of 2D dynamics, etc. during the gradual transition. The results should then provide a deeper understanding of the role that plasma turbulence plays in the development of sheared zonal flows.

7.2.3 Analysis of nonlinear energy transfer using conditional average

Typically very long time series are needed to get converged bispectra. For the nonlinear energy transfer measurement on CSDX, ~ 10 second of data were divided into more than 1000 independent windows to do the ensemble averages. Thus it is not possible to study the dynamics of energy transfer using this approach. Earlier work in CSDX has demonstrated that the shear flow slowly grows and decays. Since the CSDX plasma is highly stable, by using conditional average technique we could study the evolution of energy transfer over time. The growth and collapse phases of shear flows can be separated this way, and the nonlinear energy transfer rates of both phases can be obtained and compared against each other.

7.2.4 Increasing the separation of spatial scales

As discussed above, one of the weaknesses of the current CSDX experiments is a poor separation of spatial scales. If the device could be upgraded to operate at higher magnetic fields, operate with lighter ions (e.g. neon, helium or even hydrogen) and/or operate with a larger sized plasma source, is likely that a wider range of sizes of drift vortices could be observed, and a larger separation between the vortex birth region and the shear layer could be produced. If this distance was large enough, it might be possible to try and observe the formation of multiple zonal flow shear layers and thus confirm theoretical predictions of an equivalent to the Rhines scale that has been observed in geophysical systems.

7.2.5 A testing of ideas from linear machines on tokamak plasmas

In principle, similar measurements of the energy transfer rates, the Reynolds stress and background poloidal and toroidal flow velocities could be performed in tokamak devices. This would be a direct test to see whether the vortex-driven physics picture at CSDX plasma edge is operative in hot toroidal plasmas. This would require the design of an appropriately arranged array of probes which could then be inserted into the edge region of such a plasma. Of course, the parallel heat flux in such a device is much higher, and care would have to be taken that the probe array does not overheat and/or cause unacceptable disturbances to the tokamak plasma discharge.

It is likely that multiple discharges would have to be carried out in order to obtain adequately long datasets for the required ensemble averaging. In addition, fast imaging of the tilting, stretching and absorption of turbulent structures using fast imaging diagnostics in tokamak plasmas, and associated such observations with the evolution of sheared flows in these devices would also provide useful tests of the observations presented in this work.

References:

[1] J. A. Boedo, D. L. Rudakov, R. A. Moyer, G. R. McKee, R. J. Colchin, M. J. Schaffer, P. G. Stangeby, W. P. West, S. L. Allen, T. E. Evans, R. J. Fonck, E. M. Hollmann, S. Krasheninnikov, A. W. Leonard, W. Nevins, M. A. Mahdavi, G. D. Porter, G. R. Tynan, D. G. Whyte, and X. Xu, Phys. Plasmas **10**, 1670 (2003)

[2] O. Grulke, J. L. Terry, B. LaBombard, and S. J. Zweben, Phys. Plasmas **13**, 012306 (2006)

[3] N. Mahdizadeh, F. Greiner, M. Ramisch, U. Stroth, W. Guttenfelder, C. Lechte and K. Rahbarnia, Plasma Phys Contr F **47** (4), 569-579 (2005).